


Università di Brescia

DIPARTIMENTO DI INGEGNERIA MECCANICA E INDUSTRIALE

DOTTORATO DI RICERCA IN TRANSIZIONE ENERGETICA E SISTEMI PRODUTTIVI SOSTENIBILI

CICLO XXXVIII

SETTORE SCIENTIFICO DISCIPLINARE: CHEM-06/A

# Hybrid computational methods for environment and health: applications in catalysis, sensing and advanced diagnostics

PhD Candidate

Michele Speziani

Supervisor

Prof. Ivano Alessandri (Università di Brescia)

Prof. Michele Ceotto (Università degli Studi di Milano)

# 1. Index

**1. Index ..... 3**

**2. Abstract ..... 4**

**3. Introduction ..... 9**

**4. Overview on the computational methods ..... 21**

**5. Carbon dioxide adsorption on titanium dioxide ..... 29**

5.a Convergence tests and the importance of supercell dimensions ..... 29

5.b Surface energy of anatase facets and guidelines for its calculation ..... 48

5.c Adsorption geometries of $CO_2$ on (001) anatase ..... 58

5.d Computational and experimental characterization of adsorbates ..... 67

5.e Simulations of single-site catalysts: examples with calcium and magnesium ..... 83

**6. Other projects ..... 98**

6.a The reaction of refrigerant gases investigated via DFT and vibrational spectroscopy .... 98

6.b DFT study on the interaction between histamine and polydopamine ..... 111

6.c Estimation of the deacetylation grade of chitosan via FTIR spectroscopy ..... 121

6.d Baseline correction algorithm of Raman spectra: analysis of the Schulze algorithm .... 135

**7. Notes on the synthesis procedures and characterization of titanium dioxide .150**

**8. Conclusions and future perspectives .....160**

# 2. Abstract

## (EN)

The project detailed within this thesis aims to unite two fields often perceived as vastly distant: chemistry and computer science. Although the origins of these and other disciplines followed highly specific historical needs, over time we have witnessed a partial overlap among many seemingly unrelated areas. As proof of this, one can look at the 2024 Nobel Prizes in Chemistry and Physics, both of which recognized projects where computer science played a fundamental role. The ability to predict the behaviour of a real-world system using dedicated software drives innovation in research, enabling the construction of much more robust hypotheses that are likely to be verified through subsequent experimentation. This significantly reduces the time required for experimental investigations, as the major effort is often shifted to computational studies rather than the practical experiments. To be clear, the necessity of the latter remains indispensable, since a core requirement of the scientific method is the need to verify the validity of any theory.

Given the general terms through which computer science serves as a valuable support to chemistry, this thesis intends to address highly topical case studies, which are, in some instances, remarkably different from one another. The predominant effort has been dedicated to the study of titanium dioxide ($TiO_2$, titania), a widely known material with extensive applications across many sectors. Examples of these are found in many industrial processes that exploit its brilliant white colour, the cosmetic and pharmaceutical fields, where its role as a stabilizer and solar filter is widely appreciated, and, despite some controversy, the food industry. A wide range of chemical applications is present, due to the photocatalytic properties of this material which allow the development of next-generation catalysts. Inevitably, the focus of this thesis will be concentrated on this latter category of applications. Significant interest has emerged regarding the possibility of exploiting the photocatalysis enabled by this material as a co-catalyst in applications aiming to convert carbon dioxide into energy vectors.

This project represents a fundamental theme in the energy transition, as it simultaneously reduces the atmospheric presence of one of the most harmful pollutants and aims to obtain energy-carrying molecules. The use of these compounds, much like the use of biofuels, would enable a carbon cycle independent of fossil sources, with a net-zero overall emission balance. However, this is hindered by the properties of $CO_2$ itself, which is a particularly stable molecule that is very difficult to decompose

and convert into other products. The deployment of appropriate photocatalysts would allow these energy barriers to be overcome and promote the conversion of the molecule.

To achieve this, however, the catalyst must be selective, targeting selectively certain molecules, and at the same time avoiding electron-hole recombination. This phenomenon is enabled only when the target molecule, $CO_2$ in the case study under analysis, is adsorbed onto the catalyst surface. To this end, the comprehensive study of the geometries and principles governing $CO_2$ adsorption on titania represents the cornerstone of this section of the thesis. For this purpose, Density Functional Theory (DFT) served as a fundamental tool in predicting the interaction between molecules and surfaces. Inevitably, it was also necessary to identify the methods to validate the computational results once the simulations were completed. Among the available characterization techniques, vibrational spectroscopy certainly represented a key element, as the vibrational frequencies of adsorbed species are readily obtainable through DFT.

The simulations confirmed that the reactivity of a material, and consequently its ability to favour specific types of adsorptions, depends on the exposed crystal facet. Therefore, the synthesis and characterization of titanium dioxide samples with preferentially exposed crystal facets were of particular interest. As side results, direct correlations were observed between computational parameters and simulation outcomes, leading to the identification of convenient working frameworks to achieve robust simulations.

The techniques investigated in depth within the presented case study subsequently proved fundamental in parallel projects as well, which were also characterized by a strong connection to the energy transition and pollutants and allergens monitoring. It is worth mentioning the study of products obtained following the reaction between refrigerant gases, where DFT allowed for the determination of which configurations were the most stable, and vibrational spectroscopy enabled the validation of the simulation results. Similarly, it was possible to demonstrate the interaction between histamine and polydopamine, which allows Raman resonators coated with the polymer to detect the molecule at low concentrations.

Purely spectroscopic investigations concerned the study of FTIR and Raman spectra of polymers (chitosan, plastics) where, for various reasons, a fundamental step of the analysis was characterized by the issue of spectral baseline removal. It was therefore possible to identify suitable methods tailored specifically to the case study in question. In the case of chitosan, a rapid method based on infrared spectroscopy was identified for estimating the degree of deacetylation.

The first part of this thesis will focus on the issue of titania and its role as a carbon dioxide adsorbent; the second section, instead, will feature stand-alone chapters that specifically describe the other studies conducted.

# (IT)

Il progetto dettagliato all'interno di questa tesi mira a unire due campi spesso percepiti come ampiamente distanti: la chimica e l'informatica. Sebbene le origini di queste e di altre discipline abbiano risposto a esigenze storiche estremamente specifiche, nel tempo si è assistito a una parziale sovrapposizione tra molte aree apparentemente non correlate. A riprova di ciò, si può guardare ai Premi Nobel per la Chimica e per la Fisica del 2024, i quali hanno entrambi riconosciuto progetti in cui l'informatica ha svolto un ruolo fondamentale. La capacità di prevedere il comportamento di un sistema reale utilizzando software dedicati guida l'innovazione nella ricerca, consentendo la costruzione di ipotesi molto più robuste che hanno maggiori probabilità di essere verificate attraverso la successiva sperimentazione. Questo riduce significativamente il tempo richiesto per le indagini sperimentali, poiché lo sforzo maggiore viene spesso spostato sugli studi computazionali piuttosto che sugli esperimenti pratici. Per completezza, la necessità di questi ultimi rimane indispensabile, poiché un requisito fondamentale del metodo scientifico è l'esigenza di verificare la validità di qualsiasi teoria.

Date le modalità generali attraverso cui l'informatica funge da prezioso supporto alla chimica, questa tesi intende affrontare casi di studio di grande attualità, che sono, in alcuni casi, notevolmente diversi tra loro. Lo sforzo predominante è stato dedicato allo studio del biossido di titanio ($TiO_2$, titania), un materiale ampiamente noto con vaste applicazioni in molti settori. Esempi di queste si trovano in molti processi industriali che sfruttano il suo colore bianco brillante, nei campi cosmetico e farmaceutico, dove il suo ruolo come stabilizzatore e filtro solare è ampiamente apprezzato, e, nonostante alcune controversie, nell'industria alimentare. È presente un'ampia gamma di applicazioni chimiche, dovuta alle proprietà fotocatalitiche di questo materiale che consentono lo sviluppo di catalizzatori di prossima generazione. Inevitabilmente, il focus di questa tesi si concentrerà su quest'ultima categoria di applicazioni. Un notevole interesse è emerso riguardo alla possibilità di sfruttare la fotocatalisi attivata da questo materiale come co-catalizzatore in applicazioni volte a convertire l'anidride carbonica in vettori energetici.

Questo progetto rappresenta un tema fondamentale nella transizione energetica, in quanto riduce simultaneamente la presenza atmosferica di uno degli inquinanti più nocivi e mira a ottenere molecole ad alto contenuto energetico. L'uso di questi composti, proprio come l'uso dei biocarburanti, consentirebbe un ciclo del carbonio indipendente dalle fonti fossili, con un bilancio complessivo delle emissioni prossimo allo zero. Tuttavia, ciò è ostacolato dalle proprietà della stessa $CO_2$, che è una molecola particolarmente stabile, molto difficile da decomporre e convertire in altri prodotti. L'impiego di adeguati fotocatalizzatori consentirebbe di superare queste barriere energetiche, le quali ostacolano la conversione della molecola.

Per ottenere questo, il catalizzatore deve essere selettivo, bersagliando specificatamente alcune molecole, e allo stesso tempo evitando la ricombinazione delle coppie elettrone-lacuna. Questo fenomeno si attiva solo quando la molecola target, la $CO_2$ nel caso di studio in esame, viene adsorbita sulla superficie del catalizzatore. A tal fine, lo studio approfondito delle geometrie e dei principi che regolano l'adsorbimento della $CO_2$ sulla titania rappresenta il cuore di questa sezione della tesi. Per questo scopo, la Density Functional Theory (DFT) è risultato uno strumento fondamentale nel prevedere l'interazione tra molecole e superfici. Inevitabilmente, è stato anche necessario identificare i metodi per convalidare i risultati computazionali una volta completate le simulazioni. Tra le tecniche di caratterizzazione disponibili, la spettroscopia vibrazionale ha certamente rappresentato un elemento chiave, poiché le frequenze vibrazionali delle specie adsorbite sono facilmente ottenibili tramite DFT.

Le simulazioni hanno confermato che la reattività di un materiale, e di conseguenza la sua capacità di favorire specifici tipi di adsorbimento, dipende dal piano cristallino esposto. Pertanto, la sintesi e la caratterizzazione di campioni di biossido di titanio con piani di taglio preferenzialmente esposti sono stati di particolare interesse. Come risultati secondari, sono state osservate correlazioni dirette tra i parametri computazionali e i risultati delle simulazioni, portando all'identificazione di convenienti protocolli di lavoro per ottenere simulazioni robuste.

Le tecniche approfondite all'interno del caso di studio presentato si sono successivamente rivelate fondamentali anche in progetti paralleli, anch'essi caratterizzati da un forte legame con la transizione energetica e con il monitoraggio di inquinanti e allergeni. Vale la pena menzionare lo studio dei prodotti ottenuti a seguito della reazione tra gas refrigeranti, dove la DFT ha permesso di determinare quali configurazioni fossero le più stabili e la spettroscopia vibrazionale ha consentito la validazione dei risultati delle simulazioni. Allo stesso modo, è stato possibile dimostrare l'interazione tra istamina

e polidopamina, che consente ai risonatori Raman rivestiti con il polimero di rilevare la molecola a basse concentrazioni.

Altri progetti paralleli hanno previsto un approccio combinato computazionale e sperimentale per analizzare le interazioni tra diverse specie chimiche. Si deve menzionare lo studio dei prodotti ottenuti a seguito della reazione tra gas refrigeranti, dove la DFT ha permesso di determinare quali configurazioni fossero le più stabili e la spettroscopia vibrazionale ha consentito la validazione dei risultati delle simulazioni. Allo stesso modo, è stato possibile dimostrare l'interazione tra istamina e polidopamina, che consente ai risonatori Raman rivestiti con il polimero di permettere la rilevazione della molecola a basse concentrazioni.

Indagini puramente spettroscopiche hanno riguardato lo studio di spettri FTIR e Raman di polimeri (chitosano, plastiche) dove, per varie ragioni, una fase fondamentale dell'analisi è stata caratterizzata dal problema della rimozione della linea di base spettrale. È stato quindi possibile identificare metodi idonei e studiati appositamente per i casi studio in questione. Per quanto riguarda il chitosano, è stato individuato un metodo rapido basato sulla spettroscopia infrarossa per stimare il grado di deacetilazione.

La prima parte di questa tesi si concentrerà sulla questione della titania e del suo ruolo come adsorbente dell'anidride carbonica; la seconda sezione, invece, presenterà capitoli indipendenti che descrivono specificamente gli altri studi condotti.

# 3. Introduction

*This thesis is subdivided in two macro sections: the first one which focuses on titanium dioxide and its role as a photocatalyst driven by DFT simulations, and the second one which describes other projects related to chemical characterization with a strong computer science component. Each work in the latter section will be presented in a paper-like format; thus, each one will be briefly introduced in the corresponding section. Given the relevance that Density Functional Theory (DFT) acquired to a proper estimation of $TiO_2$ behaviour, an outline of this method will be exposed, with the scope of a better comprehension of the following considerations. This chapter aims to present the state of the art about titanium dioxide, possible techniques for its characterization and its role as catalyst.*

## $TiO_2$ overcomes noble metals: brief discussion over costs and safety

Titanium dioxide ($TiO_2$) is a non-toxic and low-cost material which nowadays finds many industrial applications. Its photocatalytic activity has been demonstrated in many industrial applications for air and water remediation. It represents a novel perspective compared to common catalysts, which include noble metals without an adequate grade of control over the reactions promoted, and, at the same time, which often present prohibitive costs. The utilization of $TiO_2$ as a co-catalyst supported by noble metals remains a possibility, taking advantage of the beneficial properties of both.

A quickly understandable example of this is given by the catalytic converter of vehicles, whose role is necessary to limit air pollution but with costs that are surprisingly high. A catalytic converter is commonly an alloy of platinum (60 €/g), palladium (45 €/g) and rhodium (300 €/g) (source: https://it.tradingeconomics.com/)[1]. The price for a catalytic converter of a small car can easily reach hundreds of euros, considering its composition of a few grams of noble metal[2]. The geographic distribution of deposit of metals must be as well considered, as political tensions may limit their actual availability[3]. Because of this, the price of the metal can undergo strong fluctuations depending on not-controllable factors. Given these factors, novel catalysts should consider the actual availability of a material, as it represents a necessary condition for its industrial applications. From the economic side, titanium dioxide belongs to completely different price ranges, hardly exceeding 1€/g even for high purity samples with desired features.

Another factor which should be considered is the possible toxicity of a material. Many noble metals are not considered to pose health risks to the general population[4]. Possible formation of toxic compound, such as some Pt salts, was not judged as critical because of the low concentration[4].

However, it was reported that because of the extraction processes, ground-up noble metals may be dangerous due to possible impurities, represented by lead or residues of exhausted batteries[5]. Moreover, nanoparticles produced by catalyst wear can damage cells, since their microscopic size allows them to penetrate cellular membranes, and the continuous exposure has been widely explicitly stated[6]. Thus, if on one side the combination of a low quantity of material and its limited exposition makes the harmfulness a theoretical issue, on the other hand the continuous request for catalysts connected to the industrial scale up makes the catalyst subject to this criticism, due to the overall total quantity and the variety of usage.

In this regard, titanium dioxide is not considered harmful to the environment and health, although it is not completely immune to criticism. Some research investigates possible damage which $TiO_2$ might cause to human health, which drove the decision of the International Agency for Research on Cancer (IARC) in 2006 to declare it as a Group 2B carcinogen (i.e. possibly carcinogenic to humans) when inhaled[7]. This characteristic tends to describe many nanoscopic powders, as mentioned about Pt nanoparticles, because they potentially interact with biological organisms in hardly predictable ways. Notably, a recent study demonstrated biological alteration in workers exposed to pigment grade $TiO_2$, substantially denying previous research which stated the opposite[8], [9].

Because of media pressure about potential adverse effects caused by $TiO_2$, in the last few years different authorities explicitly declared their opinions about its use as a food additive. After a consideration promoted by the European Union about its unsafety, the UK and Canada contested the opinion and criticized the quality of the data the EU based its decision on[10], [11], [12]. In any case, $TiO_2$ is still used for different applications, such as pigments, excipients and sun creams.

A general consideration which appears from promoters of $TiO_2$ applications is that the advantages drastically outweigh the drawbacks. Moreover, the EU decision is based on the impossibility to define safe levels of intake in food. Lastly, the Safety Data Sheet of a general nanostructured $TiO_2$ does not signal any harmful point, except in some cases remarking its potential carcinogenicity if inhaled and general possible discomfort when in contact with mucous membranes as a generic foreign substance. To the best of our knowledge, just a few suppliers of $TiO_2$ include the hazard statement: H351 – Suspected of causing cancer (inhalation) and the corresponding danger pictogram.

Following these considerations, titanium dioxide cannot be defined as an intrinsically dangerous compound, as the potential harmfulness derives from its shape and specifically following inhalation. Thus, to reduce the overall risk, general protection devices are recommended to work with $TiO_2$, even

more so when considering dry powder. In other contexts, such as real-case scenarios where powder is incorporated into macroscopic scaffolds for catalysis purposes, titanium dioxide can be considered completely safe. Obviously, accidental detachment of the powder from the scaffold should be avoided, but primarily because it would cause loss of catalyst more than because of safety issues. It must be also considered that often pure $TiO_2$ is not directly used, as doped versions could present improved performance. Thus, the actual harmfulness of $TiO_2$-based materials mostly depends on dopants and other chemicals that constitute the catalyst and evidently must be considered as well.

## Different forms of stoichiometric titanium dioxide

As repeatedly remarked in the previous section, $TiO_2$ is commonly available as a white powder, although different forms may be obtained via specific synthesis techniques. This paragraph requires an introduction on the crystalline structure of titanium dioxide, as it may present many different polymorphs[13]. Just three of them, anatase, rutile and brookite, plus the amorphous one, are naturally occurring and at the same time have significant industrial relevance because of their relative stability[14]. The most studied of them are anatase and rutile, as they exhibit the highest photocatalytic activity under solar radiation; the third one is brookite and its higher bandgap combined with the difficulties in its production make it the least studied naturally occurring $TiO_2$ polymorph. Since $TiO_2$ is commonly used in photocatalytic applications, a parameter which must be highlighted is the bandgap, which is typically around 3.20 eV for anatase, 3.03 for rutile and 3.24 eV for brookite[14]. Therefore, to promote the excitation of electrons in stoichiometric titania, a radiation with wavelength in the UV region is required. This effectively limits the efficiency of photocatalysis induced by solar light, whose UV component does not exceed the 4%. Doped or defective titania may present a lower bandgap, usually assuming a darker or even black colour, but a complete in-depth analysis is out of the scope of this thesis, which strictly analyzes the behaviour of stoichiometric $TiO_2$[15].

Commercial $TiO_2$ powder is not usually monocrystalline, but this factor depends on the objective the sample was designed for. For example, for $TiO_2$-based pigments, the refractive index and colour are fundamental for aesthetic and technical purposes, such as achieving the desired opacity. A patent filed by Ishihara et al, which contains a method for producing $TiO_2$ pigment, reports an almost 100% composition of anatase, while that of Bender et al indicates that rutile is preferrable[16], [17]. They

state two different goals: the first one aims to enhance the “bluish color tone and physical characteristics such as low hardness” while the second focuses on the “high greying stability” caused by the highest refractive index ($n_{anatase}$=2.7, $n_{rutile}$=2.8)[18].

X-Ray Diffraction (XRD) obviously represents the gold standard to achieve phase recognition, although phase recognition can also be successfully performed via Raman spectroscopy, as the three polymorphs of interest present significantly different spectra[19], [20]. Relative composition in terms of phases may not be easily available with Raman spectroscopy due to sample inhomogeneities, while thanks to a higher penetration depth XRD is less sensitive to internal variabilities. When the concentration of a phase is comparatively very low with respect to others, its specific features may be covered.

Recently, Raman spectroscopy in combination with Machine Learning has demonstrated to be an interesting tool for the quantification of anatase and rutile in binary mixtures[21]. In the work sponsored by the Italian Institute for Metrological Research, different participants equipped with different Raman spectrometers analysed binary mixtures anatase/rutile obtaining quantification errors lower than 3%. Three mixtures consisting of 5%, 45%, and 80% anatase were considered in the test, thus the calculated models adapt to a broad range of conditions. This approach suggests that specific pretrained models are required to perform phase quantification.

## Overview on some commercial samples

Following in the thesis, commercial $TiO_2$ will be used as references. Two samples were primarily considered: Degussa P25 (Evonik) and Hombikat UV100. The main difference between them is that Degussa P25 shows an anatase content over 70%, with a consistent grade of inhomogeneity in phase composition, while UV100 consists of pure anatase[22], [23]. It was reported that Hombikat has a larger surface area compared to P25, consequence of the reduced size of its crystals[24]. Both can be considered TiO2 nanoparticles, with average diameter of around 20 and 8 nm for crystals in P25 and Hombikat respectively. Notably, different size estimation performed on different samples confirmed inhomogeneity of P25[24], [25]. Because of the limited size of these particles, the considerations about safety of their use are relevant, thus all the precautions to avoid inhalation should be applied.

Early research was sceptical about heterojunction-promoted charge transfer in Degussa P25[26]. Nevertheless, recent studies demonstrate enhanced photocatalytic efficiency in these multi-phase nanoparticles[27], [28], [29], [30].

## Application of $TiO_2$ for $CO_2$ conversion

Carbon dioxide is one of the most critical pollutants driving global climate change. Its role as a greenhouse gas is well-established, and its continuous accumulation led to devastating impacts on the environment, economy, and society. While a detailed discussion of its origins and emission mitigation strategies is highly relevant, it remains outside the scope of this thesis. At the same time, another critical challenge of the current energy transition is the urgent need for alternative energy vectors to bypass dependency on fossil fuels.

These dual challenges inspire the concept of utilizing $CO_2$ as a primary resource to produce energy vectors. However, this process is highly complex due to the thermodynamic stability of the carbon dioxide molecule; predicting and achieving the cleavage of an oxygen atom requires highly efficient, specialized catalysts.

Once carbon monoxide is obtained, it can serve as a building block for synthesizing new molecules acting as energy vectors, potentially replacing fossil fuels in current applications. A pathway which includes production of CO as starting point is not necessarily the exclusive or preferred route, as alternative direct-conversion strategies may be also evaluated.

To address these challenges, the primary objective of this thesis is a combined computational and experimental study of $TiO_2$ surfaces capable of adsorbing $CO_2$. It is remarkable that the $TiO_2$ is not intended as a novel material capable of storing $CO_2$, but a photocatalytic surface helpful to drive its chemical conversion. Conversion process remained out of the scope of this thesis work, but it represents a direct perspective of what has been hereby demonstrated.

## Overview of the work

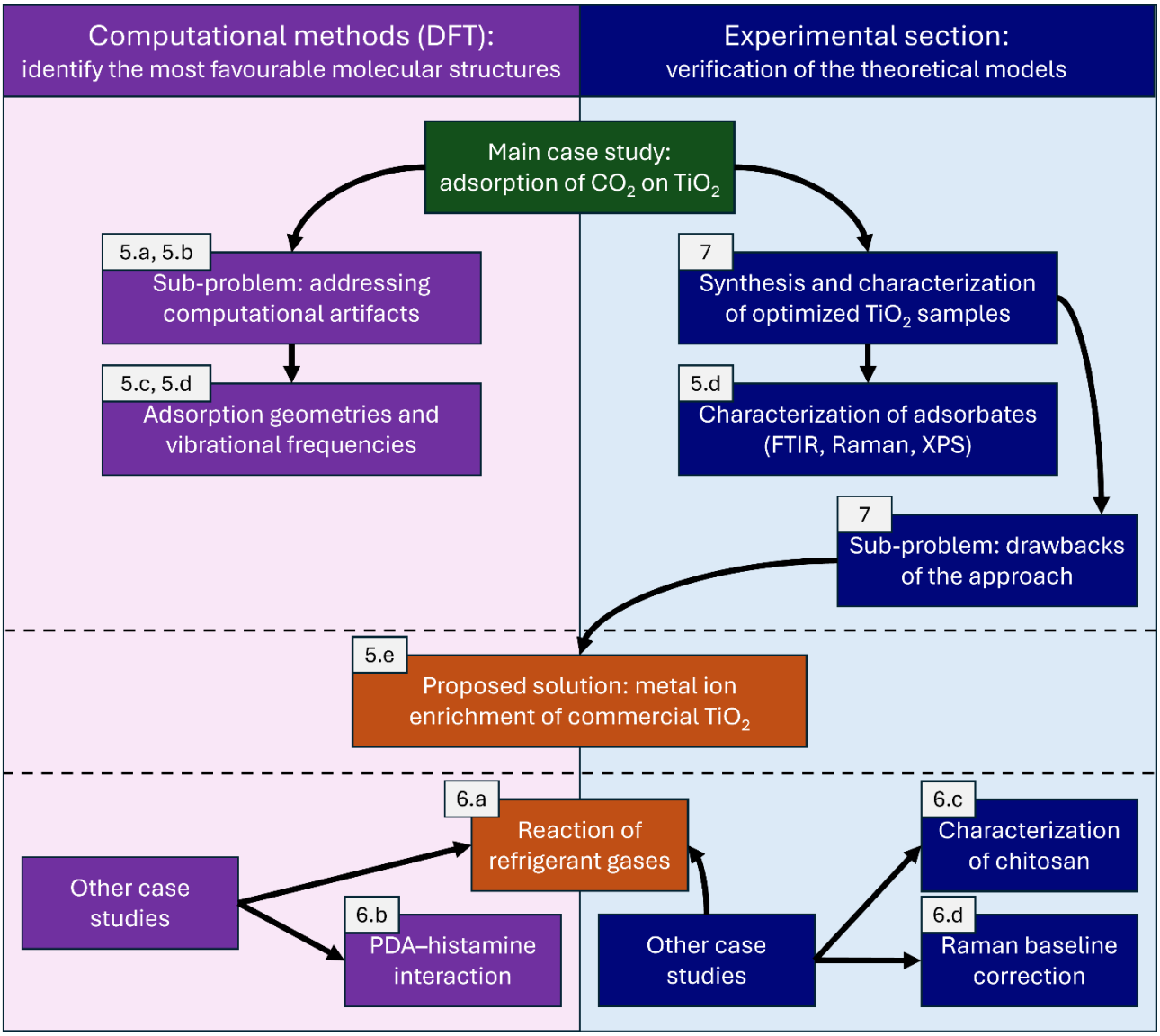



***Figure 3.1:*** *Schematic outline of the research conducted within the scope of this thesis. The positioning of each block within the diagram indicates whether a specific part focuses primarily on computational or experimental analysis. Chapter numbers are explicitly reported to provide a direct reference to the corresponding section.*

Figure 3.1 shows a diagram aimed at visualizing the various phases of the work and mapping them to the different chapters of the thesis. The main section of the work focuses on stoichiometric $TiO_2$, primarily in the anatase crystalline phase. To maximize the accuracy of the performed simulations, a detailed series of convergence tests on different computational parameters became necessary. This involved several parameters that are notoriously the focus of attention during the crucial stage of convergence testing, such as the cut-off energy and the number of k-points used. However, it was observed that structural parameters related to the size of the supercell used and the dimensions of

the slab considered during the simulation can influence certain computational results. Therefore, it is important to highlight how the surface energy associated with a specific exposed crystalline plane and specific adsorption geometries can be influenced by an incorrect choice of computational parameters.

Following this phase, having defined a stable working framework, the foundations were laid for a comparison between two anatase $TiO_2$ surfaces widely studied in the literature, namely those terminating with the (101) and (001) planes. This comparison is necessary because the former represents a highly stable atomic arrangement with a comparatively low surface energy, on which, in general, many adsorption geometries prove to be thermodynamically unstable. Conversely, the latter exhibits high surface energy, thus representing a relatively unstable condition but one that allows for various adsorption geometries. Subsequently, $CO_2$ adsorption geometries on both investigated surfaces were evaluated, and their vibrational frequencies were calculated. This operation is fundamental for any subsequent experimental validation via infrared or Raman spectroscopy.

Considering the results obtained in the computational section of this work, particular attention was devoted to the anatase (001) surface. Consequently, various hydrothermal synthesis procedures were evaluated to obtain a titania sample exposing this specific crystalline plane. This phase raised several critical issues, as many of the attempted procedures—adapted from the literature but with a degree of originality heavily constrained by the available instrumentation and reagents—presented non-negligible intrinsic risks. For this reason, an effort was made to select some of the followed recipes and present them in a dedicated section of the thesis, along with the structural characterizations of the synthesized samples. A further difficulty encountered relates to the identification of the predominantly exposed facets, as certain characterization techniques could prove ineffective.

Following this, the focus was shifted to studying the possible adsorbates on the titania sample exposing the anatase (001) surface, with a specific emphasis on identifying the computationally predicted structures through a comparison with the calculated vibrational frequencies. The accuracy of the simulations was confirmed, as infrared spectroscopy allowed for the observation of vibrational features directly assignable to the most stable CO2 adsorption geometries, specifically in the form of carbonates and bicarbonates. Additional characterizations, such as Raman and XPS, were performed to support the infrared data.

What emerges from both the simulations and the subsequent experimental evidence is the role of water in promoting $CO_2$ adsorption. Indeed, the presence of carbonates was often not observed (via

FTIR and Raman) or appeared more limited (via XPS) in the case of a dry anatase (001) sample, depending on the specific spectroscopic technique used. The addition of a drop of ultrapure water, under ambient atmospheric conditions, led to the spectroscopic detection of the carbonates and bicarbonates, presumably originating from the adsorption of atmospheric $CO_2$.

Having therefore achieved the primary objectives of the thesis—namely, the successful agreement between computational and experimental results—and demonstrated that the anatase (001) surface possesses interesting $CO_2$ adsorption capabilities, the difficulties encountered in obtaining the target sample were nevertheless considered. The intrinsic risks of the synthesis procedure, combined with the limited amount of sample obtainable from a single synthesis batch, remained a constant focus of attention. To this, it must be added that the high surface energy of the facet in question implies significant structural instability; consequently, certain procedures, some of which are necessary, such as thermal treatment, may convert the exposed surface toward more stable facets, such as the aforementioned (101) plane, which possesses limited $CO_2$ adsorption capabilities.

For these reasons, an alternative approach was evaluated, which could lead to a $TiO_2$ sample free of such critical issues while still retaining the targeted adsorption characteristics. A key feature of this method is the use of commercial $TiO_2$, a material that, as previously mentioned, is low-cost and easy to handle. This material is practically ineffective in adsorbing ambient $CO_2$, as it is not specifically synthesized to predominantly expose anatase (001) or other planes with similar properties. The concept, which is currently at a very initial stage, involves incorporating metal ions onto the $TiO_2$ surface via wet-impregnation techniques. Following the washing and drying of the $TiO_2$ powder, a preliminary phase of spectroscopic characterization revealed the presence of spectral features assignable to carbonates and bicarbonates, which likely originated once again from adsorbed ambient $CO_2$. Although this new approach requires further work and is currently in a highly early state, the promising results, combined with its novel character, support future research in this field.

The remaining section of this thesis focuses on collateral studies distinct from the main case study presented above. In these projects, the computational and characterization techniques thoroughly detailed in the previous section played a pivotal role. Across the various investigations reported herein, a theoretical analysis was conducted on the potential reactions of refrigerant gas molecules, hypothesized following the formation of liquid and solid products during thermodynamic testing on a gas mixture. Vibrational spectroscopy contributed to the characterization of the reaction products, providing robust validation for the theoretical findings.

From a purely computational standpoint, the interaction between polydopamine (PDA) and histamine was investigated as part of a broader project aimed at enhancing the sensing capabilities for specific molecules. These computational results proved crucial in elucidating the mechanisms behind the enhanced sensing capabilities observed via Raman spectroscopy.

Furthermore, mathematical pretreatment techniques for spectroscopic data led to the identification of an innovative method to estimate the degree of deacetylation (DDA) in chitosan via infrared spectroscopy. Lastly, within a wider research framework on microplastics, an algorithm capable of correcting the additive baseline in Raman spectra was developed and evaluated.

As previously noted, each of these independent projects will be fully introduced in its respective section of the thesis.

## References


[1] ‘Are There Precious Metals in Catalytic Converters?’ Accessed: Jun. 10, 2026. [Online]. Available: https://www.thermofisher.com/blog/metals/platinum-group-metal-recovery-from-spent-catalytic-converters-using-xrf/

[2] I. Yakoumis, A. M. Moschovi, I. Giannopoulou, and D. Panias, ‘Real life experimental determination of platinum group metals content in automotive catalytic converters’, 2018, doi: 10.1088/1757-899X/329/1/012009.

[3] D. I. Groves, D. Müller, M. Santosh, and C. X. Yang, ‘The heterogeneous distribution of critical metal mineral resources: An impending geopolitical issue’, *Geosystems and Geoenvironment*, vol. 4, no. 1, p. 100288, Feb. 2025, doi: 10.1016/J.GEOGEO.2024.100288.

[4] R. Merget and G. Rosner, ‘Evaluation of the health risk of platinum group metals emitted from automotive catalytic converters’, *Science of The Total Environment*, vol. 270, no. 1–3, pp. 165–173, Apr. 2001, doi: 10.1016/S0048-9697(00)00788-9.

[5] ‘Are There Precious Metals in Catalytic Converters?’ Accessed: Jun. 10, 2026. [Online]. Available: https://www.thermofisher.com/blog/metals/platinum-group-metal-recovery-from-spent-catalytic-converters-using-xrf/

[6] P. Konieczny *et al.*, ‘Effects triggered by platinum nanoparticles on primary keratinocytes’, *Int. J. Nanomedicine*, vol. 8, p. 3963, Oct. 2013, doi: 10.2147/IJN.S49612.

[7] R. A. Baan, ‘Carcinogenic hazards from inhaled carbon black, titanium dioxide, and talc not containing asbestos or asbestiform fibers: recent evaluations by an IARC Monographs Working Group’, *Inhal. Toxicol.*, vol. 19 Suppl 1, no. SUPPL. 1, pp. 213–228, 2007, doi: 10.1080/08958370701497903.

[8] S. Bonetta *et al.*, ‘DNA damage in workers exposed to pigment grade titanium dioxide (TiO2) and association with biomarkers of oxidative stress and inflammation’, *Environ. Toxicol. Pharmacol.*, vol. 105, Jan. 2024, doi: 10.1016/j.etap.2023.104328.

[9] D. B. Warheit and E. M. Donner, ‘Risk assessment strategies for nanoscale and fine-sized titanium dioxide particles: Recognizing hazard and exposure issues’, *Food and Chemical Toxicology*, vol. 85, pp. 138–147, Nov. 2015, doi: 10.1016/J.FCT.2015.07.001.

[10] ‘UK disagrees with EU position on titanium dioxide | Food Safety News’. Accessed: Jun. 10, 2026. [Online]. Available: https://www.foodsafetynews.com/2022/03/uk-disagrees-with-eu-position-on-titanium-dioxide/

[11] ‘E171: EU watchdog says food colouring widely used in UK is unsafe | Food safety | The Guardian’. Accessed: Jun. 10, 2026. [Online]. Available: https://www.theguardian.com/world/2021/may/06/e171-eu-watchdog-says-food-colouring-widely-used-in-uk-is-unsafe

[12] ‘Titanium dioxide (TiO2) as a food additive: Current science report- Canada.ca’. Accessed: Jun. 10, 2026. [Online]. Available: https://www.canada.ca/en/health-canada/services/food-nutrition/reports-publications/titanium-dioxide-food-additive-science-report.html

[13] T. Zhu and S. P. Gao, 'The Stability, Electronic Structure, and Optical Property of TiO2 Polymorphs', *Journal of Physical Chemistry C*, vol. 118, no. 21, pp. 11385–11396, May 2014, doi: 10.1021/JP412462M.

[14] D. R. Eddy *et al.*, 'Heterophase Polymorph of TiO2 (Anatase, Rutile, Brookite, TiO2 (B)) for Efficient Photocatalyst: Fabrication and Activity', *Nanomaterials 2023, Vol. 13, Page 704*, vol. 13, no. 4, p. 704, Feb. 2023, doi: 10.3390/NANO13040704.

[15] S. Bouhadoun *et al.*, 'One step synthesis of N-doped and Au-loaded TiO2 nanoparticles by laser pyrolysis: Application in photocatalysis', *Appl. Catal. B*, vol. 174–175, pp. 367–375, Sep. 2015, doi: 10.1016/J.APCATB.2015.03.022.

[16] J. et al Bender, 'Patent No.: US 6,962,622 B2'.

[17] H. Takahashi and et al., 'Patent No.: US20050228112A1'

[18] Bendavid A. and Martin Philip, 'Review of thin film materials deposition by the filtered cathodic vacuum arc process at CSIRO'.

[19] M. N. Iliev, V. G. Hadjiev, and A. P. Litvinchuk, 'Raman and infrared spectra of brookite (TiO2): Experiment and theory', *Vib. Spectrosc.*, vol. 64, pp. 148–152, Jan. 2013, doi: 10.1016/J.VIBSPEC.2012.08.003.

[20] S. Challagulla, K. Tarafder, R. Ganesan, and S. Roy, 'Structure sensitive photocatalytic reduction of nitroarenes over TiO 2', *Scientific Reports 2017 7:1*, vol. 7, no. 1, pp. 8783-, Aug. 2017, doi: 10.1038/s41598-017-08599-2.

[21] A. Sacco *et al.*, 'Quantification of titanium dioxide (TiO2) anatase and rutile polymorphs in binary mixtures by Raman spectroscopy: an interlaboratory comparison', *Metrologia*, vol. 60, no. 5, p. 055011, Sep. 2023, doi: 10.1088/1681-7575/ACF76D.

[22] K. Schoumacker, C. Geantet, M. Lacroix, E. Puzenat, C. Guillard, and J. M. Herrmann, 'Photocatalytic synthesis of thio-organic compounds: case study of propan-1-thiol', *J. Photochem. Photobiol. A Chem.*, vol. 152, no. 1–3, pp. 147–153, Sep. 2002, doi: 10.1016/S1010-6030(02)00208-3.

[23] B. Ohtani, O. O. Prieto-Mahaney, D. Li, and R. Abe, 'What is Degussa (Evonik) P25? Crystalline composition analysis, reconstruction from isolated pure particles and photocatalytic activity test', *J. Photochem. Photobiol. A Chem.*, vol. 216, no. 2–3, pp. 179–182, Dec. 2010, doi: 10.1016/J.JPHOTOCHEM.2010.07.024.

[24] A. Alonso-Tellez, R. Masson, D. Robert, N. Keller, and V. Keller, 'Comparison of Hombikat UV100 and P25 TiO2 performance in gas-phase photocatalytic oxidation reactions', *J. Photochem. Photobiol. A Chem.*, vol. 250, pp. 58–65, Dec. 2012, doi: 10.1016/J.JPHOTOCHEM.2012.10.008.

[25] M. Á. López Zavala, S. A. Lozano Morales, and M. Ávila-Santos, 'Synthesis of stable TiO2 nanotubes: effect of hydrothermal treatment, acid washing and annealing temperature', *Heliyon*, vol. 3, no. 11, p. e00456, Nov. 2017, doi: 10.1016/J.HELIYON.2017.E00456.

[26] B. Ohtani, O. O. Prieto-Mahaney, D. Li, and R. Abe, 'What is Degussa (Evonik) P25? Crystalline composition analysis, reconstruction from isolated pure particles and photocatalytic activity test', *J.*

*Photochem. Photobiol. A Chem.*, vol. 216, no. 2–3, pp. 179–182, Dec. 2010, doi: 10.1016/J.JPHOTOCHEM.2010.07.024.

[27] L. Lo Presti *et al.*, 'Direct measurement and modeling of spontaneous charge migration across anatase–brookite nanoheterojunctions', *J. Mater. Chem. A Mater.*, vol. 9, no. 12, pp. 7782–7790, Mar. 2021, doi: 10.1039/D1TA01040A.

[28] G. Di Liberto, V. Pifferi, L. Lo Presti, M. Ceotto, and L. Falciola, 'Atomistic Explanation for Interlayer Charge Transfer in Metal–Semiconductor Nanocomposites: The Case of Silver and Anatase', *Journal of Physical Chemistry Letters*, vol. 8, no. 21, pp. 5372–5377, Nov. 2017, doi: 10.1021/ACS.JPCLETT.7B02555.

[29] L. Collado *et al.*, 'Unravelling charge dynamic effects in photocatalytic CO2 reduction over TiO2: Anatase vs P25', *Catal. Today*, vol. 423, p. 114279, Nov. 2023, doi: 10.1016/J.CATTOD.2023.114279.

[30] D. R. Eddy *et al.*, 'Heterophase Polymorph of TiO2 (Anatase, Rutile, Brookite, TiO2 (B)) for Efficient Photocatalyst: Fabrication and Activity', *Nanomaterials*, vol. 13, no. 4, p. 704, Feb. 2023, doi: 10.3390/NANO13040704.

# 4. Overview on the computational methods

Capabilities of computational calculations in the chemistry field were characterized for long time by several limitations. The first level of complexity stems from the many-body problem, which is the impossibility of analytically solving the mutual interaction among three or more physical objects[1]. Although this phenomenon is not unique to chemistry, it becomes particularly evident in this domain due to the necessity of considering numerous particles to properly describe an actual system.

Secondly, it is worth noting the limitations of classical theory in describing atomic and subatomic structures. Wave-particle duality and the resulting observable macroscopic phenomena highlight the necessity of quantum formalism when length scales approach the microscopic level. However, the intrinsic probabilistic nature of subatomic motion, lacking absolute determinism, introduces further computational complexity, which is of crucial relevance when studying the highly miniaturized systems typical of chemical problems.

Solving the Schrödinger equation for complex chemical systems therefore requires a critical compromise between physical accuracy and computational feasibility. To bypass this limitation, theoretical chemistry has developed two conceptually distinct approaches. On the one hand, force-field-based methods do not consider an explicit description of electrons, treating atoms as classical spheres interconnected by analytical potentials; this simplification allows for the simulation of macromolecular systems over extended timescales at a reasonable computational cost[2], [3].

These methods are characterized by decomposing the potential energy as a sum of simpler terms, generally divided into contributions originating from actual chemical bonds and Coulombic contributions[4]. Although this approximation allows for rapid calculations even for highly complex molecular systems, it introduces a significant approximation that must be empirically corrected. Therefore, these methods cannot be defined ab initio.

For applications where such approximations are not tolerated, the convenience is to consider methods that include a rigorous definition of the electronic structure. To achieve this, these quantum mechanical approaches rely on the Born-Oppenheimer approximation, according to which it is possible to uncouple the motion of light electrons from that of heavy nuclei[5]. Two frameworks can be defined that attempt to solve the problem differently: those based on the Hartree-Fock (HF) model and Density Functional Theory (DFT).

The Hartree-Fock method includes a wavefunction that depends on the spatial and spin coordinates of all electrons in the system, the resolution of which often proves to be computationally highly complex, thus requiring mathematical shortcuts to simplify the calculation. Without going too deeply into the details of the method, each electron is influenced by the others, which are treated as an electron cloud where the quantum exchange energy plays a significant role, while the electron correlation, which arises from instantaneous electron-electron repulsions, is neglected[6], [7].

In contrast, DFT replaces the characteristic HF wavefunction with the electron density, which is a single term defined by just three spatial coordinates. Both exchange and correlation terms are explicitly considered through various approaches that represent clear trade-offs between accuracy and computational cost[8]. Notably, the exact exchange term from HF can still be incorporated; while this increases computational complexity, it offers the potential to achieve a high degree of accuracy[9].

Generally, by accounting for electron correlation, DFT can yield more precise values for bond energies and overall higher accuracy. For this reason, DFT is considered significantly more advantageous than HF. In fact, HF is often replaced by so-called post-Hartree-Fock methods, which, however, will not be further explored within the scope of this thesis.

Considering the computational time required by the two methods, DFT and HF tend to scale almost identically with respect to the complexity of the problem[10]. This would seem to contradict what is theoretically stated, as one might expect HF to suffer more given its reliance on an explicit many-body wavefunction, while DFT formally depends only on the simpler three-dimensional electron density. However, practical Kohn-Sham DFT introduces a set of one-electron orbitals to calculate the non-interacting kinetic energy. Consequently, solving the Kohn-Sham equations requires an iterative self-consistent field (SCF) scheme whose algebraic structure is strictly analogous to that of the Hartree-Fock method. As a result, both methods must compute and manipulate a comparable number of matrices and spatial integrals over molecular orbitals, leading to a similar conventional scaling factor, typically on the order of $O(N^4)$ or $O(N^3)$, with respect to the number of basis functions N[11].

It must be noted that certain optimized algorithms, such as Schwarz screening, allow for a significant simplification of the calculations[12]. These methods typically rely on conditional screening criteria to filter out negligible integrals before they are computed. This drastically reduces the number of operations required, thereby abating the overall computational complexity.

In addition to the well-known quantum foundations upon which DFT is built, it is worth highlighting the theoretical pillar given by the Hohenberg-Kohn theorems[13], [14]. They establish the formal exactness of DFT in the ground state, because:

- The ground-state properties of a non-degenerate many-electron system are described by functionals of the electron density alone.
- The ground-state energy corresponds to the minimum value of the total energy functional with respect to the electron densities for which it is defined.

This mathematical framework aligns perfectly with the fundamental postulate of standard quantum mechanics, which states that the wavefunction embodies the totality of a system's physical information. Since the density uniquely determines the ground-state wavefunction, it follows that all observables of this state can be rigorously deduced from the electron density alone.

Once the capabilities of DFT relative to other methods have been defined, it is important to introduce the concept of the pseudopotential, as it represents a fundamental methodology for reducing computational costs[15]. It is based on the idea that not all electrons within an atom are essential for defining its behaviour; thus, a detailed representation of the inner-shell electrons can be omitted in favour of the outer ones. The former, referred to as core electrons within this framework, can be replaced by a simpler pseudo-wavefunction that avoids rapid oscillations, consequently requiring fewer parameters to be managed. The latter, designated as valence electrons, have their wavefunction fully retained to ensure an accurate representation of the atom's behaviour within the system. Generally, these valence states include not only the strict outermost valence electrons but also certain semi-core electrons belonging to the subshells immediately lower in energy. How many valence electrons are explicitly considered remains a methodological detail which falls outside of the scope of this introduction.

Among the families of pseudopotentials, those applied within the context of this thesis are the Norm-Conserving (NC) pseudopotentials. These are characterized by imposing the condition that the total charge enclosed within the core region remains unaltered by the introduced approximation[16]. Although their commonness, they typically require higher cut-off energy values for plane-wave basis sets (this point is further expanded upon in the chapter regarding convergence tests). Other options include Ultrasoft (US) pseudopotentials, in which the charge constraint is relaxed, and those

employing the Projector Augmented-Wave (PAW) method[17], [18]. The latter retains the computational advantages introduced by US pseudopotentials while allowing for a mathematical transformation to reconstruct the exact wavefunction.

A final aspect to consider is, as previously mentioned, the approximation of the exchange-correlation functional. Between the two main approaches, one can distinguish the Local Density Approximation (LDA), which is based on the local density value, and the Generalized Gradient Approximation (GGA), which instead considers both the local value and its gradient[19].

Having clarified the core principles of DFT, the focus now shifts to some of the possible calculations that can be performed. Many of these are based on the Self-Consistent Field (SCF) method, which is the iterative mathematical procedure used to solve the self-consistent relationship between the electron density and the potential acting upon it[20]. Specifically, the process begins with the generation of a trial electron density and the solution of the Kohn-Sham equations (which replace the Schrödinger equation) to obtain the wavefunction corresponding to that density. Since the new electron density derived from the calculated wavefunction does not necessarily coincide with the previously assumed one, the error between the two is evaluated. By defining a threshold parameter, the cycle terminates once the error falls below this specified limit.

Once the wavefunction of the electron density is known, it is then possible to calculate the force acting on the atoms. The SCF cycle can therefore be repeated after displacing the atoms in accordance with the exerted force. This is of fundamental importance when optimizing atomic positions to reach the lowest energy configuration (relax), optionally varying the dimensions of the supercell as well (vc-relax). The second type of calculation has proven essential for representing crystal cells starting from experimental configurations, whereas the first is typically used for calculating molecular systems or, specifically within the scope of this thesis, the adsorption of molecules on surfaces. A further possibility is to perform this type of calculation while maintaining the total energy of the system constant (md, molecular dynamics), with the latter defined as the sum of the total energy and the kinetic energy. By including this term, temperature dependence also becomes accessible. In this manner, the system can be evolved for an arbitrary number of iterations, corresponding to a predetermined simulation time.

Regarding the calculation of a system's vibrational modes, several computational techniques are available. Most importantly within the scope of this thesis, it is worth emphasizing that many of these methods incorporate only the harmonic approximation. Although slightly different approaches exist

that nonetheless lead to analogous results, the standard procedure involves calculating the second derivative of the total energy, as described within the Density Functional Perturbation Theory[21], [22]. From this, the vibrational modes (phonons) can be obtained by evaluating the response of the electronic system to the infinitesimal perturbation caused by the displacement of the atomic nuclei.

This approach, however, was not considered sufficient to obtain an accurate representation of a system's vibrational frequencies, primarily because the anharmonic component is neglected. To account for this, it is appropriate to compute trajectories from which the velocity of each atom can be extracted at every time step. By means of a Fourier transform, it is then possible to transition from the time domain to the frequency domain, thereby obtaining the vibrational spectrum of the system. Generally, it can be observed that this operation causes a shift compared to the modes calculated under the harmonic approximation; this shift acts as a correction that effectively enhances the predictive capability of the simulation.

All the simulations presented hereinafter were performed using the Quantum ESPRESSO (QE) software suite, primarily utilizing its pw.x and ph.x modules[23], [24]. The former was employed to execute the various SCF-based algorithms, while the latter was used to calculate the vibrational modes under the harmonic approximation. It should be noted that anharmonic corrections are not natively available within the Quantum ESPRESSO package; therefore, the semisoft.unimi.it web platform was utilized to calculate the power spectrum[25], [26], [27].

The Velocity-Verlet (VV) algorithm was selected to simulate the molecular dynamics required for calculating the frequencies and intensities of the vibrational modes, as it is considered more accurate than other counterparts in defining positions and velocities at each simulation step. This proved to be a critical phase, since Quantum Espresso made this specific algorithm available only in its most recent versions. The current version 7.5, published in 2025, allows the use of this algorithm within ionic dynamics simulations to integrate Newton's equations of motion. Consequently, it was impossible to perform a systematic validation of its performance and, more importantly, to establish a supporting protocol and set of algorithms capable of making atomic velocities and positions available as required by the other analysis tools, such as the previously mentioned software for computing the power spectrum.

For these reasons, given the in-house availability of an additional routine to be integrated into the open-source Quantum Espresso code for dynamics calculations via the VV algorithm, its use was preferred, as it was already designed to arrange the required data in the correct format. The main

modification concerns the calculation of atomic nuclear velocities and their positions at each iteration through the integration of Newton's equations of motion. This is achieved by utilizing the previous velocities and positions, the current acceleration, and, specifically for the positions, the current velocity. The acceleration is defined as a function of the nuclear masses and the forces acting upon them, with the latter being derived from the SCF cycle. Notably, the initial values for the atomic velocities were computed by integrating the Hessian matrix obtained via the phonon method. The modifications reported here are therefore very limited; to these, routines for printing the nuclear coordinates and their velocities into dedicated files at each iteration must obviously be added.

## References


[1] I. E. Perakis and T. V. Shahbazyan, 'Many-body correlation effects in the ultrafast non-linear optical response of confined Fermi seas', *Surf. Sci. Rep.*, vol. 40, no. 1–2, pp. 1–74, Oct. 2000, doi: 10.1016/S0167-5729(00)00009-1.

[2] O. Sadiku-Agboola and E. R. Sadiku, 'Theoretical Modeling of Nanostructured Formation in Polymer Blends', *Nanostructured Polymer Blends*, pp. 33–99, Jan. 2014, doi: 10.1016/B978-1-4557-3159-6.00003-1.

[3] S. Malola and H. Häkkinen, 'Prospects and challenges for computer simulations of monolayer-protected metal clusters', doi: 10.1038/s41467-021-22545-x.

[4] L. Monticelli and D. P. Tieleman, 'Force Fields for Classical Molecular Dynamics', pp. 197–213, 2013, doi: 10.1007/978-1-62703-017-5_8.

[5] M. Born and R. Oppenheimer, 'Zur Quantentheorie der Molekeln', *Ann. Phys.*, vol. 389, no. 20, pp. 457–484, 1927, doi: 10.1002/ANDP.19273892002.

[6] P. Echenique and J. L. Alonso, 'A mathematical and computational review of Hartree-Fock SCF methods in Quantum Chemistry', *Molecular Physics introSCF Molecular Physics*, vol. 00, no. 00, pp. 1–64, 2024, doi: 10.1080/0026897YYxxxxxxxx.

[7] M. Šulka, K. Šulková, P. Jurečka, and M. Dubecký, 'Dynamic and Nondynamic Electron Correlation Energy Decomposition Based on the Node of the Hartree–Fock Slater Determinant', *J. Chem. Theory Comput.*, vol. 19, no. 22, pp. 8147–8155, Nov. 2023, doi: 10.1021/ACS.JCTC.3C00828.

[8] P. Makkar and N. N. Ghosh, 'A review on the use of DFT for the prediction of the properties of nanomaterials', *RSC Adv.*, vol. 11, no. 45, pp. 27897–27924, Aug. 2021, doi: 10.1039/D1RA04876G.

[9] S. Śmiga and L. A. Constantin, 'Unveiling the Physics Behind Hybrid Functionals', *J. Phys. Chem. A*, vol. 124, no. 27, pp. 5606–5614, Jul. 2020, doi: 10.1021/ACS.JPCA.0C04156.

[10] A. L. Botelho, Y. Shin, M. Li, L. Jiang, and X. Lin, 'Unified Hamiltonian for conducting polymers', *Journal of Physics: Condensed Matter*, vol. 23, no. 45, p. 455501, Oct. 2011, doi: 10.1088/0953-8984/23/45/455501.

[11] P. Echenique and J. L. Alonso, 'A mathematical and computational review of Hartree-Fock SCF methods in Quantum Chemistry', *Molecular Physics introSCF Molecular Physics*, vol. 00, no. 00, pp. 1–64, 2024, doi: 10.1080/0026897YYxxxxxxxx.

[12] D. L. Strout and G. E. Scuseria, 'A quantitative study of the scaling properties of the Hartree–Fock method', *J. Chem. Phys.*, vol. 102, no. 21, pp. 8448–8452, Jun. 1995, doi: 10.1063/1.468836.

[13] V. Sahni, 'The Hohenberg-Kohn Theorems and Kohn-Sham Density Functional Theory', *Quantal Density Functional Theory*, pp. 99–123, 2004, doi: 10.1007/978-3-662-09624-6_4.

[14] P. Hohenberg and W. Kohn, 'Inhomogeneous Electron Gas', *Physical Review*, vol. 136, no. 3B, p. B864, Nov. 1964, doi: 10.1103/PhysRev.136.B864.

[15] S. J. Jenkins, 'Spin-polarised surfaces: Current state of Density Functional Theory investigations', *Theoretical and Computational Chemistry*, vol. 15, pp. 261–295, Jan. 2004, doi: 10.1016/S1380-7323(04)80022-0.

[16] D. R. Hamann, M. Schlüter, and C. Chiang, 'Norm-Conserving Pseudopotentials', *Phys. Rev. Lett.*, vol. 43, no. 20, p. 1494, Nov. 1979, doi: 10.1103/PhysRevLett.43.1494.

[17] D. Vanderbilt, 'Soft self-consistent pseudopotentials in a generalized eigenvalue formalism', *Phys. Rev. B*, vol. 41, no. 11, p. 7892, Apr. 1990, doi: 10.1103/PhysRevB.41.7892.

[18] P. E. Blöchl, 'Projector augmented-wave method', *Phys. Rev. B*, vol. 50, no. 24, p. 17953, Dec. 1994, doi: 10.1103/PhysRevB.50.17953.

[19] Y. M. Juan, E. Kaxiras, and R. G. Gordon, 'Use of the generalized gradient approximation in pseudopotential calculations of solids', *Phys. Rev. B*, vol. 51, no. 15, p. 9521, Apr. 1995, doi: 10.1103/PhysRevB.51.9521.

[20] N. D. Woods, M. C. Payne, and P. J. Hasnip, 'Computing the self-consistent field in Kohn–Sham density functional theory', *Journal of Physics: Condensed Matter*, vol. 31, no. 45, p. 453001, Aug. 2019, doi: 10.1088/1361-648X/AB31C0.

[21] R. Conte, C. Aieta, M. Cazzaniga, and M. Ceotto, 'A Perspective on the Investigation of Spectroscopy and Kinetics of Complex Molecular Systems with Semiclassical Approaches', *J. Phys. Chem. Lett.*, vol. 15, no. 30, pp. 7566–7576, Aug. 2024, doi: 10.1021/ACS.JPCLETT.4C01338.

[22] V. Barone, M. Biczysko, J. Bloino, M. Borkowska-Panek, I. Carnimeo, and P. Panek, 'Toward anharmonic computations of vibrational spectra for large molecular systems', *Int. J. Quantum Chem.*, vol. 112, no. 9, pp. 2185–2200, May 2012, doi: 10.1002/QUA.23224;WGROUP:STRING:PUBLICATION.

[23] P. Giannozzi *et al.*, 'Advanced capabilities for materials modelling with Quantum ESPRESSO', *Journal of Physics: Condensed Matter*, vol. 29, no. 46, p. 465901, Oct. 2017, doi: 10.1088/1361-648X/AA8F79.

[24] P. Giannozzi *et al.*, 'QUANTUM ESPRESSO: a modular and open-source software project for quantumsimulations of materials', *Journal of Physics: Condensed Matter*, vol. 21, no. 39, p. 395502, Sep. 2009, doi: 10.1088/0953-8984/21/39/395502.

[25] R. Conte, M. Gandolfi, D. Moscato, C. Aieta, S. Valtolina, and M. Ceotto, 'Vibrational Spectroscopy Through Time Averaged Fourier Transform of Autocorrelated Molecular Dynamics Data: Introducing the Free SEMISOFT Web-Platform', *J. Comput. Chem.*, vol. 46, no. 12, p. e70118, May 2025, doi: 10.1002/JCC.70118;WGROUP:STRING:PUBLICATION.

[26] R. Conte *et al.*, 'Anharmonicity and quantum nuclear effects in theoretical vibrational spectroscopy: a molecular tale of two cities', *Theoretical Chemistry Accounts 2023 142:5*, vol. 142, no. 5, pp. 53-, May 2023, doi: 10.1007/S00214-023-02993-Y.

[27] M. Gandolfi *et al.*, 'Semisoft- Home', A web platform for time averaged Fourier transformed of autocorrelated data. Accessed: Jun. 11, 2026. [Online]. Available: https://semisoft.unimi.it/

# 5. Carbon dioxide adsorption on titanium dioxide

## 5.a Convergence tests and the importance of supercell dimensions

### Convergence tests on the anatase unit cell

Convergence tests play a fundamental role in defining the computational parameters for simulations, as they are highly specific to the investigated material. Despite the noteworthy effort in many published works to report all the parameters necessary to ensure replicability, descriptions of how simulations were executed are often incomplete. This lack of detail makes it highly difficult to reproduce such calculations with perfect accuracy.

Because of this premise, it is believed that a sufficiently extensive analysis of the convergence tests performed to ensure robust simulations is necessary. This is what numerous educational tutorials would suggest, as they emphasize the importance of these tests to improve the quality of subsequent calculations. Since the process used to establish the calculated values is often not adequately described, making associations also proves difficult. For this reason, the entire process will be described in its entirety.

Among the possible frameworks to define convergence tests, the one chosen within this thesis focuses primarily on the crystal cell[1]. Although this is a valid option, it must be mentioned that this is just one of the possible options to perform robust convergence tests[2]. This second procedure finds its theoretical foundations in the fact that, if the work specifically concerned the study of interactions between molecule and surface, it could be more relevant to verify that a small variation in the computational parameters does not cause a profound change in the adsorption geometries and energies, or distortions in the surface itself.

To perform robust convergence tests, it is first necessary to identify which computational parameters make sense to treat as variables and which to define as constants. The latter must inevitably show very stringent values, as more permissive thresholds could invalidate the effort made in defining the best options for the variables. By quickly checking the Quantum Espresso user guides, and particularly the pw.x software included in the package, one quickly understands how each simulation could be

influenced by hundreds of different variables[3]. Obviously, only a limited portion of them can cause appreciable variations in the output of the specific calculation for the specific system.

To better clarify this statement, one can mention, for example, the possibility of performing smearing to make simulations less computationally expensive[4]. Smearing introduces fractional occupancies around the Fermi level, thereby eliminating energy discontinuities and ensuring stable convergence in conductive systems. Obviously, this could introduce an element of inaccuracy, as the exact energy of these electrons might not be adequately estimated. However, clearly, the system under consideration must possess electrons energetically close to the Fermi level, a characteristic typical of metals or otherwise conductive materials. For this reason, introducing smearing in the case of semiconducting or insulating materials might cause no difference. By extension, in these cases, convergence tests on this parameter might not be relevant, given that the use of the parameter itself is useless.

Excluding therefore the hundreds of parameters that are not directly relevant, as they can cause only minimal or totally null variations in the output of a simulation, it is noted that only a few variables can assume critical importance. These generally represent energy thresholds, to which, however, the employed K-points must also be added. Below is a brief description of a selection of these variables, keeping in mind, however, that others could potentially have a certain relevance. At the end of this chapter, an example of an input file used for the calculation of an anatase crystal cell will be provided.

- ecutwfc: Kinetic energy cutoff (expressed in Rydberg) for the plane waves used in the calculation of wave functions. This value determines the size of the mathematical basis of the system: a higher value increases the precision of the calculation but significantly increases the computational time and the required memory.

- etot_conv_thr: Convergence threshold on the total energy (expressed in atomic units) during relaxation. The geometric convergence criterion is satisfied when the total energy difference between two consecutive self-consistent field (scf) steps falls below this value, declaring the end of the structural optimization.

- forc_conv_thr: Similar to the previous one but referring to forces (expressed in atomic units). The criterion is satisfied when the difference between all forces in two consecutive scf steps is lower than this value.

- conv_thr: Convergence threshold internal to a scf step; the criterion is satisfied when the estimated error on the calculated energy is lower than this value.
- K_POINTS: Sampling points in the reciprocal space used to discretize the first Brillouin Zone of the crystal.

Among these parameters, convergence tests are typically performed on the cutoff energy ($E_{cut}$) and k-points. Including the other thresholds in the previous description is necessary because these values were set to specific constants rather than using the software defaults. It should be noted that the computational complexity of a self-consistent field (SCF) cycle scales linearly with the number of k-points and roughly to the power of 3/2 with the ecutwfc value[5].

A crucial factor in defining a proper convergence test is selecting the appropriate output variable and the condition for success. Total energy is often chosen as the dependent variable. In this approach, convergence is achieved when the difference in total energy between two consecutive steps falls below a specified threshold. Since the simulation must optimize both atomic positions and cell parameters, a variable-cell relaxation ('vc-relax') calculation was employed.

The convergence test applies the previously described criterion to determine the optimal kinetic energy cutoff ($E_{cut}$) and k-points grid. The procedure involves progressively increasing $E_{cut}$ in steps of 5 Ry between successive calculations. Meanwhile, the reciprocal space sampling is optimized by expanding the k-points grid dimensions by one unit along each spatial direction at each step. To minimize the total computational cost, the two variables are treated independently: during the k-points convergence test, $E_{cut}$ is fixed at 60 Ry; subsequently, the optimized k-points grid is used to perform the $E_{cut}$ convergence test. The convergence point is defined when the variation in $E_{tot}$ between two consecutive steps does not exceed $10^{-3}$ Ry (~1.3 kJ/mol).

Convergence test here reported refers to the primitive cell of anatase (6 atoms), as visible in the example reported as appendix.

Since the unit cell dimensions satisfy $c > a = b$, it is preferable and faster to choose $k_a$ and $k_b$ (the number of k-points along the a and b axes) larger than kc. When the structural differences between cell parameters are small—as in the present case of the anatase primitive cell—a single-unit difference should suffice. This stems from the fact that sampling occurs in reciprocal space, meaning that the products *a*ka*, *b*kb*, and *c*kc* should remain approximately constant. A separate test,

omitted here for brevity, in which the number of k-points along each direction was optimized independently, yielded analogous results to the ones here presented.

The initial crystal lattice parameters and atomic positions were obtained from experimental data in .cif format, retrieved from the *Crystallography Open Database[6], [7]*. Since the original file refers to the conventional cell of anatase, the conversion to the primitive cell was performed using the cif2cell Linux package[8].

The experimental origin of the initial data may not sufficiently guarantee that the Density Functional Theory (DFT) calculations yield results consistent with reality, due to the potential presence of local minima. For this reason, three consecutive variable-cell relaxation (vc-relax) calculations were performed to ensure consistency and uniformity in the results.

The differences in the total energy values $E_{tot}$ between consecutive steps of the convergence test on k-points is reported in Figure 5.a.1. The convergence criterion is fully satisfied when transitioning from the 4x4x3 grid to the 5x5x4 grid, as indicated by the rightmost point in the plot. For the sake of completeness, the figure also displays the values obtained from the first and second series of geometric optimizations, although only the data from the third and final series are considered relevant for the final convergence.

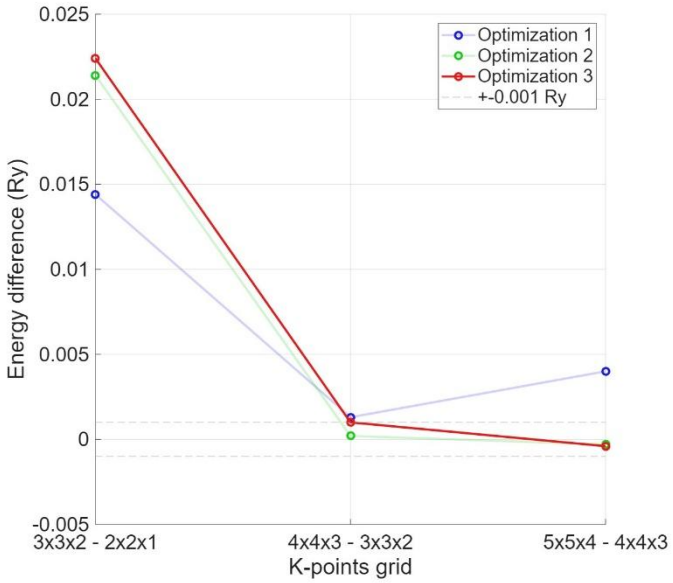


***Figure 5.a.1:*** *K-points convergence test for an anatase primitive cell. The x-axis shows the specific calculation used to determine the corresponding energy difference plotted on the y-axis. The energy cutoff $E_{cut}$ is heuristically set to 60 Ry and will be subsequently refined in the dedicated test.*

Once the 4x4x3 k-points grid was determined to be optimal according to the established convergence criterion, a new convergence test specifically for the energy cutoff $E_{cut}$ was performed, maintaining the same settings and thresholds. This selected grid was kept fixed for the subsequent optimization steps, during which $E_{cut}$ was varied in increments of 5 Ry.

Figure 5.a.2 illustrates the convergence test as a function of $E_{cut}$. The value reported for each step refers to the energy difference relative to the previous step (e.g., $\Delta E_{55} = E_{55} - E_{50}$). The convergence criterion is met at $E_{cut}$ = 80 Ry, as the energy variation at the "85" data point falls below the fixed threshold of 0.001 Ry.

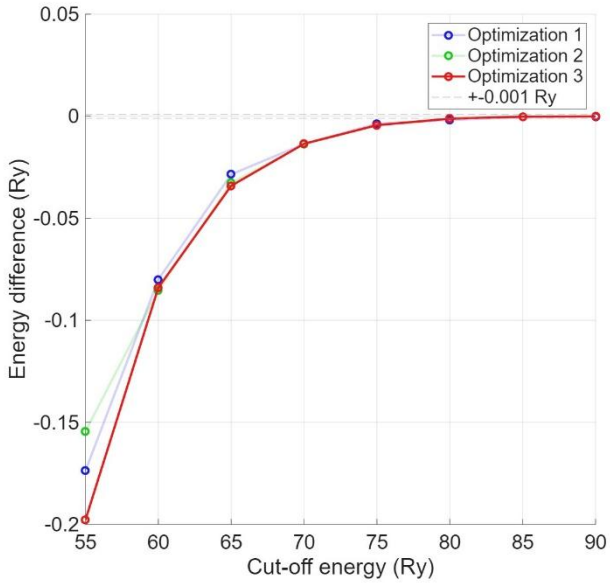



***Figure 5.a.2:*** *Energy cutoff $E_{cut}$ convergence test for an anatase primitive cell. The value on the x-axis satisfies the equation $E_x = E_x - E_{x-5}$. The k-points are generated using a uniform 4x4x3 grid, which was identified as optimal in the previous convergence test.*

Once the optimal parameter combination was determined (Ecut=80, k-points=4x4x3), the resulting optimized crystal cell structure was obtained, as illustrated in Figure 5.a.3. The lattice parameters, converted back to the conventional cell, are listed in Table 5.a.1. The comparison with experimental data demonstrates excellent agreement, thereby confirming the accuracy and reliability of the performed convergence tests.

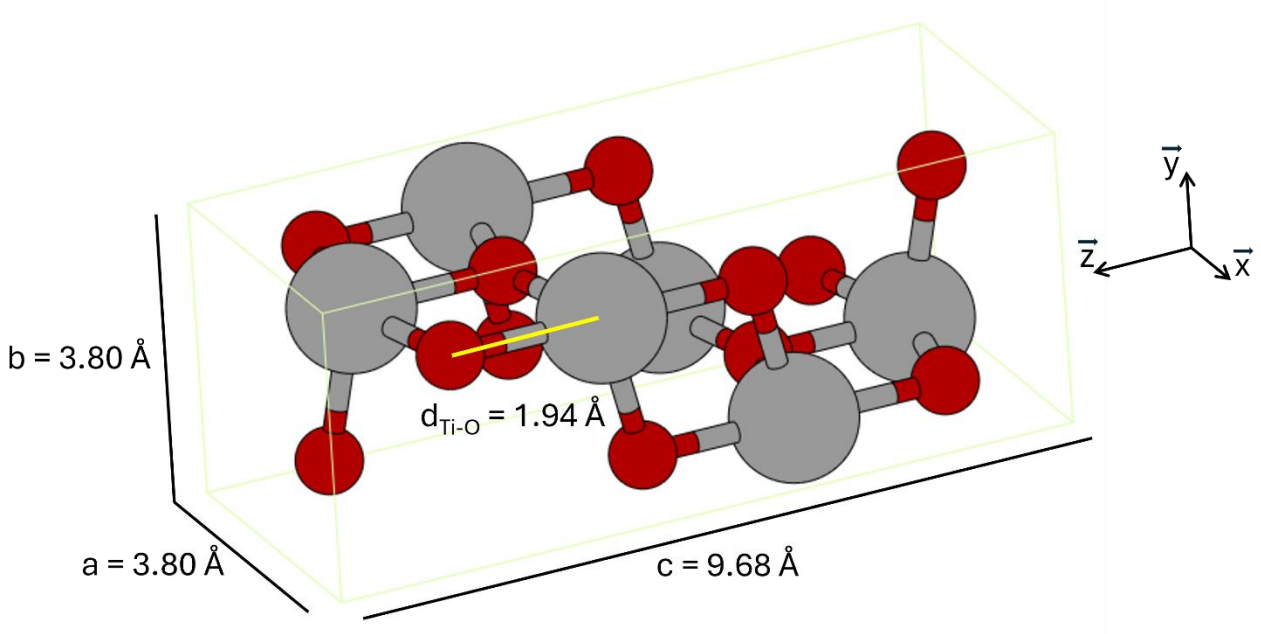



***Figure 5.a.3:*** *Optimized conventional unit cell of anatase.*

| | Optimized cell | Weirich et al (2000)[7] | Aidid et al (2025)[9] |
|---|---|---|---|
| a | 3.80 | 3.77 | 3.79 |
| b | 3.80 | 3.77 | 3.79 |
| c | 9.68 | 9.43 | 9.52 |
| Volume | 139.8 | 134.1 | 136.4 |
| $d_{Ti-O}$ | 1.94 | 1.92 | ND |

***Table 5.a.1:*** *Lattice parameters and Ti–O bond lengths for the optimized crystal cell compared with literature values. The initial cell parameters before optimization are sourced from Weirich et al. (2000). All the values are in Å or Å$^3$.*

Starting from the obtained unit cell, it was possible to construct the anatase surfaces already in the second part of this chapter. The methodology applied herein is general and follows a systematic approach; therefore, this procedure is expected to be readily applicable to numerous other computational contexts, including those structurally distinct from the case study presented here.

## Supercell dimensions: a critical hidden factor

A parameter that is often overlooked but which, as will be demonstrated later, plays a crucial role is the supercell dimensions. The supercell is defined by three vectors that span the volume within which the atoms are arranged and represents the minimum unit that is repeated infinitely due to periodicity.

From a purely mathematical point of view, this is identical to what has been described for the unit cell; the difference lies in the fact that using the term supercell implies it is larger in size, suitable for containing several crystal units and optionally including a vacuum region in which to position the molecules prior to their adsorption.

Considering the results that will be presented later in this chapter, it will emerge how the lateral dimensions of the supercell can play a fundamental role in the obtained results. However, it is deemed necessary to also describe the vertical coordinate; while it undoubtedly represents an important element, being the most frequently investigated, it does not actually give rise to any hidden issues.

It is necessary to distinguish the cell parameters *(a, b, c)* from those of a supercell, hereinafter defined as *(a', b', c')*. For convenience, they will be considered orthogonal. This does not result in a loss of generality, since, in the case of a surface, it is possible to consider solely the magnitude of the vector itself, without dependence on the relative angles formed between them. This does not apply to the unit cell, nor when the atomic positions in space are expressed as a function of the supercell coordinates. This is a consequence of the geometric properties of generic elements arranged in a space and is not specifically linked to the physical or chemical properties of a system. It is not possible to extend this consideration to a computational calculation lacking periodicity.

In surface generation, the unit cell is replicated *m x n x o* times, where the three variables correspond to the number of repetitions along the *(x, y, z)* axes, respectively. Without loss of generality, the *z*-axis is conventionally identified as the vertical coordinate. It follows that, in surface generation, the length of the *c'* vector will be oversized compared to *o*c*, as it is necessary to include a vacuum gap to simulate that the atoms are exposed, thereby forming a surface.

The value $v = c' - o * c$ is of considerable importance, as it defines the thickness of the vacuum volume within the supercell. When the value of *v* is limited, there is a risk of mirror interactions between atoms belonging to a surface and those belonging to the surface replicated by periodicity in the *z* direction. A graphical example illustrating this issue is reported in Figure 5.a.4. Normally, this does not represent a critical factor, and it is preferred to assign an arbitrarily large value to v to exclude this type of interaction. Commonly used values range from 15 to 25 Å, but they may also depend on the system under study[10]. Due to these considerations, an exhaustive discussion regarding the value of v is not necessary: if this value is sufficiently large, small variations are negligible.

Among the o layers along the z-axis, fixed ones must be distinguished from the free ones. As fixed atoms cannot move during optimizations or dynamics, their role is to effectively simulate that the bulk of the surface is solid and therefore cannot excessively deform due to the stresses arising from the introduction of the vacuum gap. The most accurate, albeit utopian, case scenario would feature a surface vertically described by numerous fixed layers at the bottom and numerous free layers above them. This clashes severely with the required computational time, which explodes as the number of atoms in the system increases. For this reason, a trade-off is often required. Interestingly, in the case study of titania, no consensus appears in the literature among different authors, who propose surfaces characterized by a variable number of fixed and total layers. Table 5.a.2 reports, for information purposes, some choices found in the literature to represent a (001) anatase slab.

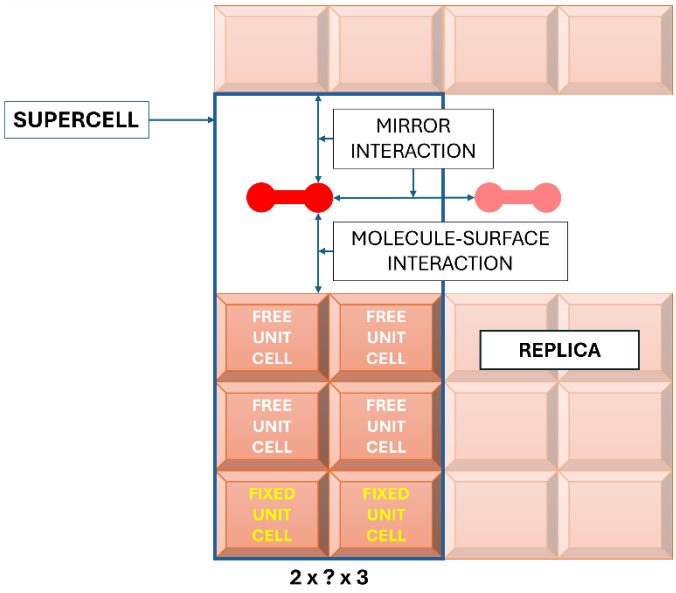



***Figure 5.a.4:*** *graphical representation of a generic supercell obtained replicating m=2 and o=3 times the original crystal unit cell. Value for n is not deducible because of the perspective. Translucid components-unit cells and molecule-represent a not-exhaustive subset of replicas along x and z dimensions.*

| | #vertical layers | #fixed layers | Vacuum | Supercell size |
|---|---|---|---|---|
| Tian et al (2013)[11] | 4 | 2 | NA | 3 x 4 |
| Mino et al (2014)[12] | 6 | NA | NA | 2 x 2* |
| Huygh et al (2016)[13] | 4 | 1 | 16 | 2 x 2 |
| Lopez et al (2016)[14] | 5 | NA | 14 | 2 x 2 |

| | | | | |
|---|---|---|---|---|
| Varilla et al (2019)[15] | 5 | 1 | 14 | 2 x 2 |
| Harb et al (2019)[16] | 7 | NA | 16 | 2 x 2 |

*Table 5.a.2: number of total layers, numbers of fixed layers and top vacuum used to simulate (001) anatase in relevant published papers. NA: Not Available, when the number of layers is sufficiently high, fixed layers may be absent (and the slab present two exposed surfaces). Vacuum size is reported in Å. Asterisk next to the supercell size indicates that the value was not reported but guessed from presented figures.*

It must also be considered that the required number of layers, both fixed and total, depends on the surface under study, as the orientation of the unit cell could lead to different vertical distances. Another potentially relevant factor is the surface energy of the exposed facet; unstable and probably more reactive surfaces—in the case study of this thesis, anatase (001) compared to (101)—might require a larger number of layers to provide an accurate representation of reality. Furthermore, if the simulation objective is the calculation of surface energy, a high number of vertical layers is necessary to allow the system to relax into its lowest-energy geometry, thereby enabling a more accurate calculation. However, since this factor must also be integrated with the analysis of the number of K-points used, it will be discussed in detail in the following chapter. Once again, it must be emphasized that a trade-off is required since the computational cost depends on the number of atoms, but also, given the latter consideration, on the number of K-points.

In defining these parameters—number of fixed layers, number of free layers, and vacuum gap—convergence tests could be useful, like what has already been described regarding the calculation of the cut-off energy and the number of K-points for the unit cell. To the best of our knowledge, there is no evidence that this has ever been taken into consideration. However, since results from different authors, particularly in relation to surface energy, converge on many aspects, it is expected that in practice this is not strictly necessary for the titania case study. In the case of novel surfaces that have not been adequately investigated, such tests could prove particularly relevant.

What instead is of particular interest, as previously stated, is the lateral dimensions of the supercell. These are usually chosen to avoid spurious mirror interactions between replicas and can only assume values that are integer multiples of the cell parameters *(a, b)*. The new parameters will be defined as $a' = m*a$ and $b' = n*b$, where $m$ and $n$ are integers. Generally, it is preferred to omit the values of $a$ and $b$ since, for a given surface, they act as constants. Therefore, the horizontally relevant dimension is given by the product $m \times n$. The novel aspect emerged in the case study concerning the anatase (001) surface, where significant differences are observed if a larger supercell than the one used by

several authors is preferred. In the following dissertation, some adsorption geometries for carbon dioxide over (001) anatase will be presented, acting as a relevant case study. Further details are reported in Section 5.c, which is specifically focused on $CO_2$ adsorption by $TiO_2$.

In Figure 5.a.5, two anatase (001) surfaces characterized by different lateral dimensions are reported for comparison. To obtain an optimized surface independent of the symmetry present in the perfect unit cell, some exposed atoms were shifted in a random direction for about 0.1 Å. Inevitably, the atoms selected for this purpose are the non-fixed ones, as they are susceptible to the movement introduced by the subsequent relaxation. The feasibility of this operation is guaranteed by the fact that, if the introduced artifice is not physically valid, the relaxation will restore the original position.

Comparing different published works, it emerges that the constructed surface often has a = b = 2, whereas the c dimension is considerably variable. A supercell with these characteristics is reported in Figure 5.a.6, where c = 3 and only the lowermost layer of titanium atoms is kept fixed. As graphically illustrated, it can be noticed that the oxygen atoms with the highest vertical coordinate, and thus the most exposed, tend to slightly vary their relative position with respect to the adjacent titanium atoms. This shift does not represent a novel result, as it was previously observed by several authors, as reported for instance by Lazzeri et al. (2001)[17]. Although not explicitly stated, in the figure they present, the supercell under analysis appears to be characterized by a = b = 2 and c = 6. In the reference, it is reported that the two O–Ti bonds in question have strongly non-equivalent lengths, reaching 2.20 and 1.76 Å. The bond lengths for Ti–O bonds in a bulk crystal are 1.94 Å. In the surface depicted in Figure 5.a.6, the exact same distances are obtained. This phenomenon is often overlooked, but it could be directly linked to the reactivity of the anatase (001) surface. Consistently, the relaxation of other less reactive surfaces, such as the (101) and (100) facets reported in the same work, show smaller differences compared to the bulk crystal geometry.

For comparison, Figure 5.a.5 displays an optimized anatase (001) surface where a = b = c = 3, again keeping only one layer of titanium atoms fixed. Inevitably, the attention is focused on the same bonds, which in this case are characterized by distances even more divergent from those found in the bulk crystal, namely 2.23 Å and 1.74 Å. Between the two cases, the one most representative of reality is that with larger dimensions, as it is without any doubts closer to a real surface. It must be noticed that the 2x2 system calculated with a total of 4 k-points shows bond lengths comparable to the one measured on the 3x3 surface.

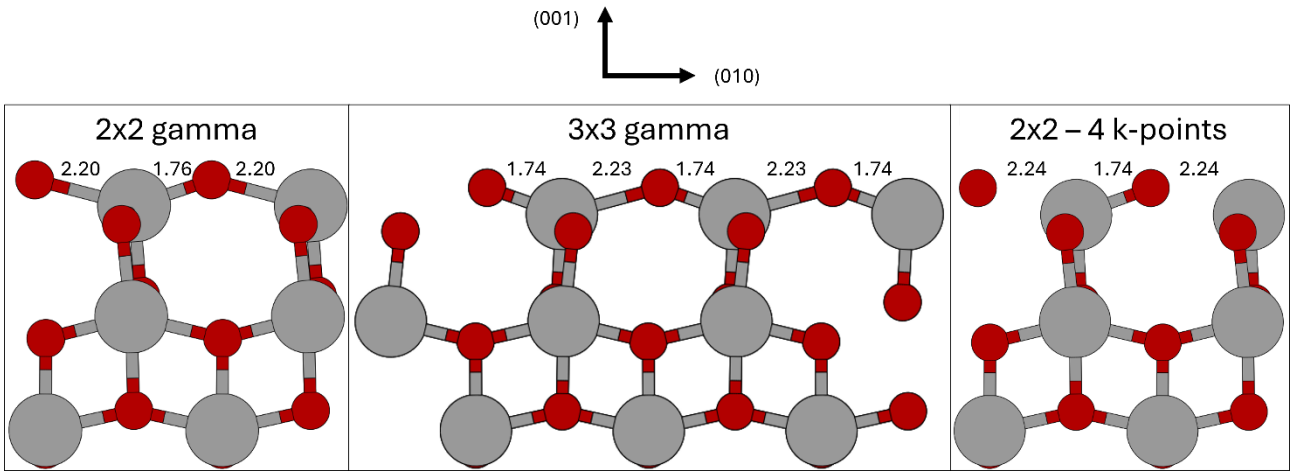



***Figure 5.a.5:*** *optimized (001) anatase slabs calculated with different input parameters.*

It should be noted that the direction exhibiting the greatest asymmetry is along the axis labelled as (010) in Figure 5.a.6. Depending on how specifically the geometry is oriented, it is not incorrect to state that it is instead connected to the (100) axis, which is orthogonal to (010). This does not formally represent an error if an adequate reference system is established. It follows that, assuming the (010) axis—as reported in Figure 5.a.6—is the one described by the y dimension, it would be sufficient to evaluate how the variation of b modifies the surface properties. Although this has been tested, it is still preferred to maintain a = b; therefore, the comparison will be between 2x2 and 3x3 surfaces. With the objective of speeding up calculation, a 2x3 surface could represent an excellent opportunity given the limited number of atoms. However, this has not been adequately investigated yet, as it is more conservative enlarging both the supercell parameters.

The simulations performed on the surfaces under analysis used the Γ-point to sample the Brillouin zone. The 2x2 may suffer from this choice because of the reduced horizontal dimensions; thus, the same calculations were replicated with a uniform 2x2x1 grid to confirm the robustness of the simulation with respect to the Γ-point sampling. The results of this improved calculation will be presented together with the main ones, although not commented upon further as substantially coherent with 2x2_ Γ-point.

In addition to the optimized surface, a valid comparison between the two cases under observation could involve evaluating potential adsorption events. Inevitably, given the overall scope of this thesis, attention is focused on $CO_2$ adsorption. The study of $CO_2$ adsorption on anatase (001) using a 3x3 surface will be properly presented later in this thesis. Although some details will be omitted in this

chapter, an overview of the current state of knowledge regarding $CO_2$ adsorption on anatase (001) can be found in the work by Mino et al (2014)[12].

The first simulation carried out involved, for both the 2x2 and 3x3 surfaces, positioning the molecule in the vacuum gap without enforcing any specific geometry, such as a carbonate species. The systems obtained following the geometry optimization are depicted in Figure 5.a.6. From the visualization, it can be observed that the previously described asymmetry is intensified. It must be emphasized that the chemical bonds displayed in the Figure are artificially introduced by the visualization software and might not be representative of the actual electron density. These bonds are inferred based on the distance between the nuclei of the participating atoms. Consequently, even in Figure 5.a.6 shown previously, it cannot be assumed that a bond is still present if the internuclear distance is increased.

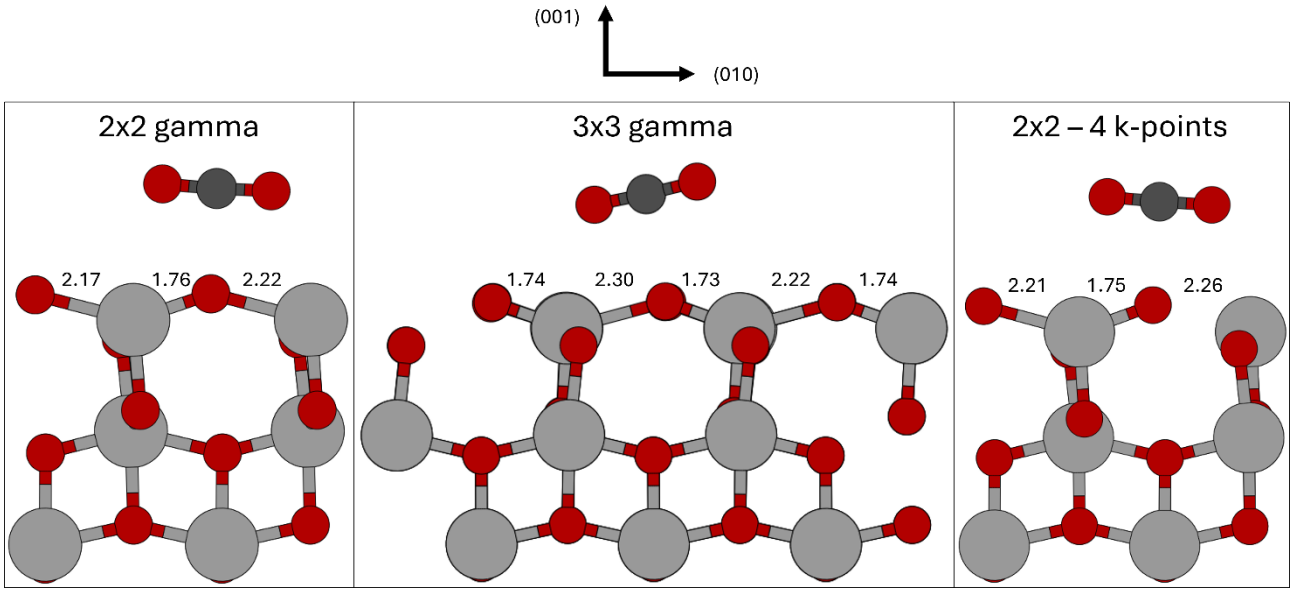



***Figure 5.a.6:*** *carbon dioxide linearly adsorbed on (001) anatase slabs calculated with different input parameters.* $E_{ads_2x2_gamma}$ *= -15 kJ/mol,* $E_{ads_3x3_gamma}$ *= -13 kJ/mol,* $E_{ads_2x2_4_k\text{-}points}$ *= -14 kJ/mol.*

Although obscured by the perspective of Figure 5.a.6, the $CO_2$ molecule lies parallel to the (100) plane, close to one or two surface Ti–O bonds. A strong predominance of local minima is noted, featuring the $CO_2$ molecule in slightly varying positions but keeping the described orientation. In the case scenario reported in Figure 5.a.6, the two Ti–O bonds close to the $CO_2$ molecule take values of 1.76 and 2.22, and 1.73 and 2.30 Å for the 2x2 and 3x3 surfaces. Consequently, for the 3x3 system, a weaker interaction is expected between the two atoms involved in the elongated bond, if present. The calculated adsorption energies for all systems are-15 and-13 kJ/mol and for the 2x2 and the 3x3 (001) anatase slabs respectively, revealing negligible variations.

This displacement is therefore more intense for the larger surface and is realistically a consequence of the possibility given to the atoms to shift horizontally along the (010) axis due to the increased dimensions. This condition suggests that the 3x3 surface has a greater capability to form stable bonds with potential adsorbed species, as its surface geometry is partially disrupted and presumably unstable.

For this reason, starting from the $CO_2$/(001) anatase system, a second molecule was added into the vacuum gap. The position of the second molecule was chosen randomly, with the sole constraint that it does not directly interfere with the first one. Any potential interaction, if possible, can still occur following the structural relaxation, and specific constraints to avoid this situation do not need to be enforced. If the available lateral space is limited, it might be convenient to exploit the vertical dimension, while obviously verifying that this does not cause any spurious adsorption on the surface replica along the z-axis.

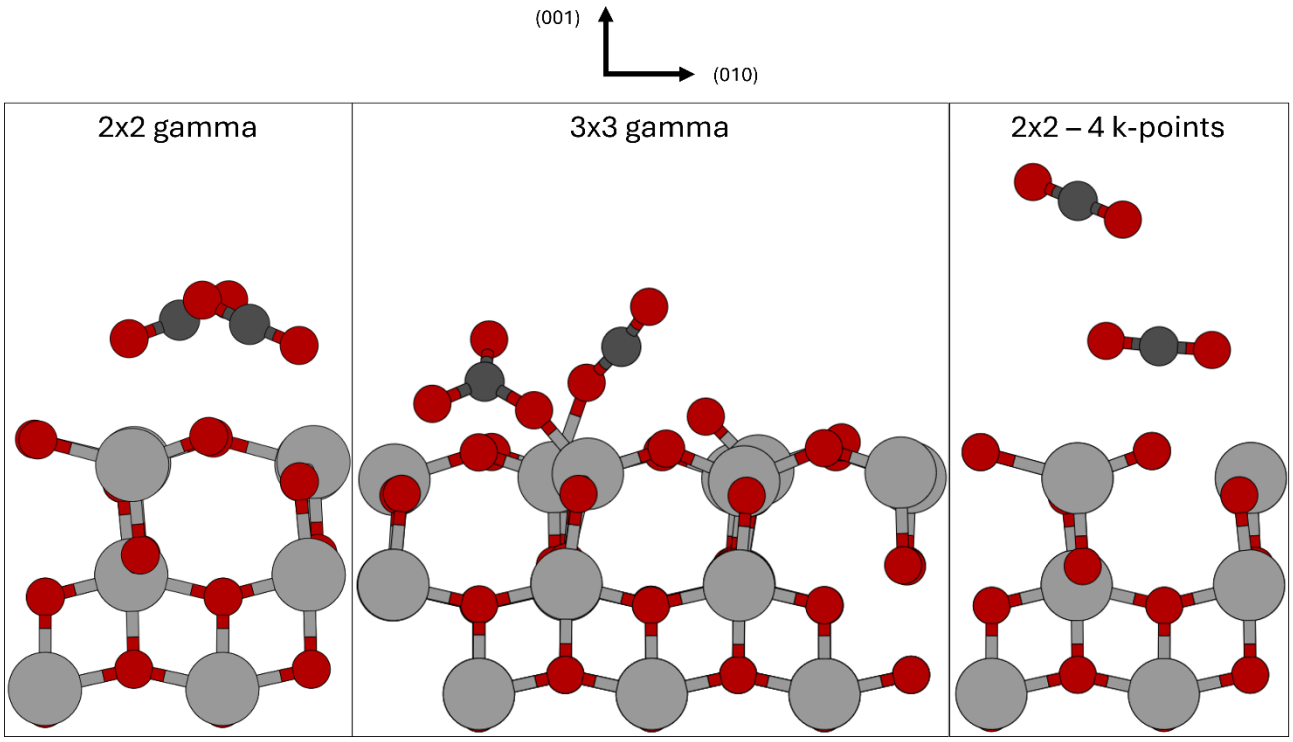



***Figure 5.a.7:*** *two molecule of carbon dioxide adsorbed on (001) anatase slabs calculated with different input parameters.* $E_{ads_2x2_gamma}$ *= -29 kJ/mol,* $E_{ads_3x3_gamma}$ *= -164 kJ/mol,* $E_{ads_2x2_4_k\text{-}points}$ *= -17 kJ/mol.*

Following the optimization of the newly constructed system, important differences are noted between the 2x2 and 3x3 systems, as can be observed in Figure 5.a.7. Indeed, in the first case, it is observed that the system converges to a state where the two molecules are adsorbed with an L-shaped geometry (L=Linear). The surface does not undergo significant variations following the

adsorption of the second molecule. The adsorption energy calculated using the formula is-29 kJ/mol. A diametrically opposite situation occurs if the investigated system corresponds to a 3x3 anatase (001) surface. In fact, the mutual interaction between the molecules and the surface promotes the formation of Bidentate Carbonate (BC) geometry. The adsorption energy in this case is-164 kJ/mol. It should be noted that the initial relative position of the two $CO_2$ molecules may affect the result of the optimization. Thus, the formation of two distinct carbonate groups is allowed and represent a more stable configuration.

Analysing the observed data, it is possible to deduce the presence of an energy barrier—the value of which has not been estimated—characterizing the adsorption of a single $CO_2$ molecule. This is a consequence of the fact that, by definition, geometry optimization can, except for rare cases, only lower the total energy of the system. Therefore, the situation where a single $CO_2$ molecule is adsorbed in an L-shaped geometry represents a local minimum. Considering the previously discussed fact that the relative position between the molecule and the most exposed surface atoms could be variable, the existence of several local minima with comparable energies is hypothesized. This phenomenon—the presence of local minima when a low interaction between the molecule and the surfaces is occurring—has already been widely verified by other authors and is not unique to anatase (001).

Following the introduction of the second molecule, however, the presence of energy barriers is identified solely in the 2x2 system, since the carbonate groups generating in the 3x3 surface. Once again, it is reiterated that estimating the value of these barriers is beyond the scope of this thesis, also considering that it would require different types of calculations and is likely a temperature-dependent phenomenon as well.

The purpose of this discussion is therefore to demonstrate how, from a computational perspective, different results can be obtained following the variation of the supercell lateral dimensions, a parameter that is normally not sufficiently investigated except regarding avoiding mirror interactions between replicas. What has been observed is presumably a consequence of the fact that a larger cell allows for greater degrees of freedom within the system; in this case study, this is provided by a different arrangement of the surface atoms along the (010) direction.

As a corollary to these data, it is worth mentioning that this phenomenon can also affect the adsorption energy for certain types of adsorption geometries. A relevant case is reported in Figure 5.a.8 and Table 5.a.3 regarding the BB geometry. Indeed, it has been noted that the 2x2 and 3x3 systems do not yield concordant results between each other. In the 2x2 system, the BB-2 geometry

proves to be more stable than BB-1, whereas the opposite occurs in the case of the 3x3 system. Although it is impossible to make a direct comparison between adsorption energies calculated using different functionals, the relative stability should nevertheless be preserved. In the literature, several authors have preferred to conduct computational analyses on the anatase (001) surface using 2x2 systems, as reported in Table 5.a.2. Among them, in the only known case to the best of our knowledge where the calculations also concerned bicarbonates, it was verified—likely inaccurately considering the previous evaluations—that BB-2 was more stable than BB-1.

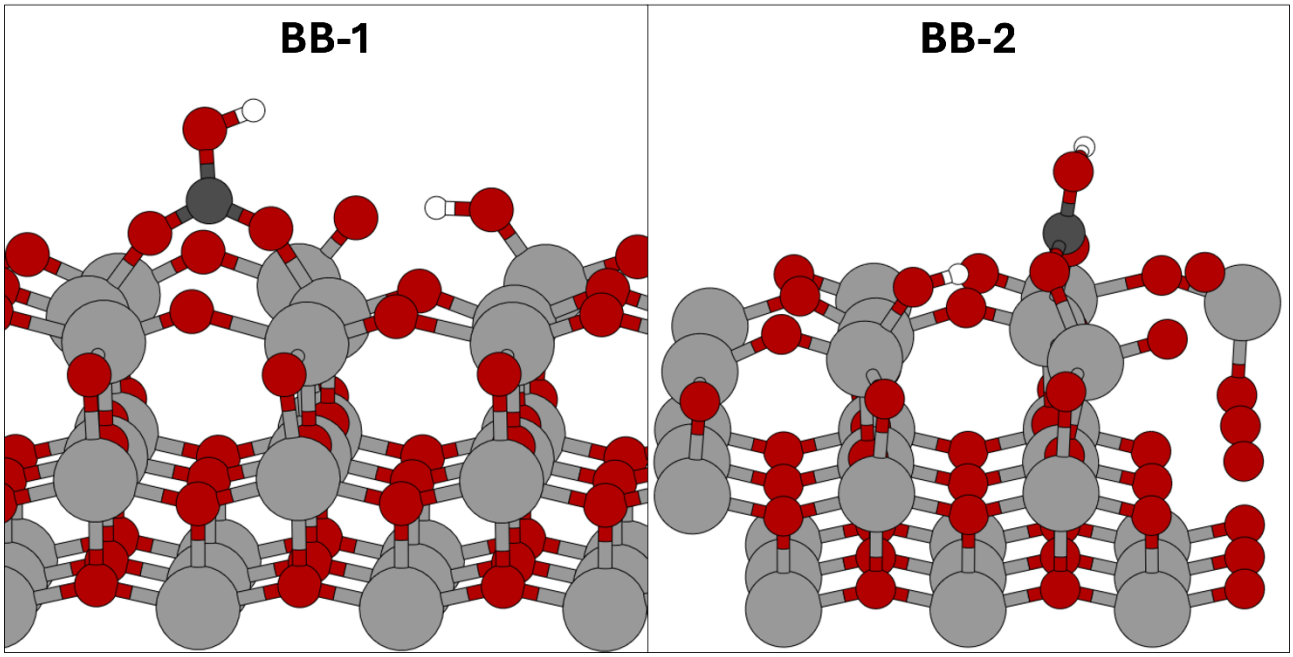



***Figure 5.a.8:*** *Bidentate bicarbonate configurations (BB-1 and BB-2) adsorbed on a 3×3 anatase (001) surface. The bicarbonate group is oriented orthogonally to the (010) direction in BB-1, and nearly orthogonally to the (100) direction in BB-2. While BB-2 does not represent the global minimum for this configuration type, it corresponds to the structure closest to the literature reference. The most stable configuration will be discussed in detail in the dedicated chapter of this thesis.*

| | Mino et al (2014), 2x2x6 | 2x2x3 gamma | 2x2x4 gamma | 3x3x3 gamma |
|---|---|---|---|---|
| $E_{ads}$ BB-1 | -43.1 | -69.2 | -45.7 | -99.9 |
| $E_{ads}$ BB-2 | -61.1 | -64.8 | -67.5 | -40.8 |

***Table 5.a.3:*** *Adsorption energies (kJ/mol) for BB-1 and BB-2 geometries inspired by Mino et al. (2014). Although full convergence to the exact reported minimum was not always achieved—primarily due to the relative orientation of $H^+/OH^-$ with respect to the bicarbonate—the trend confirming that BB-1 is*

*not the most stable configuration on 2x2 surfaces remains valid. In the case of 2x2x3 gamma, the energy difference between the two geometries is remarkably small.*

Another issue that could emerge from this analysis relates to the study of different coverages carried out by merely decreasing the surface size rather than introducing more molecules into the system. In this case, given the possible inability to achieve a correct rearrangement of the surface atoms due to the smaller dimensions of the supercell, the results could be skewed. It is therefore suggested, after performing proper convergence tests on the supercell dimensions, to increase the number of molecules present in the system whenever the goal is to evaluate co-adsorption or the effect of different coverages—phenomena that are, in any case, strictly correlated.

The issues introduced in this chapter of the thesis can be overcome through calculations that are, ultimately, more expensive in terms of computational time as well as required memory. However, this cannot be a limiting factor for the accuracy of the results, especially when the presented works lack adequate experimental evidence. In the presented case study, the same calculations were also performed for a 4x4 surface, with an equal number of vertical layers (3, 1 fixed), and the results are comparable to those obtained for the 3x3 system. As will be subsequently presented within this thesis, several experimental proofs support the soundness of the performed DFT calculations.

Example of input file for optimization

```
&control
    calculation = 'vc-relax',
    restart_mode = 'from_scratch',
    prefix = 'tmp',
    outdir = './tmp/',
    pseudo_dir=' /pseudo_gga/',
    etot_conv_thr = 1.0D-7,
    forc_conv_thr = 1.0D-6,
 /
 &system
    ibrav= 0,
    nat = 12,
    ntyp = 2,
    ecutwfc = 80,
/
 &electrons
    mixing_beta = 0.7
    conv_thr = 1.0D-9
 /
 &IONS
 /
 &CELL
 /
CELL_PARAMETERS angstrom
      3.7710000000       0.0000000000       0.0000000000
      0.0000000000       3.7710000000       0.0000000000
      0.0000000000       0.0000000000       9.4300000000
ATOMIC_SPECIES
  Ti   47.86700   Ti.upf
   O   15.99900   O.upf
ATOMIC_POSITIONS crystal
O           0.0000000000       0.2500000000       0.1656000000
O           0.0000000000       0.7500000000       0.4156000000
O           0.5000000000       0.7500000000       0.6656000000
O           0.5000000000       0.2500000000       0.9156000000
O           0.0000000000       0.7500000000       0.8344000000
O           0.5000000000       0.7500000000       0.0844000000
O           0.5000000000       0.2500000000       0.3344000000
O           0.0000000000       0.2500000000       0.5844000000
Ti          0.0000000000       0.2500000000       0.3750000000
Ti          0.0000000000       0.7500000000       0.6250000000
Ti          0.5000000000       0.7500000000       0.8750000000
Ti          0.5000000000       0.2500000000       0.1250000000
K_POINTS (automatic)
4 4 2 0 0 0
```

# References


[1] M. Napoli and A. Maris, 'Density Functional Theory Simulations of Skaergaardite (CuPd) with a Self-Consistent Hubbard U-Correction', *Chemistry 2025, Vol. 7, Page 56*, vol. 7, no. 2, p. 56, Apr. 2025, doi: 10.3390/CHEMISTRY7020056.

[2] P. Giannozzi *et al.*, 'Quantum ESPRESSO toward the exascale', *Journal of Chemical Physics*, vol. 152, no. 15, Apr. 2020, doi: 10.1063/5.0005082/1058748.

[3] 'pw.x: input description'. Accessed: Jun. 11, 2026. [Online]. Available: https://www.quantum-espresso.org/Doc/INPUT_PW.html

[4] P. Giannozzi *et al.*, 'Advanced capabilities for materials modelling with Quantum ESPRESSO', *Journal of Physics: Condensed Matter*, vol. 29, no. 46, p. 465901, Oct. 2017, doi: 10.1088/1361-648X/AA8F79.

[5] 'Solution LAB1 ecutwfc convergence- Wiki Max'. Accessed: Jun. 11, 2026. [Online]. Available: https://wiki.max-centre.eu/index.php/Solution_LAB1_ecutwfc_convergence

[6] 'Crystallography Open Database'. Accessed: Jun. 11, 2026. [Online]. Available: https://www.crystallography.net/cod/index.php

[7] T. E. Weirich, M. Winterer, S. Seifried, H. Hahn, and H. Fuess, 'Rietveld analysis of electron powder diffraction data from nanocrystalline anatase, TiO2', *Ultramicroscopy*, vol. 81, no. 3–4, pp. 263–270, Apr. 2000, doi: 10.1016/S0304-3991(99)00189-8.

[8] T. Björkman, 'CIF2Cell: Generating geometries for electronic structure programs', *Comput. Phys. Commun.*, vol. 182, no. 5, pp. 1183–1186, May 2011, doi: 10.1016/J.CPC.2011.01.013.

[9] A. R. Aidid, M. K. H. Shishir, M. A. Rahaman, M. T. Islam, M. Mukta, and M. A. Alam, 'Powder X-ray line diffraction pattern profiling of anatase-quartz binary oxide: A crystallographic investigation', *Next Materials*, vol. 8, p. 100571, Jul. 2025, doi: 10.1016/J.NXMATE.2025.100571.

[10] O. T. Hofmann, E. Zojer, L. Hörmann, A. Jeindl, and R. J. Maurer, 'First-principles calculations of hybrid inorganic–organic interfaces: from state-of-the-art to best practice', *Physical Chemistry Chemical Physics*, vol. 23, no. 14, pp. 8132–8180, Apr. 2021, doi: 10.1039/D0CP06605B.

[11] F. H. Tian, X. Wang, W. Zhao, L. Zhao, T. Chu, and S. Yu, 'Adsorption of 2-propanol on anatase TiO2 (101) and (001) surfaces: A density functional theory study', *Surf. Sci.*, vol. 616, pp. 76–84, Oct. 2013, doi: 10.1016/J.SUSC.2013.05.005.

[12] L. Mino, G. Spoto, and A. M. Ferrari, 'CO 2 Capture by TiO 2 Anatase Surfaces: A Combined DFT and FTIR Study', 2014, doi: 10.1021/jp507443k.

[13] S. Huygh, A. Bogaerts, and E. C. Neyts, 'How Oxygen Vacancies Activate CO2 Dissociation on TiO2 Anatase (001)', *Journal of Physical Chemistry C*, vol. 120, no. 38, pp. 21659–21669, Sep. 2016, doi: 10.1021/ACS.JPCC.6B07459.

[14] E. Araujo-Lopez, L. A. Varilla, N. Seriani, and J. A. Montoya, 'TiO2 anatase's bulk and (001) surface, structural and electronic properties: A DFT study on the importance of Hubbard and van der Waals contributions', *Surf. Sci.*, vol. 653, pp. 187–196, Nov. 2016, doi: 10.1016/J.SUSC.2016.07.003.

[15] L. A. A. Varilla, N. Seriani, and J. A. Montoya, 'Molecular adsorption and dissociation of CO2 on TiO2 anatase (001) activated by oxygen vacancies', *Journal of Molecular Modeling 2019 25:8*, vol. 25, no. 8, pp. 231-, Jul. 2019, doi: 10.1007/S00894-019-4103-7.

[16] M. Harb, G. Jeantelot, and J.-M. Basset, 'Insights into the Most Suitable TiO 2 Surfaces for Photocatalytic O 2 and H 2 Evolution Reactions from DFT Calculations', 2019, doi: 10.1021/acs.jpcc.9b08145.

[17] M. Lazzeri, A. Vittadini, and A. Selloni, 'Structure and energetics of stoichiometric TiO 2 anatase surfaces', doi: 10.1103/PhysRevB.63.155409.

## 5.b Surface energy of anatase facets and guidelines for its calculation

A central point analyzed within this thesis is how the same material can radically change its behavior depending on the exposed crystalline plane. This is not only a consequence of different atomic relative positions, but also due to rearrangements introduced by the energy minimization. Inevitably, if the condition prior to relaxation is particularly unstable, a significant rearrangement will be more likely, resulting in bonding geometries among the exposed atoms that are very different from the bulk crystal.

The calculation of surface energy is directly possible using total energies calculated via DFT; however, depending on the simulation parameters, the estimated value may include a non-negligible error. For this reason, it is appropriate to highlight which computational parameters have the greatest influence on introducing inaccuracies into the calculation.

Once the surface energy associated with a specific crystal plane has been calculated, it is possible to evaluate whether it is more catalytically active compared to others, but it is also possible to infer the stability of a sample with specific characteristics. Indeed, it cannot be ruled out that in the case of highly energetic surfaces, a conversion toward more stable situations may occur. Furthermore, this type of study is also helpful when using computational techniques to investigate surfaces of materials synthesized without control over the exposed crystal plane. Depending on the case under study, the plane with the lowest associated surface energy could be an excellent starting point for simulating slabs that are representative of the sample being examined.

In the case study of this thesis, anatase, already identified as a crystalline phase of titanium dioxide that attracts considerable interest in the field of catalysis, is known to exhibit different behaviours depending on the exposed cleavage plane. Indeed, some studies focus on the spatial separation of specific facets within the sample, as this would hinder electron recombination[1], [2]. This phenomenon has important implications in photocatalysis, since unrecombined charges allow for interaction with adsorbates and their subsequent conversion. It has been reported that TiO2 samples in which the separation between the (101)/(100) and (001) cleavage planes is present have favoured selective redox reactions. Specifically, the trend is reported to involve electron transfer toward the (101)/(100) facets, with a consequent migration of holes toward the (001) facet. It follows that a preference toward either oxidation or reduction of adsorbed species occurs, respectively.

In general, surface energy can provide indications regarding the reactivity of a cleavage plane; however, it does not guarantee that certain molecular adsorptions will occur. For this reason, a different type of study focusing on adsorption geometries in various contexts may be advisable. In the case study of this thesis, several works report the tendency of anatase cleavage planes with higher surface energy to allow more stable $CO_2$ adsorptions; however, this must be considered a correlation rather than a consequence.

Every surface is characterized by a specific amount of energy associated with its formation. This term is often called surface energy ($E_{surf}$) or formation energy ($E_{form}$), and the two terms are used interchangeably. However, within the scope of this discussion, the former formulation is preferred, as the normalization with respect to the exposed area is explicit, whereas in the latter term, the necessity of including the described normalization is less clear.

The formula for calculating the surface energy is given in Equation 5.b.1. It consists of dividing the difference between the total energy calculated for the slab and the energy of an equivalent number of $TiO_2$ formula units by the exposed surface area. The calculation of the subtracted term is effectively a normalization of the total number of atoms present in the slab with respect to those contained in the bulk unit cell. In practice, this involves multiplying the calculated total energy of the crystal unit cell by the ratio between the total number of atoms in the slab and the number of atoms present in the crystal unit cell (whether primitive or conventional is indifferent when the correct number of atoms is included)

$$E_{surf} = (E_{slab} - E_{bulk_eq}) / exposed_surface_area$$

*Equation 5.b.1*

Although the calculation appears almost trivial, it hides a critical issue that is very often overlooked. This lies in the fact that, in the study of surfaces via plane-wave DFT, it is frequently assumed that the actual surface is identifiable by the atoms with the highest vertical coordinate. The other side of the slab, the one identified by the lowest atoms, is often ignored; at most, the vacuum spacing value is intentionally increased to avoid spurious mirror interactions. In reference to this, a simplified figure is provided in the previous chapter to help better visualize the described phenomenon.

Many authors propose freezing the lower atoms in position so that they maintain the crystal geometry, allowing the upper atoms to simulate the actual surface of a bulk crystal. Consequently, particularly for surfaces with high surface energy, an accurate representation of the movement of the

exposed atoms can only be achieved when the total number of layers free to move is sufficiently high. It is worth noting that, although this represents a useful convention, one can find works that do not include fixed atoms. In these cases, the number of vertical layers must instead be large enough so that the effects of the displacement of the exposed atoms on one side of the slab are negligible on the optimized position of the exposed atoms on the opposite side. In Equation 5.b.1, when referring to the dimensions of the exposed surface it is mandatory to consider that the slab possesses two surfaces.

Effects due to the inaccuracy introduced by fixed atoms are less evident when the study focuses on adsorption energies. Indeed, it can be reasonably assumed that the formula used, requiring the subtraction between the total energies of two systems containing the slab, reduces or cancels the error contribution.

Anatase investigated in this thesis has represented an interesting case study, given the extensive knowledge regarding the properties of its exposed facets. Moreover, a partial knowledge about how certain computational parameters, primarily the functionals used, can alter formation energies and the geometries of bonds involving the exposed atoms.

A pivotal work reporting the surface energy values for the most well-known cleavage planes of anatase is that by Lazzeri, Vittadini, and Selloni (2002). The values listed in Table 5.b.1 are those corrected and reported in its associated Erratum (it is worth noting that the Erratum did not introduce significant modifications to the original work).

In the comparison between different surfaces of rutile and anatase, the comparison between calculations conducted using different functionals, LDA and PBE (the latter belonging to the GGA category), is significant. Indeed, it is noted that there is no coincidence between the two sets of calculations, with LDA being theoretically less accurate but still appearing to demonstrate correct relationships between the reactivities of different surfaces. Therefore, very cautiously, it could be stated that the lighter LDA functionals remain valid for this purpose, though their results obviously cannot be analysed together with GGA ones.

The proposed work includes an attempt to analyze the energy of unrelaxed systems, a potential future development of the current chapter that is not without critical issues. However, a direct reference to values from the work by Lazzeri et al. will be provided below.

| Surface | (101) anatase | (001) anatase |
|---|---|---|
| $E_{surf}$ Lazzeri et al (2002)[3] | 0.44<br>1.28 ➔ 0.49 | 0.90<br>1.12 ➔ 0.98 |
| Esurf other works[4] | [0.37, 0.69] | [0.90, 1.08] |

***Table 5.b.1:*** *surface energies ($E_{surf}$, in J/m²) for specific anatase facets, as calculated by Lazzeri et al. (Erratum, 2002) and other literature references. Underlined values highlight the transition from unrelaxed to relaxed surfaces based on uncorrected $E_{surf}$ data.*

Regarding the supercell dimensions discussed in the previous chapter, the influence of these parameters on the surface energy calculation was investigated. Already in the work by Lazzeri et al., it was mentioned that the number of vertical layers could affect the geometries of surface atoms and, consequently, the surface energy. However, this appeared to be disproven by their following simulations conducted on the same surface with a variable number of layers show comparable surface energies. Nevertheless, due to the slight inaccuracy reported in the Erratum, a new work addressing this topic has been identified.

The paper in question is that by Martsinovich and Troisi (2012), which reports a specific study on surface energies with respect to the number of vertical layers for various anatase surfaces[4]. Figure 1 of the mentioned work reveals that, for many cleavage planes, the number of layers does not significantly affect the surface energy calculation; however, a few important points should be noted. First, for the (100) surface, the upper extreme resulting from a single layer is clearly an outlier compared to the values obtained with a higher number of layers. Therefore, this underscores the necessity of a reasonable number of vertical layers, even though this critical case is the only one reported in the paper. Second, an increase in the number of layers does not coincide with a systematic increase or decrease in surface energy. As shown in the comparison between the (001) and (110) surfaces in the same figure, this fluctuation could lead to conflicting data that depend on the slab thickness. Nevertheless, excluding the reported single-layer case, the calculation results appear sufficiently robust to allow a general estimation of the stability of the investigated surface.

Having therefore already established a thorough study on the vertical dimension, the horizontal dimension is also taken into consideration, following the same approach used in the previous chapter for analyzing other properties of the anatase (001) surface. In this case, the comparison will be between two scenarios widely evaluated in the literature, namely the (101) and (001) anatase surfaces. This is because, as shown in Table 5.b.1, they represent two very distinct conditions in terms

of surface energy and, consequently, predicted stability. Furthermore, as related information, it is noted that the (001) surface generally allows for more stable molecular adsorptions. In relation to the analysis presented in the following chapters, this surface is also capable of distorting bonds (such as the formation of carbonate from $CO_2$) or breaking molecules (such as water splitting on anatase (001)).

## (001) anatase

To determine the influence of computational parameters on the formation energy of the anatase (001) surface, several tests were conducted by varying the horizontal dimensions of the supercell. A representative set of these tests is reported in Table 5.b.2. However, considering solely the spatial extension data is not sufficient on its own, as it must be recalled that the sampling of the first Brillouin zone in the reciprocal space varies inversely with the spatial dimensions of the supercell. For this reason, different k-point grids were used. When the Γ-point was not employed, at most one vertical sampling point is present, since the oversized z-coordinate dimension of the supercell was never modified.

To verify the accuracy of the calculations, it is necessary to identify a reference value considered correct beyond any doubt (a gold standard). This proves difficult when literature results are significantly variable, as shown in Table 5.b.1. For this reason, it was preferred to define an internal standard obtained based on considerations of the computational parameters and their role in the surface energy calculation. The standard regarding the anatase (001) surface is the one designated as #1 in Table 5.b.2, the reason for its choice will become clear at the end of the discussion.

| (001) anatase | | | | | |
|---|---|---|---|---|---|
| Id calc | X x Y (horizontal) | Z (vertical) | Z fixed | k-points | $E_{surf}$ ($J/m^2$) |
| #1 | 2x2 (reference) | 5 | 0 | 2x2x1 | 0.94 |
| #2 | 1x1 | 3 | 1 | 2x2x1 | <u>0.80</u> |
| #3 | 1x1 | 3 | 1 | 3x3x1 | 0.98 |
| #4 | 1x1 | 4 | 1 | 2x2x1 | <u>0.75</u> |
| #5 | 1x1 | 4 | 1 | 3x3x1 | 0.97 |
| #6 | 2x2 | 3 | 1 | Gamma | <u>0.80</u> |
| #7 | 2x2 | 3 | 1 | 2x2x1 | 0.99 |
| #8 | 2x2 | 4 | 1 | Gamma | <u>0.75</u> |
| #9 | 2x2 | 4 | 1 | 2x2x1 | 1.00 |
| #10 | 3x3 | 3 | 1 | Gamma | 0.98 |
| #11 | 3x3 | 4 | 1 | Gamma | 0.99 |
| #12 | 3x3 | 5 | 1 | Gamma | 0.97 |
| #13 | 3x3 | 4 | 2 | Gamma | 1.00 |
| #14 | 3x3 | 5 | 2 | Gamma | 0.97 |

***Table 5.b.2:*** *$E_{surf}$ of (001) anatase calculated employing different computational parameters. Outlier values are underlined.*

As shown in the table, and consistently with the literature, the number of vertical layers does not appear to impact the calculated surface energy. Examples of this can be observed, for instance, when transitioning from calculations #2 and #3 to #4 and #5, respectively, where one vertical layer was added. Similarly, all calculations from #10 to #14, in which the number of vertical layers varies from 3 to 5 (with 1 or 2 fixed layers), yield very similar surface energy values, which are well in line with literature data. The range for the number of vertical layers was selected based on those proposed by numerous authors, who nevertheless might not have included the surface energy calculation among the results of their work. Clearly, the effort by Zhao et al. (2010) in using 16 layers is deemed excessively disproportionate and is not recommended, as it represents an unnecessary waste of computational time if the objective is limited solely to calculating the surface energy[5].

It is also necessary to consider how relaxation affects the position of surface atoms, as significant displacement requirements combined with the presence of fixed layers could severely restrict atomic movement. Although no evidence of this effect was found for the (001) surface, Lazzeri et al. did

attempt to evaluate the unrelaxed surface[3]. Even though the unrelaxed energy values were not corrected in the Erratum, thus they are likely slightly inaccurate in the main text due to the functional-related issues they reported, they can still be included in this discussion. Specifically, the interest lies in comparing the $E_{surf_unrelaxed}$ values of anatase (001) and (101), estimated at 1.12 and 1.28 J/m$^2$, with their corresponding $E_{surf_relaxed}$ values of 0.98 and 0.49 J/m$^2$. It is evident that the surface energy of the (101) facet changes much more significantly upon relaxation compared to the (001) surface. Therefore, it is reasonable to assume that atomic displacement is more pronounced in the case of the anatase (101) surface.

Table 5.b.2 clearly shows that the critical issues in the surface energy calculation are mostly dependent on the horizontal dimensions. However, unlike what was specifically described for other behaviours of the anatase (001) surface, the role of k-points is highly relevant for the calculation of $E_{surf}$ Indeed, through simple multiplications, it becomes immediately clear that in the case study under consideration, when #Lα * kα < 3, where #Lα represents the number of layers along a generic dimension (x or y) and kα is the number of k-points for the chosen direction, the surface energy values deviate significantly from both analogous tests conducted within the present work and confirmed literature data.

Based on these findings, it is recommended to use the maximum allowed value of #Lα * kα, within the limits of computational capabilities. Following this criterion, the reference system was identified: an anatase (001) surface with a 2x2 horizontal supercell and a 2x2x1 k-point grid. The resulting product, equal to 4, is well above the determined lower limit. Regarding the choice of 5 vertical layers, this stems from the previously discussed rationale concerning fixed layers; while these layers effectively constitute the lower surface, their electron density is not accurately represented due to an inadequate atomic arrangement. The choice for the reference is therefore to employ a sufficiently thick slab with no constrained atoms. The selected number of layers was deemed reasonable based on the results obtained from simulations #12 and #14, and it is consistent with values used by other authors, which typically do not exceed 6 layers when the simulation excludes fixed atoms.

## (101) anatase

The study of the surface energy of the (101) anatase surface proved to be comparably much more complex. In wishing to leverage some of the considerations made for the (001) surface, one must account for the horizontal dimensions of the single $TiO_2$ unit (3 atoms) constituting a (001) surface prior to optimization (3.80 x 3.80 Å). Consequently, when normalizing the required number of k-points with respect to length, the resulting product must be greater than 3.80 x 3 = 11.40, keeping in mind that the '3' derives from the considerations regarding the number of k-points for the (001) surface.

Following the identification of the new axes required for generating the (101) surface, a step that was unnecessary for the (001) surface, it is convenient to define the repeating unit as $Ti_2O_4$, thus consisting of 6 atoms. Its horizontal dimensions are 5.53 x 3.57 Å, and the created model surface is a 2x2x3 replica of this unit, naturally including vertical vacuum spacing to avoid mirror interactions. This results in the necessity of constructing a k-point grid of at least 1x2x1; although a denser grid could yield more accurate results, it would be computationally expensive.

Table 5.b.3 lists the tested cases of anatase (101) surfaces and their corresponding calculated $E_{surf}$. It is clearly observed that the presence of fixed layers, in this case, contributes to the calculated result. This is in line with expectations, given the prior considerations regarding unrelaxed surfaces. In this instance, despite the limited number of vertical layers, a value consistent with the literature (cf. Table 5.b.1) is achieved only when fixed layers are excluded.

| (101) anatase | | | | | |
|---|---|---|---|---|---|
| Id calc | X x Y (horizontal) | Z (vertical) | Z fixed | k-points | $E_{surf}$ ($J/m^2$) |
| *1 | 2x2 | 3 | 0 | 1x2x1 | 0.44 |
| *2 | 2x2 | 3 | 1 | Gamma | <u>0.72</u> |
| *3 | 2x2 | 3 | 1 | 1x2x1 | <u>0.84</u> |

**Table 5.b.3:** $E_{surf}$ of (101) anatase calculated employing different computational parameters. Outlier values are underlined.

Although the performed work involved only two surfaces, some cautious conclusions can be drawn. First, it is confirmed that the total number of vertical layers is not particularly relevant to the surface energy calculation. This result had already been highlighted by several works in the literature, but for the sake of thoroughness, an independent confirmation was preferred. Although not tested within the scope of the presented work, it is worth recalling the dependence on the functional used, along

with the preference to include the electron density gradient to achieve more accurate results. When this is not included, the results can still be considered valid, despite the lack of a possibility for a direct comparison between results calculated at different levels of approximation. Finally, the horizontal dimension of the surface appears to influence the $E_{surf}$ calculation when the k-points are not adequately considered.

The novel element introduced by this thesis chapter concerns how the presence of fixed layers can influence the surface energy calculation. As described, this factor does not appear to be relevant for the anatase (001) surface but becomes crucial for the anatase (101) facet. A tentative explanation for this phenomenon could lie in the energy difference between the unoptimized and optimized surfaces. Although obtaining an accurate total energy value for the unoptimized case is highly critical, since it is far from a ground-state condition where the fundamental theorems of DFT guarantee the reliability of the result, a direct correlation was highlighted among $\Delta E_{surf_unrelaxed\text{-}relaxed}$, the number of fixed vertical layers, and the calculated $E_{surf_relaxed}$[6].

While the results and considerations proposed in this chapter certainly need to be expanded before drawing definitive conclusions, this discussion is believed to represent a solid starting point for subsequent future developments.

## References

[1] D. Kim *et al.*, 'Dissimilar anisotropy of electron versus hole bulk transport in anatase TiO 2 : Implications for photocatalysis', *Phys. Rev. B*, vol. 95, p. 45209, 2017, doi: 10.1103/PhysRevB.95.045209.

[2] L. Ren, Y. Li, M. Mao, L. Lan, X. Lao, and X. Zhao, 'Significant improvement in photocatalytic activity by forming homojunction between anatase TiO2 nanosheets and anatase TiO2 nanoparticles', *Appl. Surf. Sci.*, vol. 490, pp. 283–292, Oct. 2019, doi: 10.1016/J.APSUSC.2019.05.351.

[3] M. Lazzeri, A. Vittadini, and A. Selloni, 'Structure and energetics of stoichiometric TiO 2 anatase surfaces', doi: 10.1103/PhysRevB.63.155409.

[4] N. Martsinovich and A. Troisi, 'How TiO 2 crystallographic surfaces influence charge injection rates from a chemisorbed dye sensitiserw', *Phys. Chem. Chem. Phys*, vol. 14, pp. 13392–13401, 2012, doi: 10.1039/c2cp42055d.

[5] Z. Zhao, Z. Li, and Z. Zou, 'Surface properties and electronic structure of low-index stoichiometric anatase TiO 2 surfaces', 2010, doi: 10.1088/0953-8984/22/17/175008.

[6] V. Sahni, 'The Hohenberg-Kohn Theorems and Kohn-Sham Density Functional Theory', *Quantal Density Functional Theory*, pp. 99–123, 2004, doi: 10.1007/978-3-662-09624-6_4.

## 5.c Adsorption geometries of $CO_2$ on (001) anatase

To enhance the efficiency and selectivity of the catalyst, elucidating the adsorption geometries of the target molecule, carbon dioxide within the scope of this thesis, on the material surface, titanium dioxide, is of vital importance. Prior literature demonstrates an excellent level of consensus regarding the stable adsorption configurations of $CO_2$, although the results reported in this chapter introduce a correction concerning the stability of one specific geometry. A scheme illustrating these theoretical geometries, inspired by the work of Mino et al. (2014) and often reported in similar works, is presented in Figure 5.c.1[1]. The study is divided into two distinct sections, evaluating the system in the absence and presence of water, respectively.

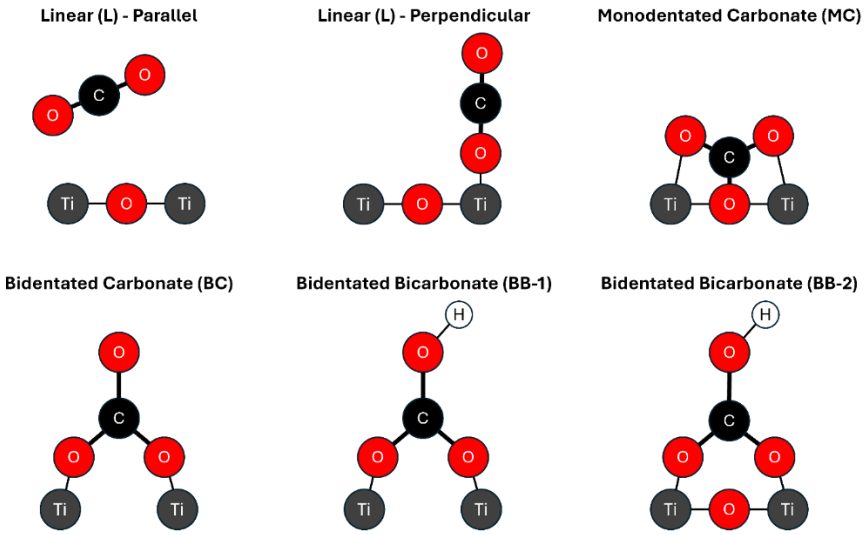



*Figure 5.c.1: A schematic representation of relevant adsorption geometries of $CO_2$ on $TiO_2$ surfaces.*

To simulate anatase with the (001) facet exposed, a supercell including 3x3 units of $TiO_2$ with three vertical layers was constructed. For (101), a supercell consisting of 2x3 units of $Ti_2O_4$ with two vertical layers was used. In both slabs, a vacuum region of approximately 16 Å was included to prevent interactions between periodic images, and the atoms belonging to bottom layers were fixed. The reciprocal space of the supercell was sampled at the Γ-point, while other computational parameters were identical to the one provided in the example reported at the end of Chapter 5a.

## $CO_2$ adsorption on the stoichiometric (001) anatase slab

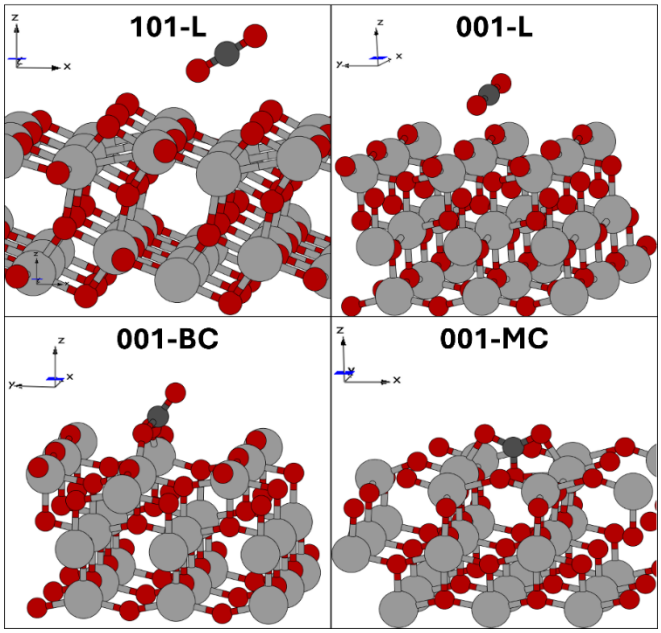



***Figure 5.c.2:*** *Optimized adsorption geometries of $CO_2$ on stoichiometric (001) anatase. Linear adsorption on (101) anatase is reported as a reference.*

| | Gas-phase | L (on 101) | L | BC | MC |
|---|---|---|---|---|---|
| $d$(Ti–$O_m$) (Å) | - | 2.686 | 3.051 | 1.828, 1.862 | 2.036, 2.051 |
| $d$(C–$O_s$) (Å) | - | 3.189 | 2.800 | - | - |
| $d$(C–$O_m$) (Å) | 1.168 | 1.172, 1.163 | 1.171 1.166 | 1.334, 1.352 1.207 | 1.293 1.293, 1.286 |
| $\alpha$(O-C-O) (°) | 180.0 | 177.9 | 177.6 | 112.9, 122.8, 124.3 | 116.9, 115.7 127.4 |
| $\alpha$(Ti-O-C) (°) | - | 146.3 | 115.1 | 146.1, 153.9 | 94.6, 95.9 |
| $E_{ads}$ (kJ/mol) | - | -17.5 | -13.5 | -125.9 | -151.9 |

***Table 5.c.1:*** *geometrical parameters of gas-phase and adsorbed $CO_2$ over (101) and (001) stoichiometric anatase. $d$: distance, $\alpha$: angle, $E_{ads} = E_{slab+molecule} - E_{slab} - E_{molecule}$, $O_m$: oxygen atom which*

*forms a bond with the carbon atom, $O_s$: oxygen atom of the surface not forming a bond with the carbon atom. Underlined values indicate distances between the carbon atom and the upper oxygen atom.*

Different starting configurations were tested to achieve all the different optimized geometries for $CO_2$ adsorbed on anatase: Linear (L), Bidentate Carbonate (BC) and Monodentate Carbonate (MC). Comparing similar works available from literature, some discrepancies in the definition of the BC geometry may be highlighted. This is a consequence of the presence of an additional oxygen atom not justified by the stoichiometry of the system[1], [2]. For this reason, the structure with the correct number of oxygen atoms might be more accurately described as the Bent (B) geometry. Nevertheless, the label BC was chosen to ensure comparability with prior studies, despite this non-negligible difference. Due to the presence of different local minima which can be reached during the optimization, different results may be obtained, as reported in the work of Kovačič et al. for the L geometry on a (001) anatase slab[3]. The optimized systems are shown in Figure 5.c.2, while their corresponding bond lengths and angles are summarized in Table 5.c.1, with the L geometry on the (101) anatase slab serving as a reference as it is the only possible adsorption geometry on this surface.

Revising works from different authors, calculated adsorption energies are found to depend on several factors. Literature values range from-18.3 to-30.6 kJ/mol for L, and from-114.2 to-137.3 kJ/mol for MC, while the only available reference for BC is the value of-87.4 kJ/mol reported by Mino et al[1], [3], [4], [5]. The values computed in this work deviate drastically from these findings, being lower for L and higher for both BC and MC. Theoretically, these discrepancies may be attributed to varying simulation parameters, most notably the choice of pseudopotentials. Specifically, the simulations reported herein were conducted using NC-PBE functionals, whereas prior literature predominantly relies on hybrid functionals. Moreover, the supercell dimension has been shown to affect the calculated adsorption energy. Nevertheless, the stability trend $E_{MC} < E_{BC} < E_L$ remains unaltered, confirming that MC is the most stable and, consequently, the most frequently occurring configuration.

These non-negligible adsorption energies computed for BC and MC confirm the higher reactivity of the (001) plane over the more stable (101) surface, where the adsorption energies of BC and MC are positive, indicating an unfavourable configuration[1]. Comparing structural parameters across the three calculated adsorption geometries, L presents the greatest differences compared to the work of Mino et al[1]. This is most evident in the distance between the carbon atom and the closest oxygen atom of the surface, as our result is 0.844 Å greater than theirs. This discrepancy occurs because

different local minima, associated with varying positions of the molecule over the slab, could be reached during the optimization; this behaviour was extensively explored by Kovačič et al. in their work, which was, however, limited to the L configuration[3]. In the case here reported, the adsorption is characterized by an oxygen from the molecule coordinating toward a titanium atom of the surface, whereas in their case, the molecule lies almost parallel to the surface, with the result that the shortest distance obtained is d(C–Os). Consequently, we obtain a value for $\alpha$(Ti-O-C) that is slightly greater than theirs. The most significant differences in the BC geometry are found in the angles, as the values reported herein are around 10° smaller than those that they obtained. Notably, the shape of the adsorbed molecule is not completely perpendicular to the surface but is significantly tilted toward the y-direction. Finally, MC does not present any significant difference with respect to prior studies, likely because it represents the most stable configuration, which prevents variations associated with alternative local minima.

To conclude this section, it is worth recalling the previously discussed effects of supercell dimension on promoting adsorption, particularly when two $CO_2$ molecules are adsorbed onto the anatase (001) surface. To the best of our knowledge, the phenomenon of spontaneous conversion from the L to the BC configuration has not been documented in the literature and could represent a compelling avenue for future investigation. In any case, the MC geometry remains the most stable adsorption configuration; however, its formation starting from either the L or BC states was not observed during our simulations, thereby suggesting the presence of substantial energy barriers.

## $CO_2$ adsorption on the hydroxylated anatase (001) slab

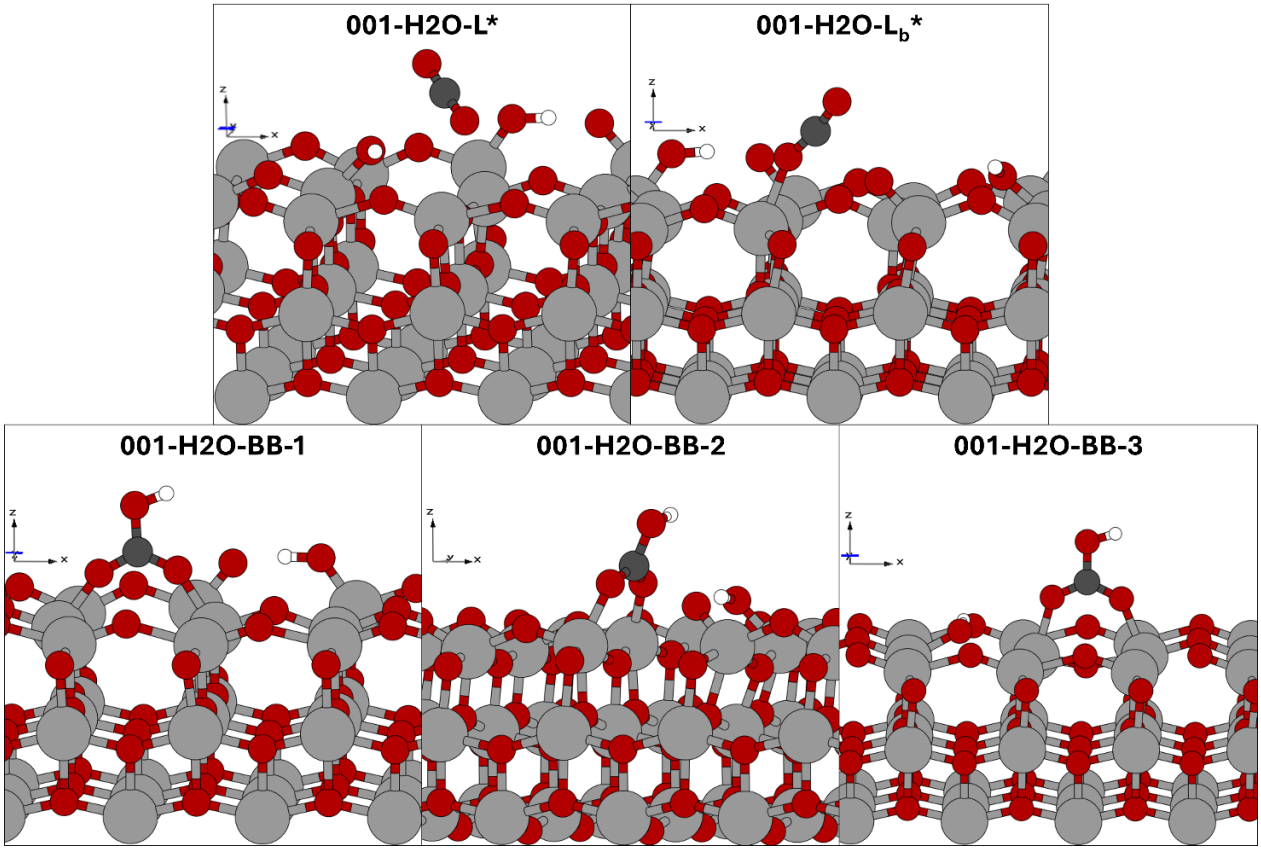



*Figure 5.c.3: Optimized adsorption geometries of $CO_2$ on hydroxylated (001) anatase.*

| | L* | $L_b$* | BB-1 | BB-2 | BB-3 |
|---|---|---|---|---|---|
| $d$(Ti–$O_m$) (Å) | 2.292 | 2.209 | 1.962<br>2.016 | 2.012<br>2.013 | 2.059,<br>2.068 |
| $d$(C–$O_s$) (Å) | 2.705 | 2.400 | - | 3.116 ($d$(C–$O_s$H)) | - |
| $d$(C–$O_m$) (Å) | 1.180,<br>1.155 | 1.183,<br>1.156 | 1.262,<br>1.263,<br>1.338 | 1.249,<br>1.263,<br>1.337 | 1.265,<br>1.277,<br>1.348 |
| $\alpha$($O_m$-C-$O_m$) (°) | 176.0 | 170.0 | 115.0,<br>118.0,<br>127.0 | 115.2,<br>116.5,<br>128.3 | 130.0,<br>115.7,<br>114.3 |
| $\alpha$(Ti-$O_m$-C) (°) | 139.4 | 148.3 | 145.9,<br>154.6 | 136.4,<br>136.7 | 129.0,<br>138.0 |

| | | | | | |
|---|---|---|---|---|---|
| $E_{ads}$ (kJ/mol) | -21.0 | -46.2 | -99.5 | -29.8 | +54.9 |

***Table 5.c.2:*** *adsorption geometries of gas-phase and adsorbed CO2 over (001) hydroxylated anatase.* $d$*: distance,* $\alpha$*: angle,* $E_{ads} = E_{h001+CO2} - E_{h001} - E_{CO2}$*,* $O_m$*: oxygen atom which forms a bond with the carbon atom,* $O_s$*: oxygen atom of the surface not forming a bond with the carbon atom. Underlined values indicate distances between the carbon atom and the upper oxygen atom.*

To accurately describe $CO_2$ adsorption on hydroxylated surfaces, the nomenclature used to describe $CO_2$ adsorption must be updated. This revision accounts for new chemical species arising from the joint interaction of the surface, $CO_2$, and ions from dissociated water $H^+$ or $(OH)^-$. The configurations are classified as Monodentate Bicarbonate (MB) and Bidentate Bicarbonate (BB), with the linear case labelled as L*.

As extensively reported, water tends to dissociate into $H^+$ and $OH^-$ when adsorbed over a (001) anatase surface, as this state is more stable than the molecular adsorption[6]. For this reason, this configuration, labelled as $h_{001}$=hydroxylated (001) anatase, was considered when calculating the adsorption energy as $E_{ads} = E_{h001+CO2} - E_{h001} - E_{CO2}$. Optimized structures over $h_{001}$ are reported in Figure 5.c.3 and Table 5.c.2.

Several local minima were identified for the linear geometry on $h_{001}$, depending on the relative position between the $CO_2$ molecule and the $H^+/OH^-$ ions. The configuration labelled L* corresponds to the molecule adsorbed close to the $H^+$ ion, while $L_b$* represents a configuration where $CO_2$ is located further away from the ions on the slab. The case where the molecule is positioned next to the $OH^-$ ion is not presented, as it no local minima were found corresponding to this condition.

The major modification observed in L* and $L_b$* with respect to the linear geometry in the absence of water is that the molecule is significantly closer to the surface, as the distance $d$(Ti–$O_m$) is 2.291 and 2.209 Å respectively, while for L on (101) and L on (001) from the previous section it was 2.686 and 3.051 Å. Kovačič et al. presented different available geometries over a (001) anatase slab, revealing a condition where the distance was 2.305 Å, which suggests that this parameter does not represent a characteristic factor[3]. More interestingly, the $\alpha$($O_m$-C-$O_m$) angle for $L_b$* is 170.0°, which is significantly lower than in the other linear configurations, suggesting a tendency for the molecule to transition toward a “Bent/BC” geometry. This may be attributed to a long-range interaction (2.803 Å) between the uppermost oxygen atom of the $CO_2$ molecule and a surface oxygen atom located near the carbon atom. Notably, the $d$(C–$O_s$) bond length reported for $L_b$* is the shortest among all

configurations. The adsorption energy of L* and Lb* in the presence of chemisorbed water on (001) anatase is respectively-21.0 and-46.2 kJ/mol, indicating a higher stability compared to L over the stoichiometric surface which presents an adsorption energy of-17.5 kJ/mol. This may suggest that the water presence can promote $CO_2$ adsorption.

Among the various geometries explored by Mino et al. for the configuration of bicarbonates, it can be confidently stated that only the *bridging* BB configuration is energetically favourable[1]. In contrast, the *chelating* BB configuration (referred to as BB4 in their study) exhibits an adsorption energy of-6.3 kJ/mol indicating low stability while all MB configurations present positive adsorption energies and are therefore unfavourable.

Figure 3 of their work shows that the different bridging BB configurations vary based on the angle formed between the bicarbonate group and the direction defined by two adjacent titanium atoms with a bridging oxygen atom located above them. For clarity, let us define configuration BB-1 as the one in which the plane formed by the three oxygen atoms of the $HCO_3^-$ group is parallel to this direction, and configuration BB-2 as the one in which the plane and the direction are orthogonal. BB-3 could be considered a special case of BB-1, although the formed bicarbonate group does not include an oxygen atom from the surface. This behaviour could be schematically represented by the following reactions:

$$\textbf{BB-1: } 001_\text{Anatase} + H_2O + CO_2 \rightarrow (001_\text{Anatase} - O)^{2+} + HCO_3^- + OH^-$$

$$\textbf{BB-2, BB-3: } 001_\text{Anatase} + H_2O + CO_2 \rightarrow 001_\text{Anatase} + HCO_3^- + H^+$$

This simplified description of the atoms involved in the reaction highlights that, in the first case, an $OH^-$ ion remains bound to the surface, whereas in the other case, it is a proton ($H^+$) that is retained. The position of the ion introduced to balance the charge, which is not part of the bicarbonate group, may also play a significant role in determining the system's stability. This is particularly evident for the BB-2 and BB-3 configurations, as depending on this the adsorption energy could vary by around 10 kJ/mol, while for BB-1 there is a difference of just few kJ/mol. The geometries reported in this work are those with the lowest energies, considering different starting positions for the optimisations that cover the described cases.

Given the completeness of the work of Mino et al., a direct one-to-one comparison is available[1]. Considering the results presented in this work, BB-1 presents the lowest adsorption energy (-99.5 kJ/mol), followed by BB-2 (-29.8 kJ/mol) and BB-3 (+54.9 kJ/mol), in contrast with their results which

showed $E_{ads\text{-}BB1}$=-43.1 kJ/mol, $E_{ads\text{-}BB2}$=-61.1 kJ/mol and $E_{ads\text{-}BB3}$=-18.0 kJ/mol. Although there are evident differences in the adsorption energy values for the same geometry, possibly addressable to the previously mentioned considerations about input parameters, the focus should be on the relationship between the different adsorption configurations considering the same computational framework. In fact, it is noticeable that they did not obtain the relationship $E_{BB\text{-}1} < E_{BB\text{-}2} < E_{BB\text{-}3}$, as in their case $E_{BB2} < E_{BB1} < E_{BB3}$. Moreover, the positive value we obtained for BB-3 implies that this geometry is not stable, while BB-1 should be the preferred one. Nevertheless, BB-3 was included in Table 5.c.2 because they suggested it was detected via FTIR spectroscopy.

Comparing geometrical parameters, the only significant difference we could observe is that BB-1 presents $\alpha$(Ti-$O_m$-C) angles equal to 145.9 and 154.6°, while for BB1 (Mino et al.) this value is 135.8°.

## Summary of results and implications

The preceding discussion required a meticulous analysis of carbon dioxide adsorption geometries on the anatase (001) surface. To summarize the insights obtained, the investigations that were conducted on the stoichiometric surface yielded results in complete alignment with existing literature. Specifically, the Monodentate Carbonate (MC) geometry emerged as the most stable configuration among those analysed. Consistent with prior studies and corroborated by independent internal validation, alternative geometries, particularly the linear (L) configuration, exhibit susceptibility to multiple local minima.

Regarding the hydroxylated surface, which assumes the dissociative adsorption of a water molecule into $H^+$ and $OH^-$ ions, the formation of Bidentate Bicarbonate (BB) represents the most energetically favourable state. Given the various hypothetical orientations, extensive geometric verifications of the BB configuration were required. These analyses revealed that only one specific orientation, designated as BB-1, exhibits a considerably lower adsorption energy than the others, thereby suggesting its thermodynamic stability.

Significantly, the presence of co-adsorbed water was found to enhance $CO_2$ affinity; specifically, the linear (L) configuration exhibits a lower adsorption energy on the hydroxylated surface compared to the stoichiometric $TiO_2$ substrate. The implications of this phenomenon will be primarily addressed from an experimental perspective, as a complete computational study would require the analysis of the associated energy barriers, entailing a prohibitive computational cost.

# References

[1] L. Mino, G. Spoto, and A. M. Ferrari, 'CO2 Capture by TiO2 Anatase Surfaces: A Combined DFT and FTIR Study', *Journal of Physical Chemistry C*, vol. 118, no. 43, pp. 25016–25026, Oct. 2014, doi: 10.1021/JP507443K.

[2] F. Wu, Y. Du, S. Lv, C. Zhao, and X. Yang, 'DFT Modeling of CO2 Adsorption and HCOO• Group Conversion in Anatase Au-TiO2-Based Photocatalysis', *ACS Omega*, vol. 7, no. 8, p. 7179, Mar. 2022, doi: 10.1021/ACSOMEGA.1C06861.

[3] Ž. Kovačič, B. Likozar, and M. Huš, 'Electronic properties of rutile and anatase TiO2 and their effect on CO2 adsorption: A comparison of first principle approaches', *Fuel*, vol. 328, p. 125322, Nov. 2022, doi: 10.1016/J.FUEL.2022.125322.

[4] S. Huygh, A. Bogaerts, and E. C. Neyts, 'How Oxygen Vacancies Activate CO2 Dissociation on TiO2 Anatase (001)', *Journal of Physical Chemistry C*, vol. 120, no. 38, pp. 21659–21669, Sep. 2016, doi: 10.1021/ACS.JPCC.6B07459.

[5] P. Rezaee *et al.*, 'DFT study on CO2 capture using boron, nitrogen, and phosphorus-doped C20 in the presence of an electric field', *Scientific Reports 2024 14:1*, vol. 14, no. 1, pp. 12388-, May 2024, doi: 10.1038/s41598-024-62301-x.

[6] R. Erdogan, O. Ozbek, and I. Onal, 'A periodic DFT study of water and ammonia adsorption on anatase TiO2 (001) slab', *Surf. Sci.*, vol. 604, no. 11–12, pp. 1029–1033, Jun. 2010, doi: 10.1016/J.SUSC.2010.03.016.

# 5.d Computational and experimental identification of the vibrational frequencies of adsorbates

*This section of the thesis is the result of an original and independent analysis regarding carbon dioxide adsorption on titania samples. It should be noted that the XPS measurements were conducted by Dr. Xavier Noirfalise and analysed under the supervision of Prof. Carla Bittencourt.*

Following the detailed description of the $CO_2$ adsorption geometries on the (001) and (101) anatase surfaces, an experimental validation is required to confirm the accuracy of the simulations. To this end, the vibrational frequencies were identified for each of the calculated geometries, enabling the use of infrared and Raman spectroscopies to detect potential adsorbates on samples of anatase. $TiO_2$ here employed was synthesized to promote the preferential exposure of the (001) facet. Since the primary objective of this thesis is not to identify the optimal synthesis procedure for a powder with such characteristics, the details regarding sample synthesis and characterization are reported in Chapter 7 as supplementary information. Inevitably, this does not apply to the measurement of surface adsorbates, which instead represents a cornerstone of this chapter. Figure 5.d.1 schematically illustrates the vibrational mode directions for the $CO_2$ adsorption configurations simulated on (001) anatase.

The FTIR data, and subsequently also the results from the other characterizations performed, will reveal the fundamental role of water in promoting $CO_2$ adsorption, as already hypothesized following the analysis of the computational data. In the experimental phase, this was achieved simply by placing an aliquot of $TiO_2$ powder, generally the few milligrams sufficient to perform the subsequent characterization, onto a laboratory glass slide. Afterwards, a few drops of Milli-Q water (a few hundred microliters) were used to wet the powder, taking care to ensure a uniform distribution of the liquid, occasionally by means of brief mechanical mixing. The sample was then placed under a chemical fume hood to facilitate rapid drying and to avoid contamination from microscopic airborne particles.

It is therefore significant that all vibrational spectroscopy measurements were not conducted under a controlled atmosphere. Conversely, the XPS measurements were carried out under high-vacuum conditions, as this is a necessary requirement for the execution of the technique. Consequently, in no case was $CO_2$ adsorption performed via forced carbonation or through temperature variations.

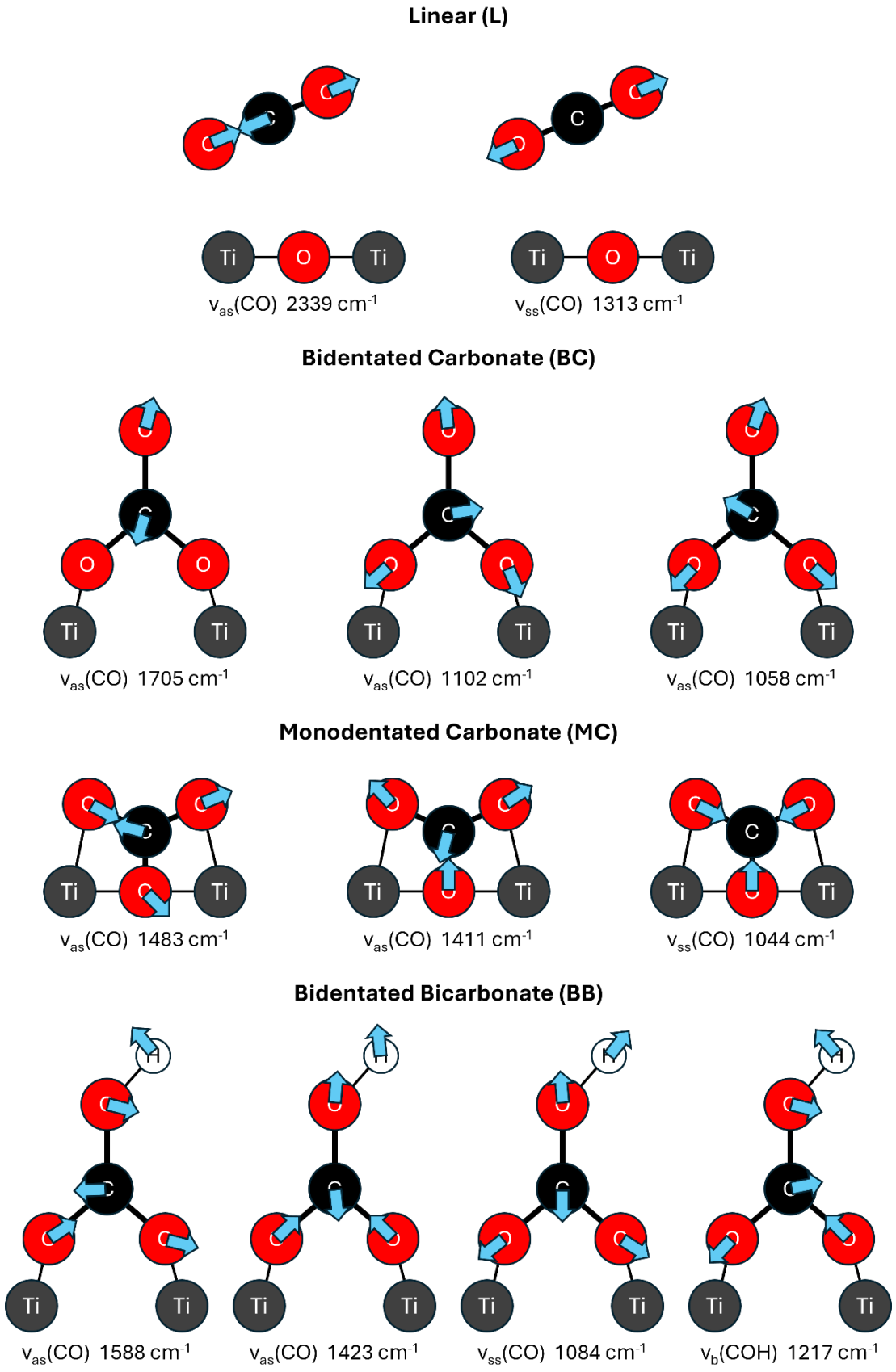



***Figure 5.d.1:*** *Schematic representation of vibrational mode directions for selected calculated adsorption geometries. This simplified model excludes vibrational intensities and anharmonic corrections.*

## Vibrational frequencies of $CO_2$ adsorbed on the stoichiometric (001) anatase slab

| | Gas-phase | L (on 101) | L | BC | MC |
|---|---|---|---|---|---|
| Eads (kJ/mol) | - | -17.5 | -13.5 | -125.9 | -151.9 |
| $\nu_{as}$(CO) (cm-1) | 2317 (2349) | 2327 (2357) | 2312 (2339) | 1676<br>1051<br>1050<br>(1705)<br>(1102)<br>(1058) | 1451<br>1394<br>(1483)<br>(1411) |
| $\nu_{ss}$(CO) (cm-1) | 1336 (1322) | 1335 (1321) | 1330 (1313) | - | 1032 (1044) |

*Table 5.d.1: Adsorption energies and vibrational frequencies for gas-phase and adsorbed $CO_2$ on the stoichiometric (001) anatase, with (101) anatase data for comparison. Values in parentheses exclude anharmonic corrections. $\nu_{as}$: asymmetrical stretching, $\nu_{ss}$: symmetrical stretching.*

From the vibrational frequencies reported in Table 5.d.1, it can be observed that the asymmetric stretching of $CO_2$ is not drastically modified when L adsorption occurs, due to the weak interaction between the slab and the molecule which does not allow $CO_2$ bending. This could represent a dramatic issue for experimental detection, as an eventual peak associated with the $\nu_{as}$(CO) of the adsorbate could be overlapped by the vibration of the gas-phase molecule, although the adsorbed $CO_2$ peak is expected not to show the typical splitting consequence of the roto-vibration. On the contrary, BC and MC present a completely different situation, as two different frequencies can be directly associated with $\nu_{as}$ of the adsorbed $CO_2$, both with a drastically lower energy with respect to the gas phase. This is because the linearity of the molecule is not maintained but all the atoms involved in the adsorption process, including those belonging to the slab, are roughly on the same plane, allowing two orthogonal modes, one of them normal to the surface while the other is parallel to it. The MC $\nu_{as}$ peaks lie in the region of the infrared spectrum typically associated with the carbonate group[1]. Differences in the structural parameters that could be observed by comparing results from the work of Mino et al. may be the reason for the huge discrepancies in the frequencies[2]. However, it could be the consequence of the different computational methods employed for the calculation of vibrational modes.

## $CO_2$ adsorption on the hydroxylated anatase (001) slab

| | L* | $L_b$* | BB-1 | BB-2 | BB-3 |
|---|---|---|---|---|---|
| $E_{ads}$ (kJ/mol) | -21.0 | -46.2 | -99.5 | -29.8 | +54.9 |
| $\nu_{as}$(CO) ($cm^{-1}$) | 2331 (2360) | - (2338) | 1557 (1588) 1395 (1423) | 1525 (1558) 1352 (1386) | 1509 (1551) 1333 (1359) |
| $\nu_{ss}$(CO) ($cm^{-1}$) | 1351 (1319) | - (1316) | 1070 (1084) | 1042 (1056) | 1012 (1032) |
| $\nu_b$(COH) ($cm^{-1}$) | - | - | 1190 (1217) | 1171 (1212) | 1196 (1203) |

***Table 5.d.2:*** *Adsorption energies and vibrational frequencies for gas-phase and adsorbed $CO_2$ on the hydroxilated (001) anatase. Values in parentheses exclude anharmonic corrections. $\nu_{as}$: asymmetrical stretching, $\nu_{ss}$: symmetrical stretching, $\nu_b$: bending.*

Table 5.d.2 shows that even when the (001) anatase surface includes a dissociated adsorbed water molecule, the vibrational frequencies of Linear $CO_2$ (L) do not vary considerably. In the case of the $L_b$* geometry, applying the anharmonic correction was not possible due to the instability of the configuration. Indeed, despite being a local minimum, during the calculation of the dynamics required to define the trajectory, the geometry spontaneously tends to convert into a BC configuration. This finding is highly significant, as it suggests that $H_2O/CO_2$ co-adsorption on the (001) anatase surface promotes the formation of more stable adsorption geometries.

Regarding the three different Bidentate Bicarbonate (BB) configurations, the vibrational frequency of the $\nu_{as}$ mode is considerably different from that of the carbonate groups described in the previous section. In general, however, it can be verified that the spectral window affected by vibrations of both carbonates and bicarbonates ranges between 1000 and 1600 $cm^{-1}$, with each geometry exhibiting a characteristic pattern that would allow its presence to be distinguished from the others.

## FTIR characterization

The FTIR spectra were recorded using a Nicolet iN10 MX infrared imaging microscope (Thermo Scientific, USA) with a spectral resolution of 2 $cm^{-1}$ over the range of 4000–675 $cm^{-1}$ equipped with a liquid nitrogen cooled MCT detector. A small amount of sample was directly placed on a gold-coated glass slide and measured using a reflection setup, after the collection of a background spectrum from a clean spot of the support. Each measurement consisted of 64 scans per replicate, with a collecting duration of 23 seconds, and three replicates were taken per sample. Spectra later reported represent the mean between the three replicates.

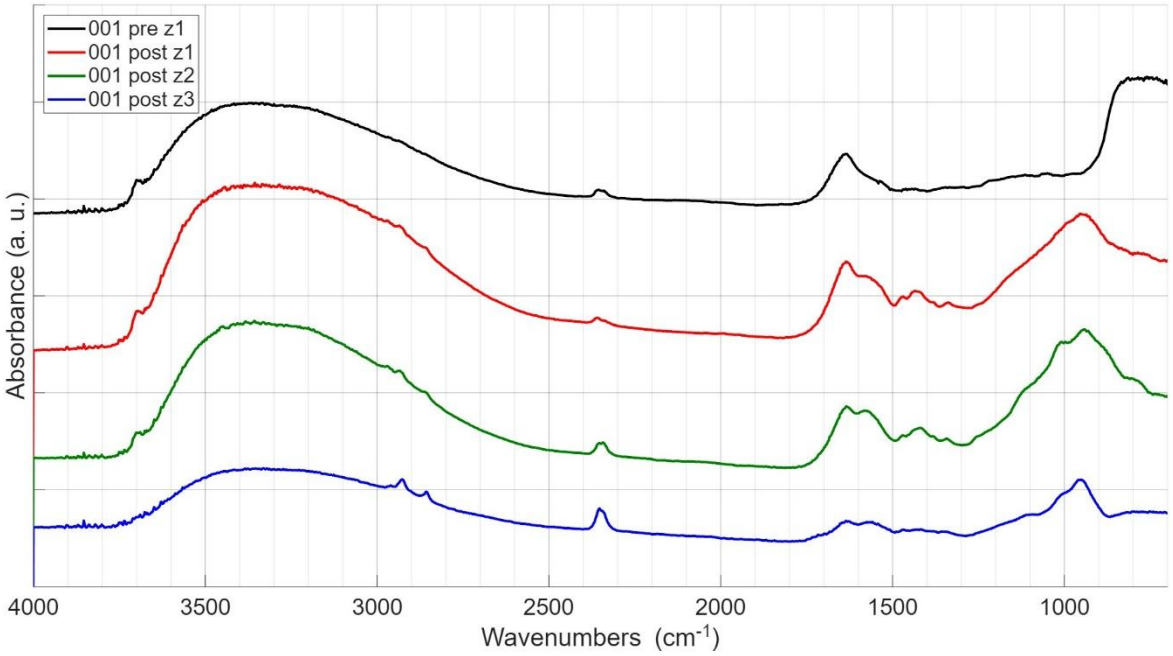



***Figure 5.d.2:*** *FTIR spectra of the (001) anatase sample before and after the hydration-dehydration treatment, as described at the beginning of this chapter. Three measurements acquired from different spots on the treated sample are reported to verify the presence of any sample inhomogeneity.*

In Figure 5.d.2, FTIR spectra obtained measuring the synthesized TiO2 powder are reported (001 pre z1). The predominant contributions in the spectrum are due to the presence of structural water in the sample, despite the synthesis including a thermal treatment at 500 °C aimed at removing it. The purpose of the calcination was also related to the removal of any organic contaminants remaining after the hydrothermal synthesis and the subsequent washing of the powder with ethanol. In this regard, it is indeed possible to notice the absence of the characteristic features of organic molecules, which would be given by C-H stretching in the region around 3000 $cm^{-1}$. The presence of an isolated

peak slightly more energetic than the water-associated band indicates the presence of OH groups that do not form complex hydrogen-bonded interactions.

The presence of $CO_2$ is clearly identifiable by its asymmetric stretching at 2349 $cm^{-1}$, despite the environmental background being obviously properly measured and subtracted prior to the measurement. This would therefore suggest the presence of adsorbed $CO_2$; considering the computational results, a Linear (L) geometry would be assumed, given that the peak frequency is unmodified. In support of this, the peak shape can also be analysed, which in the case of gas-phase $CO_2$ is characterized by the typical rotational-vibrational split. In the case under consideration, although the peak splitting is slightly visible, it is barely noticeable compared to the overall intensity of the feature. The presence of $CO_2$ adsorbed with such geometry would suggest that, despite the efforts made to have preferentially exposed (001) crystal plane, a considerable presence of (101) exposed crystal plane is still present. The latter, as previously clarified, only allows the L adsorption geometry for $CO_2$.

No features attributable to carbonates and bicarbonates are present in the analysed spectrum, although these structures were predicted to be energetically favourable following $CO_2$ adsorption. For this reason, considering the computational data, an additional step was conducted. Indeed, regarding the behaviour of simulated surfaces under different supercell dimensions, it has been demonstrated how the co-presence of multiple $CO_2$ molecules can favour the adsorption of the molecule on the surface. This is supported by the fact that in some relevant studies of $CO_2$ adsorption on titania, a controlled atmosphere of $CO_2$ or $CO_2/H_2O$ is utilized[2], [3]. Due to the impossibility of performing an in-situ test under these conditions, since they require dedicated, non-general-purpose instrumentation unlike the Nicolet spectrometer used for these measurements, a different test was considered.

This clearly refers to the hydration-dehydration treatment under room conditions, as previously described within this chapter. Following this process, the (001) anatase sample was measured again (Figure 5.d.2). After the treatment, peaks emerged in the 1600–1300 $cm^{-1}$ region, with a prominent band centred at 937 $cm^{-1}$ affecting lower frequency regions, where peak identification became impractical. Clear peaks associated with C-H stretching were evident at 2966, 2928, and 2856 $cm^{-1}$. Interestingly, the peak shape of the $CO_2$ asymmetric stretching seems to show a reduced splitting, suggesting adsorbed $CO_2$ due to a lesser influence of rotational-vibrational phenomena.

To analyse the 1600-1300 $cm^{-1}$ region, the mean of three spectra of the sample before the hydrating-dehydrating treatment was subtracted from the mean calculated over three measurements acquired after the treatment. The resulting spectrum was slightly smoothed employing the Savitzky-Golay filter (polynomial order=3, window length=9) to reduce the spectral noise. Figure 5.d.3 reports the spectrum here described in a narrower spectral window, enhancing the detection of the peaks in the region under interest. The subtraction operation had the effect of slightly modifying the peak positions by around 5–10 $cm^{-1}$.

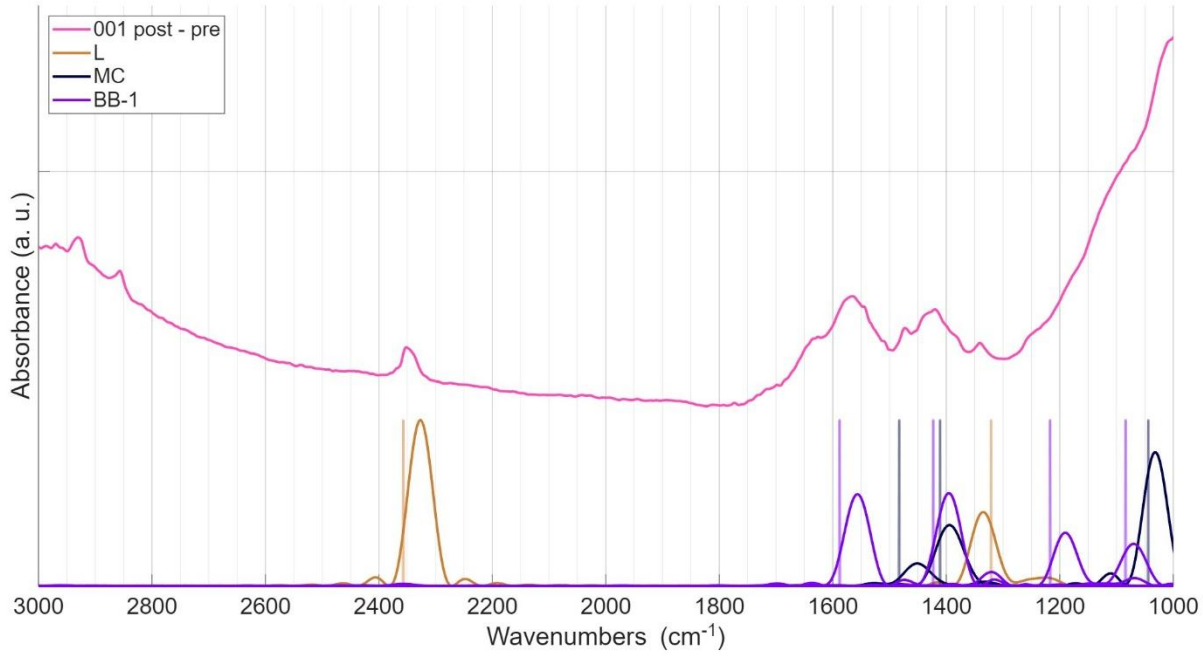



***Figure 5.d.3:*** *Difference between the average of three FTIR spectra of the (001) anatase sample after and before the hydration-dehydration treatment. A mild smoothing with the Savitzky-Golay filter was applied to enhance readability. The calculated vibrational frequencies for the three most relevant geometries identified in the previous chapter are reported. Frequencies computed within the harmonic approximation are represented as stick spectra, whereas the power spectra display the vibrational features refined through anharmonic corrections.*

Many of the peaks observed in the region 1600-1300 cm-1 correlate with calculated values for several geometries, specifically L on (101), MC on (001), and BB-**1** on hydroxylated (001). For this reason, calculated vibrational frequencies under the anharmonic approximation and power spectra including the harmonic correction are reported in Figure 5.d.3 for a rapid comparison. It is noted that the peak at 1437 $cm^{-1}$ could represent the bending of a -$CH_2$ group, given the clear presence of organic molecules in the post-treatment samples.

The highlighted adsorption geometries represent the most stable configurations under three different conditions. The L geometry is the most stable on the exposed (101) facet, supporting the hypothesis of its significant contribution as an exposed facet. The MC configuration represents the most stable geometry on the stoichiometric (001) anatase, a finding widely shared in the literature. Among the various bicarbonate-associated geometries evaluated, BB-1 represents the most stable configuration according to the calculations conducted under the computational conditions characterizing the present study. Other works, under different computational conditions, would seem to indicate BB-2 as the most stable. The vibrational frequencies calculated for both geometries are virtually overlapping; therefore, an experimental confirmation of the bicarbonate group orientation (BB-1 or BB-2) remains difficult to achieve.

More generally, the high level of agreement between simulations and experimental characterization reinforces the hypotheses advanced so far, regarding both the computational parameters and the results obtained via DFT. The most relevant hypothesis, namely the role of water in promoting $CO_2$ adsorption, appears to be unequivocally verified.

## Raman characterization

Raman spectra were acquired in backscattering configuration using a LabRAM HR spectrometer equipped with a He–Ne laser (λ = 633 nm). The laser beam was focused onto the sample, and the scattered light collected, through a 50× microscope objective (Numerical Aperture: 0.5) without the use of attenuation filters. To compensate for the expected low concentration of the adsorbate, arising from the limited surface-to-bulk ratio of the crystals, the exposure time was extended to 120 seconds. This prolonged acquisition was feasible due to both the absence of $TiO_2$ characteristic features within the investigated spectral region (1000–3500 $cm^{-1}$) and the lack of fluorescence, which prevented signal saturation.

Anatase exhibits a characteristic spectrum in the region below 1000 $cm^{-1}$. Since the characterization of $TiO_2$ is beyond the scope of this chapter, a detailed discussion of this measurement is deferred to Chapter 7, which provides an in-depth analysis of both the crystalline phase and the critical aspects regarding the identification of the exposed cleavage plane.

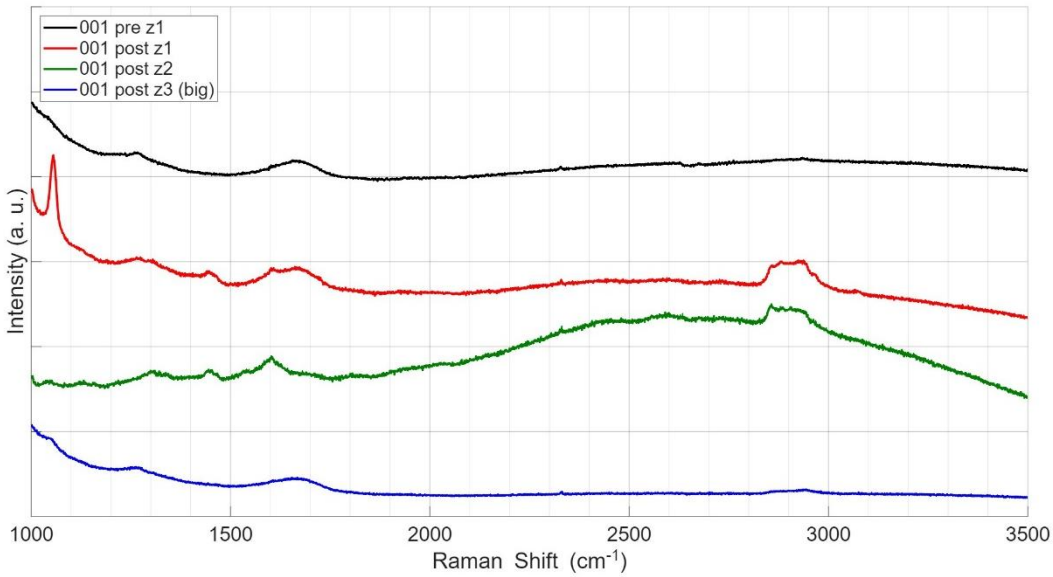



***Figure 5.d.4:*** *Raman spectra of the (001) anatase sample before and after the hydration-dehydration treatment, as described at the beginning of this chapter. Three measurements acquired from different spots on the treated sample are reported to verify the presence of any sample inhomogeneity.*

The Raman spectra in the spectral region between 1000 and 3500 $cm^{-1}$ are shown in Figure 5.d.4. As already observed in the case of infrared spectroscopy, the hydration and dehydration treatment allowed the identification of spectral features compatible with organic species and carbonates. The resulting detailed analysis would be very similar to what has already been presented for the FTIR data; however, it should be highlighted that, due to the limitations of the computational methods employed, there is a lower level of accuracy in predicting the Raman spectral features.

In the Raman spectra, more than for the FTIR data, there is a higher degree of internal inhomogeneity within the material. Based on several repeated trials, it appears that there is a greater sensitivity to adsorbed species when focusing on smaller microparticles. Spectra acquired on larger particles, but still with a diameter under one millimetre, present less resolved spectral features of any adsorbed species. In this regard, it is noted for example how in Figure 5.d.4 the presence of C-H stretching in the spectrum of the sample named 'big' is barely visible compared to the other two spectra acquired on smaller particles. For comparison, the C-H stretching is not visible in the case of the sample before the hydration and dehydration process.

Analogously to the infrared spectroscopy analysis, the spectra of the (001) anatase sample collected after the hydration and dehydration treatments were compared with the DFT-calculated vibrational frequencies. Due to the clear intra-sample inhomogeneity observed in Figure 5.d.4, the spectrum of

the larger particle ("big") was excluded, and the remaining two replicates were not averaged. Figure 5.d.5 displays these background-subtracted spectra, from which the spectrum acquired prior to the hydration procedure was removed. As previously noted, the calculated frequencies are less predictive of the adsorbed species compared to the FTIR spectroscopy observations.

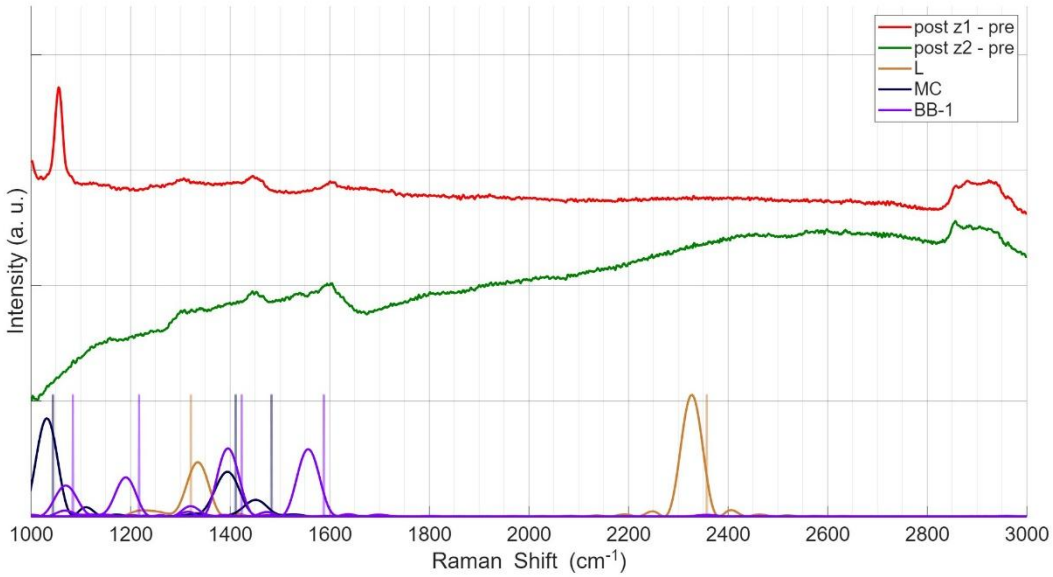



*Figure 5.d.5: Comparison between calculated vibrational frequencies and experimental Raman spectra. Calculated harmonic frequencies are displayed as stick spectra, while power spectra include anharmonicity corrections. The spectrum of the pristine powder was subtracted from the spectra of the two different spots on the anatase (001) sample following the hydration-dehydration cycle. A minor smoothing was applied to the experimental curves to improve peak resolution.*

## XPS characterization

X-ray photoelectron spectroscopy (XPS) measurements were performed using a PHI GENESIS spectrometer (Physical Electronics) operated under ultra-high vacuum conditions and equipped with a monochromatic Al Kα X-ray source (hν = 1486.6 eV). Survey spectra were acquired to determine the elemental composition of the sample surface, while high-resolution core-level spectra were recorded to investigate carbon hybridization states. To compensate for charging effects, the binding energy scale was calibrated by referencing the adventitious carbon peak to 284.6 eV. Data processing and peak fitting were carried out using CasaXPS software.

The purpose of the XPS measurements was to confirm the results obtained from the combined DFT and infrared spectroscopy approach, particularly regarding the role of water as a promoter for $CO_2$

adsorption. For this reason, the measurements were performed on the as-synthesized anatase (001) and following the hydration-dehydration process under ambient conditions. For comparison, a commercial $TiO_2$ sample (Hombikat) was also measured using the same approach. The advantage of XPS over the other techniques used is its ability to probe exclusively the outermost layers of the sample, within approximately 10 nm from the actual surface, thereby providing higher sensitivity toward potential adsorbates.

The survey scan reveals that the elemental composition of the samples consists substantially of titanium, oxygen, and carbon, the latter presumably adventitious. It is worth noting that in other measurements performed on both synthesized and commercial $TiO_2$ samples (not reported here), potential contamination from other elements, specifically chlorine and nitrogen, was identified. Although these percentages are remarkably low and therefore negligible, in some cases the Raman spectrum of titania can exhibit a peak at around 2330 $cm^{-1}$ (as shown in Figure 5.b.3), which can be assigned to the vibration of the $N_2$ molecule. The elemental composition calculated on the high resolution XPS spectra of the samples is reported in Table 5.d.3, clearly demonstrating that the differences in terms of elemental composition are negligible.

| | 001 – pre | 001 – post | Hombikat – pre | Hombikat- post |
|---|---|---|---|---|
| C | 15% | 12% | 11% | 12% |
| O | 59% | 61% | 63% | 62% |
| Ti | 26% | 27% | 26% | 26% |

***Table 5.d.3:*** *elemental composition of the samples of (001) anatase and Hombikat before and after $H_2O$ treatment*

Figure 5.d.6 shows the high-resolution carbon spectra of the $TiO_2$ samples under investigation. For the (001) anatase sample, a pronounced spectral modification is visually apparent at 287.6 eV following the water treatment. This is consistent with the increase in the percentage of carbonates relative to $sp^3$-hybridized carbon. A forced carbonation experiment conducted by Barteau and Madix (1983) on an oxidized silver surface yielded analogous results, thus strongly supporting the validity of this hypothesis[4]. This phenomenon was also observed in the spectra of the Hombikat sample, albeit less prominently.

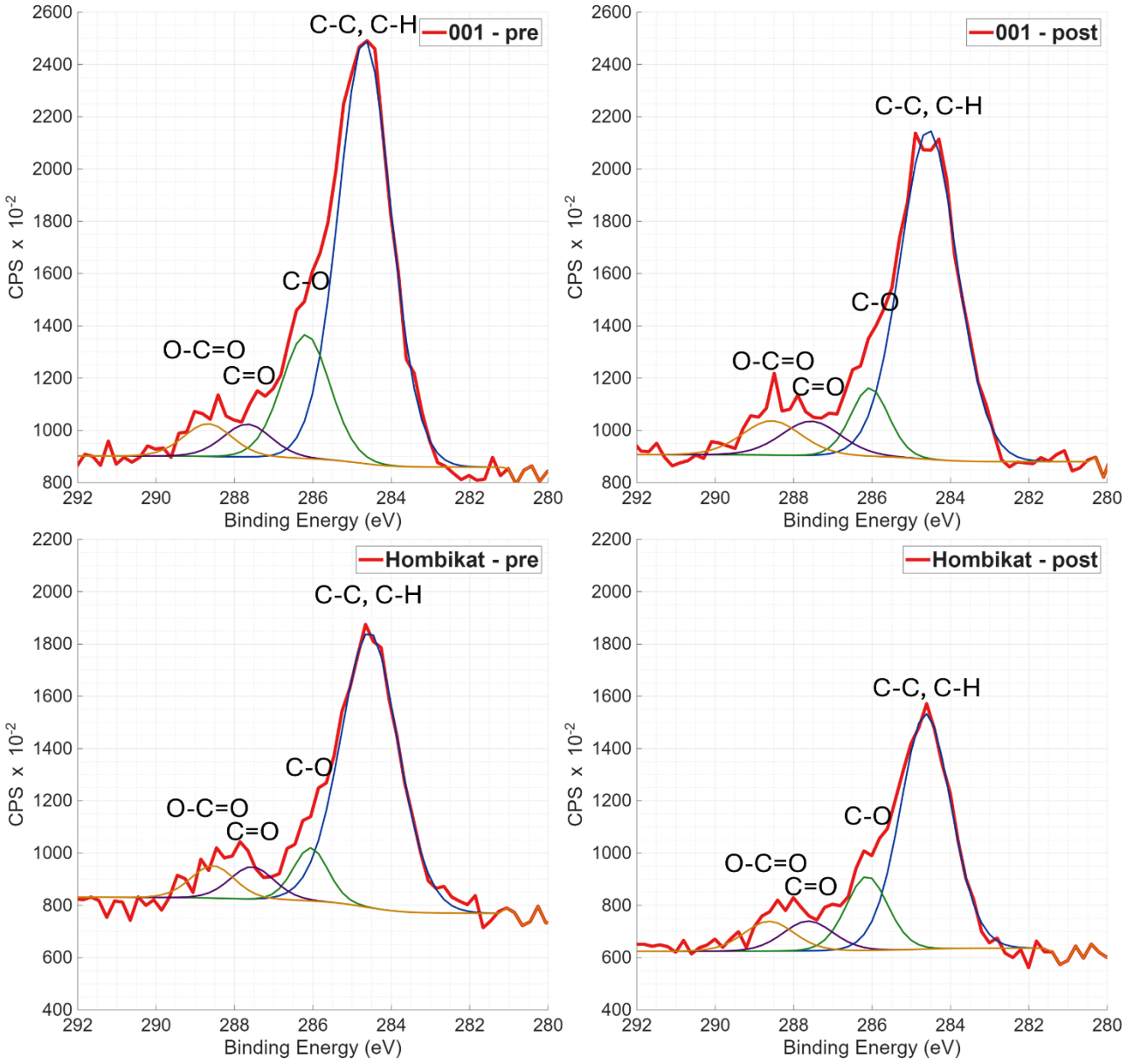



***Figure 5.d.6:*** *XPS characterization of the samples of (001) anatase and Hombikat before and after $H_2O$ treatment. The measured spectra are reported in red; the components, ordered from the lowest to the highest energy, are indicative of "C-C, C-H", "C-O", "C=O", and "O-C=O" bonds, respectively.*

Comparing the results obtained in this work with studies specifically focused on carbonates measured via XPS, it is worth noting that the binding energy of the peak under consideration is lower than the values reported in several handbooks, which are typically above 289.0 eV[5], [6]. Silver carbonate is often considered an exception to these standards, with handbook values indicating its position around 288.5 eV[5]. However, this is not entirely confirmed, as a widely known database reports the predominant peak of silver carbonate at 289.2 eV[7]. In any case, this is significantly different from what was reported in the work of Barteau and Madix, where the peak is characterized by an energy

of 287.7 eV, which is closely comparable to the value of 287.6 eV measured on the samples analysed in this thesis[4].

The most convincing hypothesis to explain this phenomenon is that, in the case of a bulk (silver) carbonate sample, the binding energy appears higher, at approximately 289 eV. Regarding carbonates adsorbed on the surface, the BE decreases to about 287.6 eV, evidently due to the different chemical environment of the carbon atom. More specifically, considering that carbonate formation occurs following $CO_2$ adsorption on an oxidized metal surface, one of the three oxygen atoms forming the carbonate ion "belongs" to the surface; therefore, prior to molecule adsorption, it already forms stable bonds with the surface metal atoms. It can be deduced from this that the $O_2^-$-$CO_2$ interaction is less strong, resulting in a decrease in the BE associated with the carbonate.

Table 5.d.4 reports the results concerning the chemical state of carbon in the different cases. For the (001) anatase sample, a significant decrease in the C-O percentage is observed in favour of C=O and O-C=O (assigned to carbonate according to the previous interpretation) following the water treatment. Remarkably, the increase in carbonates is also identifiable in the commercial titania sample, albeit to a lesser extent, but a different variation occurs in its carbon profile. Indeed, a decrease in C-C and C-H bonds is clearly apparent, mainly in favour of C-O.

| | 001 – pre | 001 – post | Hombikat – pre | Hombikat- post |
|---|---|---|---|---|
| C-C, C-H | 71% | 74% | 77% | 66% |
| O-O | 19% | 10% | 9% | 17% |
| C=O, O-C=O | 10% | 16% | 14% | 17% |

*Table 5.d.4: chemical state of carbon in the samples of (001) anatase and Hombikat before and after $H_2O$ treatment*

However, given the relatively minor role that the XPS characterization has assumed in the overall work on titania and its interaction with $CO_2$, the conclusions that can be drawn from this section remain limited. Consequently, further experiments are deemed necessary to confirm the proposed hypotheses.

## Conclusions on the computational and spectroscopic characterization of adsorbates

DFT simulations allowed for the identification of the most stable adsorption geometries under both conditions, in the presence and absence of water. Summarizing the results from the analysis reported in the previous chapter, the three most relevant geometries are the Linear (L), Monodentate Carbonate (MC), and Bidentate Bicarbonate (BB-1) configurations. The vibrational frequencies of the various adsorption geometries were calculated, initially by including solely the harmonic approximation and subsequently, after defining the trajectories describing the vibration, the anharmonic component as well. Through this approach, it was possible to evaluate the shift dictated by the inclusion of the correction, along with the relative intensities of the various vibrational features.

Infrared spectroscopy (FTIR) measurements of the $TiO_2$ synthesized with the (001) anatase facet as the preferentially exposed crystalline plane did not allow for the identification of the predicted characteristic carbonate modes. The critical challenges encountered during the synthesis and characterization of the powder, particularly regarding the identification of the preferentially exposed crystalline plane, are not reported in this section of the thesis but are presented in a dedicated chapter.

On the sample measured directly after the synthesis process, the only relevant FTIR peak is that associated with the asymmetric stretching of $CO_2$. Following the hydration and dehydration treatment conducted under ambient conditions, the FTIR spectrum of the sample changed drastically, clearly identifying the presence of adsorbed organic compounds, an absorption band at wavenumbers below 1200 $cm^{-1}$, and several relevant peaks in the 1600–1200 $cm^{-1}$ region. Among these, an almost unique correspondence was identified between the DFT-predicted and the measured spectra.

Therefore, this experiment not only allowed for the identification of the presence of carbonates on the sample surface, likely resulting from the adsorption of atmospheric $CO_2$, but also enabled the verification of the role of water in promoting adsorption. This step had also been hypothesized by analysing the simulations conducted in the presence of water chemisorbed on the (001) anatase surface.

The computational model applied for calculating vibrational frequencies has certain limitations when aiming to obtain a Raman spectrum. For this reason, the same experiment conducted within the framework of FTIR measurements led to similar results, even though the DFT-predicted frequencies

are less accurate. Nevertheless, it is worth emphasizing that the role of water was clearly recognized in this case as well.

Finally, XPS characterization confirmed that the increase in carbonates affects the outermost layers of the sample, which is compatible with an adsorption process. A significant increase was observed in the sample synthesized with the preferentially exposed anatase (001) facet, whereas this increase was more limited for the commercial sample used as a reference. Interestingly, and not yet thoroughly investigated, the two samples exhibited different behaviours following the hydration and dehydration treatment.

This work is believed to have improved the general understanding of the geometries and adsorption mechanisms of $CO_2$ on titania, providing more robust computational models for predicting experimental behaviours. Demonstrating that this process can occur under ambient conditions and is mediated by the presence of water could represent a breakthrough for future applications aimed at converting carbon dioxide into energy carriers.

## References

[1] J. Coates, 'Interpretation of Infrared Spectra, A Practical Approach', *Encyclopedia of Analytical Chemistry*, Oct. 2000, doi: 10.1002/9780470027318.A5606.

[2] L. Mino, G. Spoto, and A. M. Ferrari, 'CO2 Capture by TiO2 Anatase Surfaces: A Combined DFT and FTIR Study', *Journal of Physical Chemistry C*, vol. 118, no. 43, pp. 25016–25026, Oct. 2014, doi: 10.1021/JP507443K.

[3] J. Dankar, C. Pagis, M. Rivallan, and M. El-Roz, 'Operando FTIR study of the photocatalytic reduction of CO2 in the presence of water vapor over Pt/TiO2: on the role of surface residual C-species', *Sustain. Energy Fuels*, vol. 7, no. 12, pp. 2819–2823, Jun. 2023, doi: 10.1039/D3SE00227F.

[4] M. A. Barteau and R. J. Madix, 'Photoelectron spectra of adsorbed carbonates', *J. Electron Spectros. Relat. Phenomena*, vol. 31, no. 2, pp. 101–108, Jan. 1983, doi: 10.1016/0368-2048(83)80013-9.

[5] 'X-ray Photoelectron Spectroscopy (XPS) Reference Pages: C 1s- Carbonates'. Accessed: Jun. 17, 2026. [Online]. Available: https://www.xpsfitting.com/2011/03/c-1s-carbonates.html

[6] L. Caracciolo, L. Madec, and H. Martinez, 'XPS Analysis of K-based Reference Compounds to Allow Reliable Studies of Solid Electrolyte Interphase in K-ion Batteries', *ACS Appl. Energy Mater.*, vol. 4, no. 10, pp. 11693–11699, Oct. 2021, doi: 10.1021/ACSAEM.1C02400.

[7] 'Carbon Spectra - Ag2(CO3) - Silver Carbonate - The International XPS Spectra-Base of Monochromatic XPS Reference Spectra'. Accessed: Jun. 17, 2026. [Online]. Available: https://xpsdatabase.com/cacarbon-sspectra-ag2co3-sisilver-cacarbonate/

# 5.e Simulations of single-site catalysts: examples with calcium and magnesium

Previously reported results revealed good agreement between the geometries predicted by Density Functional Theory and the experimentally observed ones. The study focused on (001) anatase, which has gathered interest due to its considerable surface energy and because data from the literature, although limited, converged on its capability to adsorb $CO_2$. However, several criticalities introduced by the synthesis of a sample with this specific crystal plane as the preferred exposed facet could pose serious safety and scalability limitations.

Indeed, while the adsorption capabilities of (001) anatase for carbon dioxide were successfully demonstrated, and a reliable computational setup for predicting vibrational frequencies was established, the specific bottlenecks of this synthesis route warrant detailed examination. Chief among these concerns is the substantial percentage of isopropyl alcohol (IPA) used as a reaction medium, which remains a hazard despite partial dilution in water. Hydrothermal synthesis demands concurrent high temperatures and pressures, conditions under which the organic solvent risks autoignition, posing severe danger to operators[1].

Furthermore, volume constraints severely hinder scale-up; laboratory hydrothermal vessels rarely exceed a few hundred millilitres and require at least 50% headspace to prevent an excess of pressure. Transitioning to an industrial scale does not alleviate this requirement; rather, scaling up a reaction involving drastically larger volumes of a volatile solvent exacerbates pressure management issues. This volumetric restriction inherently limits the throughput of the titanium precursor. This precursor is often pyrophoric, compounding the chemical handling risks. Finally, the mandatory use of hydrofluoric acid (HF) as a morphology-controlling capping agent introduces critical toxicity hazards, demanding highly specialized personnel and stringent safety engineering controls.

For this reason, a new approach was considered, starting from commercial, inexpensive samples of $TiO_2$ decorated with metal ions. Among others, $Ca^{2+}$ and $Mg^{2+}$ were selected as a starting point to define this case study. Due to the absence of a preferentially exposed facet in general $TiO_2$ samples, the (101) anatase facet was believed to be the most frequent one due to its low formation energy. The crystal phase did not represent a critical factor, as it is predominant, if not exclusive, in many commercial $TiO_2$ powders employed in catalytic applications.

Another factor that should be considered is the conversion of the catalyst to a more stable structure, which does not necessarily entail the transformation of anatase into rutile. In fact, the conversion of (001) to (101) may happen at low temperature, even in the absence of any phase transition[2]. These factors, together with the difficulty in a direct identification of the exposed facet in the section of this thesis about the synthesis procedure, limit an actual large-scale employment of (001) anatase as catalyst, suggesting that new paths could be evaluated.

This new study aims to maintain titania as the fundamental substrate, as its photocatalytic activity is highly relevant when the chemical reaction under examination is influenced by reactant stability. The energy of the excited state could be sufficient to overcome the activation barriers that limit the conversion of $CO_2$ into other molecules of greater significance for the energy transition[3].

Since the inability of (101) anatase to adsorb $CO_2$ has already been discussed, incorporating additional compounds is required to provide active sites for adsorption. Metal ions offer promising opportunities in this regard, as they can effectively interact with the oxygen atoms of the carbon dioxide molecule. The presence of these cations modifies the surface electronic structure, potentially enhancing its overall chemical reactivity and creating favourable conditions for stable gas adsorption.

Clearly, exposed titanium atoms natively present in the material do not play a significant role into this, as they already have high coordination numbers. The focus shifted to magnesium, as it represents a key factor in $CO_2$ stabilization inside leaves[4]. Among all the compounds containing $Mg^{2+}$, magnesium hydroxide was judged a good opportunity because of the presence of strong dipoles which may promote strong interaction with the surface. $Mg(OH)_2$ presents some limitations in its employment, deriving from a lack of solubility in water; for this reason, $Ca(OH)_2$ was deeply evaluated, together with $CaCl_2$ for a side comparison.

The addition of a cocatalyst may also represent a good opportunity to limit charge recombination, which could reduce the efficiency of the catalyst. Although the work presented in this thesis does not consider energy barriers, focusing on adsorption capabilities rather than the subsequent conversion, this work aims to highlight the opportunities derived from the introduction of $TiO_2$ cocatalysts for $CO_2$ conversion. The results reported here may represent a starting point or an integration for future studies concerning this topic.

## Computational details

The convergence tests previously utilized to define a working framework capable of providing accurate results also proved to be fundamental for what is presented in this chapter of the thesis. The cut-off energy was set to 80 Ry in accordance with what was previously reported, while the use of the Γ-point for sampling the Brillouin zone in the case of a slab model was judged adequate to limit computational complexity.

The only substantial modification introduced is related to the dimensions of the slab and the supercell. Indeed, to accommodate the subsequent inclusion of metal ions on the surface, the slab was constructed by adding one layer vertically; this was done to avoid unphysical constraints that could have originated from the relative proximity between the ion and the bottom layer characterized by fixed atoms. To prevent excessively demanding computational costs, one horizontal layer was removed along the most extended direction. Although it has been demonstrated that this reduction can be critical for certain surfaces, as discussed regarding (001) anatase, there are no significant indications that this constitutes a problem for (101) anatase.

## Materials and methods

This chapter focuses on the surface modification of commercial Degussa P25 titanium dioxide $TiO_2$ through enrichment with $Ca^{2+}$ and $Mg^{2+}$ ions. Samples prepared via wet impregnation in $Ca(OH)_2$, $Mg(OH)_2$, and $CaCl_2$ solutions are characterized and compared to pristine P25 using Raman spectroscopy. The preparation of these precursor solutions followed rigorous specific criteria.

The solubility of magnesium hydroxide in water was reported to be less than 10 mg/L, and it was therefore considered poorly soluble in $H_2O$[5]. A saturated solution was prepared by mixing 30 mg of $Mg(OH)_2$ in 200 mL of Milli-Q water and vigorously stirring for 2 hours with a mild increment in temperature. As a consistent amount of $Mg(OH)_2$ did not dissolve, the obtained suspension was centrifuged at 9000 rpm for 3 minutes to separate the liquid and solid phases.

The pH of the solution changed after centrifugation from 10.2 to 9.84/9.90 (with two different samples showing different pH values). This could be the consequence of both the influence of suspended $Mg(OH)_2$ and a slight variation in temperature. The presence of suspended material even

in the centrifuged sample was not completely excluded. The concentration of dissolved $Mg(OH)_2$ in the solution was estimated to be around 4.6 mg/L, which is consistent with the references.

The $Ca(OH)_2$ solution was obtained by diluting a stock solution (pH = 12.4) until the pH reached 9.90. This was based on the consideration that the two hydroxides should have roughly similar dissociation constants, meaning that the number of metallic ions could be approximately the same at the same $H^+$ concentration. However, reliable data regarding the first and second dissociation constants for the two compounds were not identified, which limits the validity of this assumption. Within this theoretical framework, the concentration of $Mg^{2+}$ and $Ca^{2+}$ was estimated to be on the order of $10^{-4}$ M. Therefore, a $10^{-4}$ M $CaCl_2$ solution was prepared and used.

In a typical synthesis of metal-enriched P25, 100 mg of Degussa P25 were suspended in 1 mL of one of the previously described solutions and periodically shaken for 48 hours to promote interactions between the ions and the powder. The powder was then collected via centrifugation (9000 rpm, 3 min) and washed with Milli-Q water. Excess of water was removed through an overnight thermal treatment at 90 °C.

A key driving force for the work discussed in this chapter is the need for simple, cost-effective, and scalable synthetic protocols that minimize safety and environmental risks. The procedure presented herein poses no significant hazards. This stands in sharp contrast to conventional methods for synthesizing anatase with preferentially exposed (001) facets, which typically rely on hydrothermal treatments involving organic solvents and highly toxic hydrofluoric acid.

The obtained samples, alongside the pristine P25 considered as a reference, were then characterized via Raman spectroscopy, following the same setup previously described for the analysis of (001) anatase. The exposure time for Raman measurements was set to 3 s for the 100-1000 $cm^{-1}$ region and 120 s for the 1000-3500 $cm^{-1}$ region, due to the different information expected from the two regions of the spectrum.

## DFT simulations

In accordance with the procedure followed to investigate pristine $TiO_2$, the spectroscopic characterization of the material was accompanied by an extensive computational analysis aimed at identifying potential stable configurations. Given the rationale behind the study discussed in this

section of the thesis, the simulations needed to model a representative $TiO_2$ surface. Since the (101) facet has been proven to be one of the most stable $TiO_2$ surfaces due to its low surface energy, a significant presence of this exposed crystal plane is expected in commercial anatase. Consequently, this facet was selected as the substrate for the addition of metal ions. The metals chosen for this purpose were calcium and magnesium, specifically in the form of $Mg^{2+}$ and $Ca^{2+}$ ions. For this reason, calcium hydroxide, calcium chloride, and magnesium hydroxide were evaluated.

The simulations began with the placement of a molecule containing the target ion in the upper vacuum region at a moderate distance from the surface, to avoid potential artificial distortions of bond lengths and angles. Several optimizations starting from different positions may be required to address a global minimum. The simulations did not include any solvent for the previously mentioned compounds; therefore, their dissociation is not expected unless induced by the surface itself. Within this context, referring to them as molecules is appropriate.

Optimized adsorption energies and geometries for $Ca(OH)_2$, $CaCl_2$, and $Mg(OH)_2$ are reported in Figure 5.e.1 and Table 5.e.1. Each structure exhibits negative adsorption energies, which demonstrates its thermodynamic stability. As expected, due to the ionic nature of the bonds within the molecules, the positive charge of the metal and the negative charges of oxygen and chlorine lead to a similar adsorption geometry in all cases. Driven by Coulombic interactions, calcium and magnesium tend to be attracted by the surface oxygen atoms, while oxygen and chlorine coordinate with titanium.

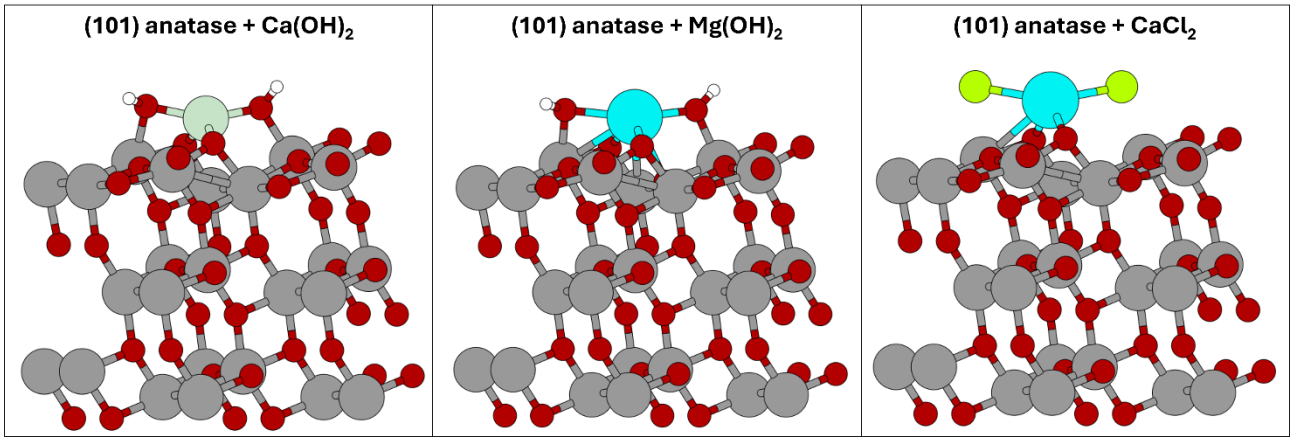



***Figure 5.e.1:*** *optimized adsorption geometries for $Ca(OH)_2$, $CaCl_2$, and $Mg(OH)_2$ on (101) anatase*

| System | Adsorption energy (kJ/mol) |
|---|---|
| (101) anatase + $Ca(OH)_2$ | -305 |
| (101) anatase + $Mg(OH)_2$ | -269 |
| (101) anatase + $CaCl_2$ | -215 |

*Table 5.e.1: adsorption energy for $Ca(OH)_2$, $CaCl_2$, and $Mg(OH)_2$ on (101) anatase*

Although the electronic structure of the metal ions is similar, there are no characteristic differences among the optimized systems in terms of geometries. A direct evaluation of the anion would not be as effective, since in a real-case scenario there are no guarantees regarding its position on the surface, and an extensive evaluation would be extremely computationally expensive. Therefore, only the evaluation of the cations is relevant. It must be noted that because of its smaller electronic shell, $Mg^{2+}$ penetrates slightly deeper into the $TiO_2$ structure than $Ca^{2+}$. This can be estimated from the z-axis coordinate of the nuclei, which in the case of $Mg^{2+}$ is around 0.02 nm lower than for $Ca^{2+}$, possibly leading to different adsorption capabilities. The graphical representation reported in Figure 5.e.1 shows more bonds involving $Ca^{2+}$, including possible Ti-Ca bonds; however, this is an arbitrary representation and does not consider the actual electronic density properly calculated by DFT.

All three previously tested configurations represent stable adsorption conditions for the chemical compound on the titania surface. Among them, the highest stability is achieved in the case of $Ca(OH)_2$ adsorption. For this reason, subsequent simulations will focus directly on the optimized (101) anatase + $Ca(OH)_2$ system, which will effectively serve as the new surface for $CO_2$ molecule adsorption. The possible adsorption geometries were based on the previous findings regarding the stoichiometric $CO_2$ surface. To obtain these configurations, the molecule was constrained into a specific position, and the system was subsequently optimized. The only exception to this procedure is geometry L (Linear), which was obtained by simply placing the molecule in the upper vacuum region.

Geometries BC and BB (Bidentate Carbonate and Bicarbonate) require a significant distortion of the initial $CO_2$ molecule, which from a physical standpoint may correspond to the presence of a potential energy barrier. Despite multiple optimization attempts, configurations MC and MB (Monodentate Carbonate and Bicarbonate) could not be stabilized, as they spontaneously converted to geometry L. A graphical representation of the relevant geometries is reported in Figure 5.e.2.

The stable L and BB geometries are of significant interest, as they represent $CO_2$ adsorption conditions that are more favourable than those occurring on the stoichiometric (101) anatase slab.

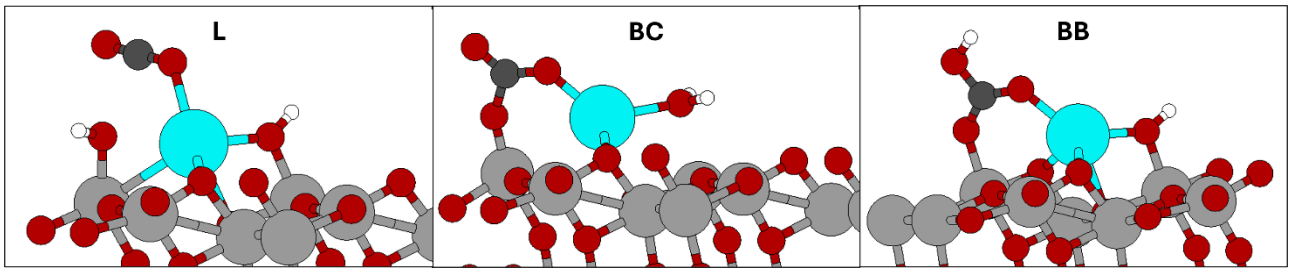



***Figure 5.e.2:*** *$CO_2$ adsorption geometries on (101) anatase + $Ca(OH)_2$*

Table 5.e.2 reports the vibrational frequencies of the relevant modes, with the Linear adsorption geometry over (101) anatase included for comparison. The frequencies of the OH stretching are omitted.

| Geometry | Eads (kJ/mol) | Vibrational frequencies (harmonic, cm-1) | Vibrational frequencies (harmonic+anharmonic, cm-1) |
|---|---|---|---|
| (101) anatase L | -18 | 2357, 1321 | 2327, 1335 |
| Ca(OH)2/(101) L | -28 | 2349, 1317 | 2323, 1325 |
| Ca(OH)2/(101) BC | +38 | 1731, 1615, 1196 | - |
| Ca(OH)2/(101) BB | -80 | 1613, 1377, 1207, 1018 | 1586, 1351, 1118, 1001 |

***Table 5.e.2:*** *Adsorption energies and vibrational frequencies of $CO_2$ adsorbed on stoichiometric and $Ca(OH)_2$-enriched (101) anatase surfaces, computed under the harmonic approximation and including the anharmonic correction. The BC configuration exhibits high total energy, placing it far from a global minimum. Consequently, the dynamics required to define the trajectory for the anharmonic correction calculation suffer from severe convergence issues, preventing its completion. However, the inability to calculate this correction remains minor information, given the intrinsic instability of the adsorption geometry.*

### Spectroscopic characterization

Based on the interesting results obtained via DFT calculations, $TiO_2$ samples were synthesized and characterized via Raman spectroscopy. This technique has proven to be a valid method to evaluate both the crystalline phase and potential adsorbates on the surface, although the calculated frequencies were in better agreement with features detected via FTIR spectroscopy. Figure 5.e.3 shows the spectra of the powders in the 100-1000 $cm^{-1}$ region, revealing that the synthesis procedure did not affect the crystal phase. Each spectrum in the figure represents the average of two spectra acquired at different spots on the sample.

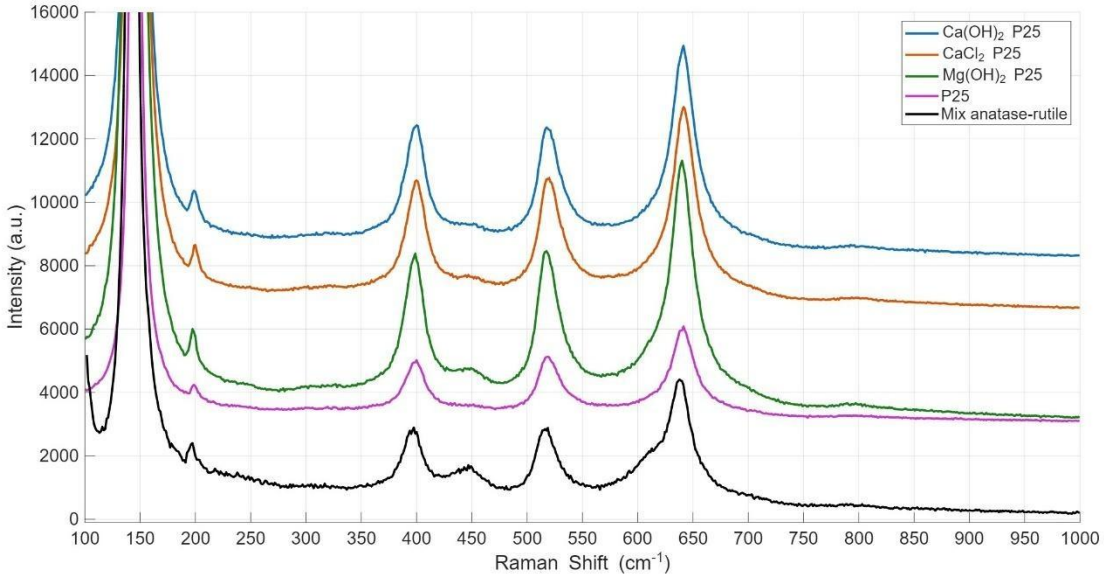



***Figure 5.e.3:*** *Raman spectra of pristine and ion-decorated Degussa P25 $TiO_2$ samples, recorded in the 100-1000 $cm^{-1}$ spectral region. Each spectrum represents the average of two independent replicates acquired at different spots on the sample.*

However, a significant modification regarding the rutile content was observed, characterized by the slight formation of a peak at approximately 450 $cm^{-1}$, which is indicative of a potential phase conversion. For comparison, the spectrum of a pristine P25 sample calcined at 600 °C for 6 hours is included in the same figure. A higher contribution from the rutile phase is particularly evident for the sample treated with $Mg(OH)_2$, whose spectrum also exhibits the potential formation of a shoulder close to the anatase peak at 640 $cm^{-1}$. In the other two synthesized samples, those prepared with $Ca(OH)_2$ and $CaCl_2$, the feature at 450 cm-1 is only weakly visible, while the other feature is obscured by the dominant anatase peak.

A theoretical hypothesis to describe this phenomenon could involve the synthesis conditions, which included an overnight thermal treatment at 90 °C that might have enabled a partial phase transition. This assumption could be supported by the fact that commercial P25 natively contains a small fraction of rutile, which could act as a seed for anatase conversion. However, it is widely reported in the literature that rutile formation at low temperatures strictly requires hydrothermal conditions and a low pH[6], [7]. This environment contrasts sharply with the conditions maintained during our synthesis, where the $Mg(OH)_2$ and $Ca(OH)_2$ solutions exhibited a pH of approximately 10, and the process was conducted under ambient atmosphere and pressure. Therefore, realistically, the thermal treatment did not promote any phase conversion.

Another possible explanation for the peak at 450 $cm^{-1}$ is related to the presence of $Mg(OH)_2$, as this compound shows a characteristic vibrational mode in the same region[8]. However, the absence of other peaks related to the hydroxide, combined with the moderately low concentration used and the subsequent washing procedure, makes this hypothesis less robust. In addition, a slight contribution from the rutile $E_g$ peak is also visible in the sample treated with $Ca(OH)_2$, which does not exhibit any relevant features in the highlighted spectral region.

Thus, the only possible explanation is that the phase transition did not occur because of the synthesis procedure; instead, sample inhomogeneity likely allows the detection of different rutile contributions depending on the selected spot. Figure 5.e.4 shows the two replicates used to calculate the mean reported in Figure 5.e.3, which are characterized by different rutile contents even within the same sample. This is particularly evident for the sample treated with $Mg(OH)_2$, which exhibits different rutile/anatase ratios depending on the measured spot. Another consideration that can be made is that the drying procedure after wet impregnation partially changes the morphology of the powder, which appears to form more coarse agglomerates. This may be due to the aggregation of powder nanofragments, which could make the mixture of anatase and rutile more apparent. Single measurable fragments in pristine P25 are statistically more likely to be pure anatase, and the spectra reported in Figure 5.e.4 appear to confirm this hypothesis.

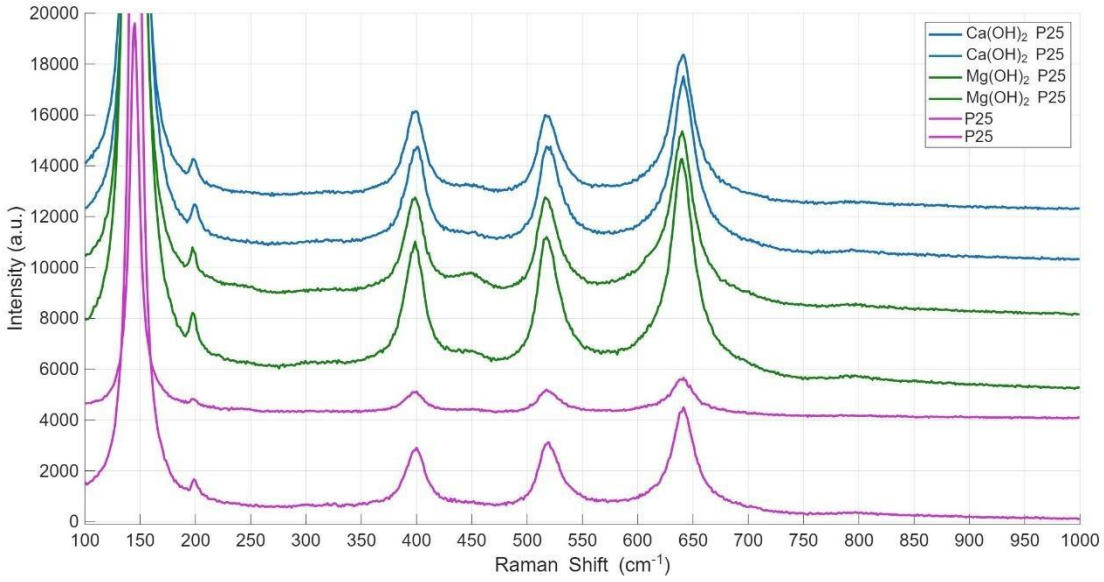



***Figure 5.e.4:*** *Raman spectra of pristine and ion-decorated Degussa P25 $TiO_2$ samples, recorded in the 100-1000 $cm^{-1}$ spectral region. Replicates are reported separately to highlight sample inhomogeneity.*

Raman spectroscopy was also employed to evaluate the presence of adsorbates. As the focus is the identification of carbonate structures that could suggest the adsorption of $CO_2$ according to the simulations, the measurements were conducted in the 1000-3500 $cm^{-1}$ spectral region. The exposure time was increased because the target molecules are expected to be present only on the surface of the powder; therefore, their low concentration might make detection impossible if the measurement is conducted over a shorter period.

The spectra acquired for the evaluation of potential carbon-containing adsorbates are reported in Figure 5.e.5; the baselines were intentionally not adjusted to highlight the differences in overall scattering. The baseline of the sample treated with $Ca(OH)_2$ appears comparable to those of pristine P25 and $Mg(OH)_2$-treated titanium dioxide, except for a variance in overall intensity. This difference can probably be attributed to a larger amount of powder present in the measured spots. Conversely, the spectrum of the $CaCl_2$-treated sample shows a stronger, broad band in the high-wavenumber region, hinting at the presence of residual water. This effect may be due to the high hygroscopicity of the salt, which tends to adsorb environmental moisture. For comparison, Figure 5.e.6 compares the spectrum of pristine P25 to that of a P25 sample hydrated with a drop of Milli-Q water and dried under ambient conditions immediately before measurement acquisition.

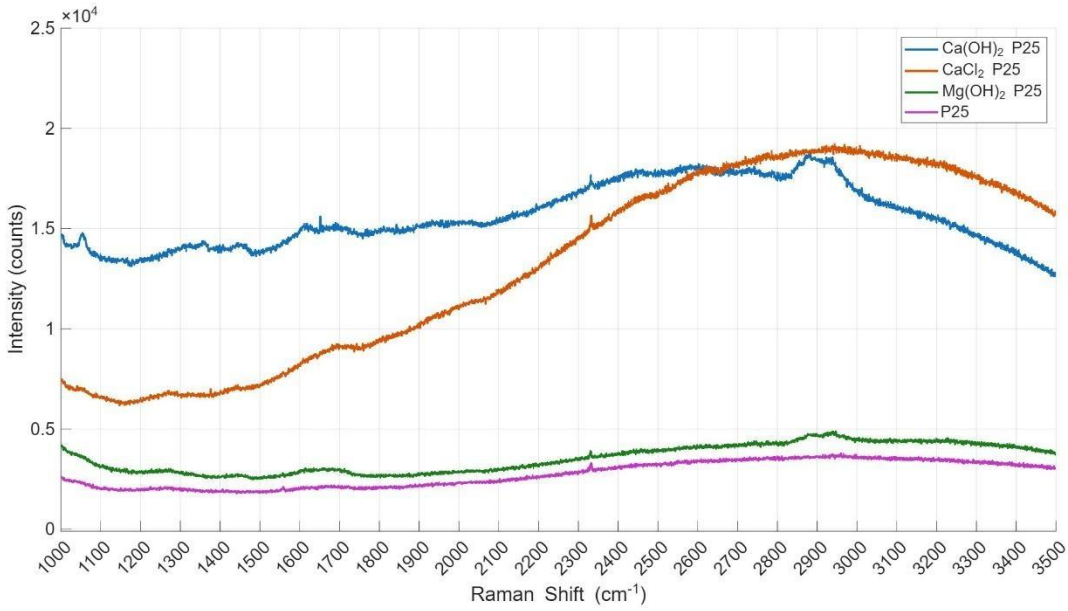



***Figure 5.e.5:*** *Raman spectra of pristine and ion-decorated Degussa P25 $TiO_2$ samples, recorded in the 1000-3500 $cm^{-1}$ spectral region. Each spectrum represents the average of two independent replicates acquired at different spots on the sample.*

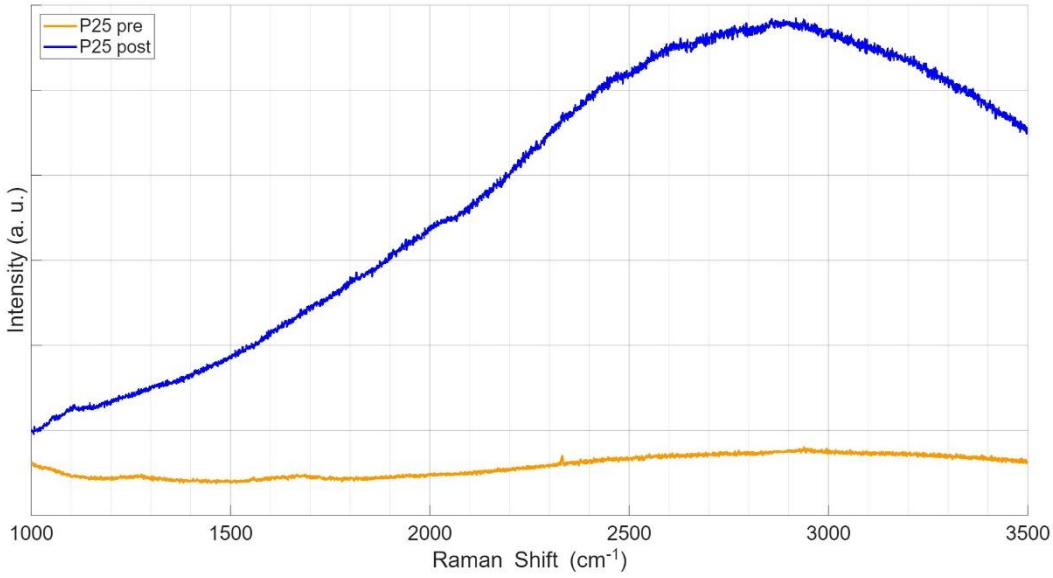



***Figure 5.e.6:*** *Raman spectra of Degussa P25 $TiO_2$ samples, recorded in the 1000-3500 $cm^{-1}$ spectral region. The sample was characterized in its pristine state and following the addition of a drop of Milli-Q water, which was subsequently dried under ambient conditions.*

All spectra exhibit a small feature at 2331 $cm^{-1}$, attributable to the presence of molecular nitrogen, and another at 1558 $cm^{-1}$ hardly identifiable derived from molecular oxygen[9], [10]. The detection of these two peaks is due to the long exposure time chosen for this type of measurement. Except for the systematic noise in the region below 1700 $cm^{-1}$, which may be caused by residual carbonaceous species, the synthesized samples show more defined features in this range. Notably, clear C-H stretching bands appear in the 2800-3000 $cm^{-1}$ region for the hydroxide-treated samples. While the presence of carbonates and bicarbonates is partially detectable, a baseline correction is required for a proper evaluation. Figure 5.e.7 shows the same spectra after the application of a baseline correction algorithm and a mild smoothing; this methodology is detailed in a dedicated chapter of the thesis.

Applying the baseline correction algorithm significantly improved peak identification. However, despite the smoothing procedure, noise still impacts spectral readability. Because this noise level is comparable to the absolute intensity of the spectra in Figure 5.e.5, the spectra of the two calcium-containing samples appear comparatively noisier. The spectral features identified in pristine P25 are also present in the treated samples, though they appear less resolved. While this could stem from a general reduction in intensity, the peaks for the $Mg(OH)_2$-treated sample remain remarkably intense. The baseline that can be estimated from Figure 5.e.5 confirms that this intensity cannot be attributed solely to differences in exposure time or in the size of the measured particle. Lastly, the signal between

1750 and 2800 $cm^{-1}$ can be ascribed to instrumental noise, as it does not affect the two samples that lacked a strong baseline. This is supported by the fact that this noise scales linearly with the baseline, remains sample-independent, and maintains an identical profile across all spectra, becoming particularly prominent in the two samples with high baselines.

In the region below 1700 $cm^{-1}$, excluding the bands at 1250 and 1650 $cm^{-1}$ and the oxygen-related features, peaks are exclusively observed in the synthesized samples. These signals are highly resolved in the $Ca(OH)_2$-treated sample, though they remain detectable as well in the other two[11]. The peak at 1053 $cm^{-1}$ is likely attributable to adsorbed bicarbonate species, given that bulk calcium carbonate typically exhibits its characteristic absorption around 1086 $cm^{-1}$. Conversely, this feature cannot be unambiguously confirmed for the $Mg(OH)_2$-treated sample; in this region, it appears merely as a shoulder, which is notably present in pristine P25 as well. Identifying the origin of the common peak at approximately 1440 $cm^{-1}$ remains challenging because its profile varies across the spectra, suggesting a convolution of multiple overlapping spectral features. Among these, $CH_2$ bending vibrations in the two hydroxide-treated samples could provide a plausible assignment for the shoulder observed at around 1465 $cm^{-1}$[12].

Interestingly, the two peaks at 1359 and 1610 $cm^{-1}$ appear to be exclusive to the $Ca(OH)_2$-treated sample. Several hypotheses were evaluated for their assignment, including the possibility that they correspond to the D and G bands of carbonaceous materials. Although their profiles deviate from typical D and G bands, this could be an effect of the specific experimental configuration, where thin layers of adsorbed species are measured rather than a bulk carbon phase. Alternatively, the peak at 1359 $cm^{-1}$ could be ascribed to methyl groups, a hypothesis supported by the presence of C-H stretching modes in the high-wavenumber region of the spectrum. The feature at 1610 $cm^{-1}$ might instead relate to C=C stretching; however, the absence of C-H stretching bands above 3000 $cm^{-1}$ weakens this assignment, even though the sp2 carbons could theoretically be fully substituted and lack hydrogen bonds. Lastly, these two peaks may be related to (bi)carbonate structures, as previously demonstrated in this thesis for the anatase (001) surface. This final explanation appears to be the most coherent, especially given the concurrent presence of bicarbonate structures confirmed by the peak at 1053 $cm^{-1}$. These assignments are based on standard vibrational frequencies compiled from literature manuals; however, they do not account for potential wavenumber shifts induced by structural distortions upon adsorption[12].

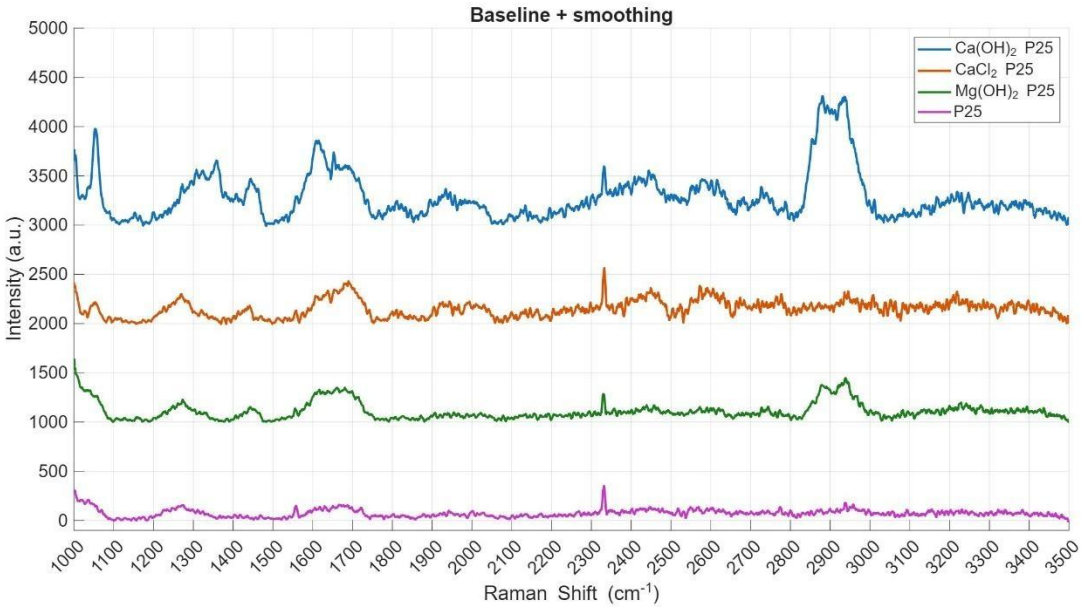



*Figure 5.e.7: Raman spectra of pristine and ion-decorated Degussa P25 TiO2 samples, recorded in the 1000-3500 $cm^{-1}$ spectral region. Each spectrum represents the average of two independent replicates acquired at different spots on the sample. Smoothing and baseline correction were applied to highlight spectral features*

The experimental Raman frequencies of the $Ca(OH)_2$ sample align well with the predicted values for adsorbed $CO_2$ structures in the form of Bidentate Bicarbonate. The partial shifts can be addressed by the computational method's limitations, which typically yields more accurate results for FTIR frequencies. Given the exploratory nature of this study, it cannot be ruled out that the actual adsorption geometries may deviate from the simulated models.

## Conclusions

To circumvent the synthetic and characterization challenges associated with anatase exposing a high percentage of reactive facets, a novel strategy was developed and thoroughly discussed in this chapter. This approach involved the modification of (101) anatase via wet impregnation with metal ions, a procedure that avoids both hydrothermal treatment and the use of hazardous reagents. Computational modelling was employed to complement the subsequent experimental analyses, although certain experimental conditions, particularly those arising from the aqueous solvent, could not be fully simulated.

The calculations revealed that the presence of the metal ion significantly alters the adsorption configurations of carbon dioxide over $TiO_2$. Consequently, certain geometric arrangements are hindered, while others become thermodynamically unstable. Nevertheless, two distinct stable geometries emerged as highly noteworthy. In the first configuration, $CO_2$ retains its Linear (L) molecular geometry. The adsorption energy calculated for this configuration on the ion-modified surface was lower than that reported for stoichiometric (101) anatase, indicating enhanced adsorption stability. The second configuration involves the formation of a Bidentate Bicarbonate (BB); although its adsorption energy for the single stable configuration identified was higher than that of the (001) anatase surface, it remains thermodynamically significant.

Subsequent characterization via Raman spectroscopy confirmed the presence of carbonate or bicarbonate species within the powder, likely originating from ambient or adsorbed $CO_2$. Consistent with the findings discussed in the (001) anatase section, DFT calculations exhibit minor systematic inaccuracies when predicting Raman frequencies compared to FTIR data. Nonetheless, DFT remains a powerful tool for identifying surface adsorbates. Notably, the experimental spectra also exhibited distinct C-H stretching modes, signalling the presence of organic contaminants. Their exact origin remains undetermined and warrants further investigation.

This chapter concludes the investigation into the adsorption properties of titanium dioxide. Given the promising results obtained from this exploratory study, further optimization and expanded investigations are highly recommended.

## References


[1] X. H. Yang, Z. Li, C. Sun, H. G. Yang, and C. Li, 'Hydrothermal Stability of {001} Faceted Anatase TiO2', *Chemistry of Materials*, vol. 23, no. 15, pp. 3486–3494, Aug. 2011, doi: 10.1021/CM2008768.

[2] C. Zhao, L. Ren, Y. Shi, X. Wang, W. Huang, and H. Xie, 'Advances and recent applications in high-energy {001} facets of anatase TiO2: A review', *J. Environ. Chem. Eng.*, vol. 13, no. 2, p. 115764, Apr. 2025, doi: 10.1016/J.JECE.2025.115764.

[3] X. Zhang, H. Ma, M. Zhang, and Y. Ma, 'Interfacial Charge-Transfer Excitons Help the Photoreduction of CO2 on TiO2', *ACS Catal.*, vol. 12, no. 18, pp. 11024–11035, Sep. 2022, doi: 10.1021/ACSCATAL.2C03795.

[4] J. G. Vitillo, 'Magnesium-based systems for carbon dioxide capture, storage and recycling: from leaves to synthetic nanostructured materials', *RSC Adv.*, vol. 5, no. 46, pp. 36192–36239, Apr. 2015, doi: 10.1039/C5RA02835C.

[5] C. Roth GmbH, 'Voluntary safety information following the Safety Data Sheet format according to Regulation (EC) No. 1907/2006 (REACH)', 2015.

[6] A.-E. Merrsews, 'The crystallization of anatase and rutile from amorphous titanium dioxide under hydrothermal conditions', *American Mineralogist*, vol. 61, p. 419424, 1976.

[7] M. Nag, P. Basak, and S. V. Manorama, 'Low-temperature hydrothermal synthesis of phase-pure rutile titania nanocrystals: Time temperature tuning of morphology and photocatalytic activity', *Mater. Res. Bull.*, vol. 42, no. 9, pp. 1691–1704, Sep. 2007, doi: 10.1016/J.MATERRESBULL.2006.11.032.

[8] T. Li and M. Ichimura, 'Fabrication of Transparent Mg(OH)2 Thin Films by Drop-Dry Deposition', *Materials 2021, Vol. 14, Page 724*, vol. 14, no. 4, p. 724, Feb. 2021, doi: 10.3390/MA14040724.

[9] J. Yamamoto and Y. Hagiwara, 'Precision evaluation of nitrogen isotope ratios by Raman spectrometry', *Analytical Science Advances*, vol. 3, no. 9–10, pp. 269–277, Oct. 2022, doi: 10.1002/ANSA.202200020.

[10] J. Thyr and T. Edvinsson, 'Evading the Illusions: Identification of False Peaks in Micro-Raman Spectroscopy and Guidelines for Scientific Best Practice', *Angew. Chem. Int. Ed.*, vol. 62, no. 43, p. e202219047, Oct. 2023, doi: 10.1002/ANIE.202219047;PAGE:STRING:ARTICLE/CHAPTER.

[11] S. Barroso-Solares, I. Mediavilla-Martinez, C. Sanz-Velasco, A. C. Prieto, and J. Pinto, 'Pigments identification and analysis of the state of conservation of the decorative elements of the castle of Coca (XV-XVI AC, Segovia, Spain) by Raman Spectroscopy', *J. Phys. Conf. Ser.*, vol. 2204, no. 1, p. 012010, Apr. 2022, doi: 10.1088/1742-6596/2204/1/012010.

[12] G. Socrates, 'Infrared and Raman characteristic group frequencies : tables and charts', 2001.

# 6. Other projects

## 6.a The reaction of refrigerant gases investigated via DFT and vibrational spectroscopy

*This chapter provides a general outline of a draft paper that was accepted for publication in the International Journal of Refrigeration. Given the hybrid engineering-chemical approach, the thermodynamical experimental characterization will not be included in this section of the thesis. Since this work is still under peer review, a general improvement of the concepts here reported may be expected. The title of the submitted manuscript is "Experimental and DFT Investigation of Reactivity in the Near-Azeotropic R1233zd(E)/R1336mzz(E) Mixture".*

*Several authors contributed to this study in different roles. Thus, sincere thanks are extended to Michele Doninelli, Gioele Di Marcoberardino, and Ivano Alessandri.*

### Abstract

Halogenated olefins and their mixtures are considered promising low-GWP working fluids for organic Rankine cycles and high-temperature heat pumps. However, as unsaturated compounds, they present chemical stability issues that risk eluding traditional analytical methodologies. For this reason, alongside the conventional, purely physical-thermodynamic study, a chemistry-oriented approach was undertaken to estimate the reactivity of a binary refrigerant mixture.

This was achieved through the application of Density Functional Theory to evaluate which condition was thermodynamically most favourable, by hypothesizing potential reaction pathways. Among the investigated pathways, one led to products characterized by a significantly lower total energy compared to the others. Following experimental tests conducted by increasing the pressure and temperature of the refrigerant gas mixture, the clear formation of a dark yellowish-brown oily compound was observed, accompanied by the presence of microscopic solid particles. Infrared and Raman spectroscopic analyses performed on both the liquid and solid phases of the obtained product led to the identification of several key functional groups consistent with the theorized reaction products.

Consequently, the structure of the reaction product would appear as a branched carbon chain containing hydrogen atoms, chlorine atoms, and -$CF_3$ groups. Furthermore, the feature associated with C=C double bonds, typically visible via vibrational spectroscopy, is scarcely detectable. This is

consistent with carbon saturation, which represents a cornerstone factor of the reaction pathway investigated through DFT.

## Introduction

The use of refrigerant gases with attractive thermodynamic performance is often limited by the severe environmental impact they can entail. Indeed, many of them possess a high GWP (Global Warming Potential), thus presenting significant environmental risks that lead to strict regulations on their use[1]. Given this premise, research focuses on identifying fluids that maintain optimal performance when subjected to high temperatures and pressures, while simultaneously posing no threat to the atmosphere, or at least ensuring that the impact of their dispersion is limited. The origins of the atmospheric release of such gases remain a highly interesting point, which is, however, beyond the scope of this discussion.

Considering the most current regulations, two gases are widely used in this field: R1233zd ($CF_3$-CH=CCIH) and R1336mzz (($CF_3CH=CHCF_3$)[2], [3]. Without going into detail regarding their thermodynamic characteristics of interest, it is worth mentioning that they are considerably stable under real working conditions, which are often characterized by medium-to-high temperatures (> 100°C) and pressures around tens of bars.

Given the geometry of the two molecules, both can exist in either the *Z* (*cis*) or *E* (*trans*) form. As demonstrated below, the *trans* configuration is the more stable of the two, likely due to lower steric hindrance. Nevertheless, both configurations are commercially relevant. This could raise an initial red flag since, in the absence of targeted characterizations, it is not possible to determine whether the gas maintains its original characteristics during operation or if it tends to isomerize toward a more stable configuration.

This issue is not limited to cis-to-trans conversion but, more generally, could include the degradation of the molecule into more stable by-products. As is often the case, these are not fully documented and could therefore pose environmental and health hazards. Furthermore, the thermodynamic performance could be compromised, resulting in a limited lifespan for the refrigerant fluid. Consequently, it would require periodic replacement, leading to increased costs and, if the replacement process is not carried out correctly, potential environmental damage.

Nevertheless, given the presumed relative stability of the two gases examined in this work, it is worth highlighting the existence of a patent related to the use of a binary mixture of R1336mzz(Z)/R1233zd(E), in which the less stable (*cis*) configuration of one of the two gases was preferred[4]. The hypothesis upon which the patent is based is that the mixture of the two fluids would achieve an optimal compromise in terms of thermodynamic performance compared to the use of the single, pure gas.

Based on several experimental tests conducted on the R1233zd(E)/R1336mzz(E) mixture, critical issues were observed, likely resulting from a potential reaction between the two gases. To this end, alongside systematically performed thermodynamic tests, a chemical characterization was evaluated to investigate which reaction products could form. This was achieved by combining a computational and experimental approach, which aims to highlight the limitations of conventional thermodynamic tests, as they often overlook the possibility of molecular reactions.

DFT proved to be a fundamental tool both for demonstrating the stability of the *trans* configuration over the *cis* form, and for identifying potential reaction pathways that can occur once enough energy is supplied to the system. On the other hand, vibrational spectroscopy provided outstanding contributions to the characterization of the reaction products, showing a high level of agreement with the molecular structures predicted by the simulations.

## Density Functional Theory simulations

As mentioned in the introduction, the potential linked to the use of the binary mixture as a refrigerant fluid could be severely limited by the possible reaction between the two. For this reason, the use of Density Functional Theory (DFT) was evaluated to gain a general understanding of which reaction products could be more likely given their chemical stability.

Plane-wave Density Functional Theory simulations were conducted using Quantum Espresso[5], [6]. All of them were performed within the generalized gradient approximation (GGA) using the Perdew–Burke–Ernzerhof (PBE) functional and norm-conserving pseudopotentials[7], [8]. Convergence tests were performed to establish the most convenient cut off energy for plane wave basis set and k-points number, respectively 80 Ry and Γ-point were chosen. A cubic supercell with side of 24 Å was employed to avoid mirror interactions, notably resulting in a weak attraction between molecules in smaller cells. The investigation of the possible reaction pathways was conducted by comparing the total energy of

different molecules that were hypothesized to assess their relative stability and, consequently, the possibility of their formation. A detailed description of the reaction dynamics was considered critical because of the possible presence of radical species and was partially beyond the scope of the present work[9]. Consequently, energy barriers cannot be identified within this framework.

Simulations of a single gas molecule of R1233zd revealed the higher stability of R1233zd(E) respect to R1233zd(Z) as the computed total energy was 11 kJ/mol lower in the first case. The same situation was verified for R1336mzz(E) over R1336mzz(Z), as the energy was 23 kJ/mol lower in the first. This demonstrates the higher stability of the trans compared to the cis isomer in both cases, addressable to Coulomb forces between hydrogen, chlorine and fluorine atoms because of their partial charge. Similar conclusions were derived in the study of Tao et al.[10]. This suggests a possible cis-to-trans conversion when the working conditions includes sufficiently high temperature and pressure, conditions needed to overcome eventual energy barriers. In this regard, the findings of this research could also be extended to the binary system R1336mzz(Z)/R1233zd(E), which has been proposed as a refrigerant blend in a patent filed by Trane, since R1336mzz(Z) is expected to partially convert into R1336mzz(E) during the plant's lifetime[4].

The mixture was simulated including a molecule for both gases in their trans configuration, as calculated to be more stable than the other. Possible products deriving from their reaction were also evaluated, identifying different possible bond breakings and a consequent rearrangement of atoms.

In the first condition that was explored, C-Cl bond from R1233zd and one C-H bond from R1336mzz are assumed to break, with the formation of hydrochloric acid and the bonding between the two residuals from the molecules through a C-C bond between the two atoms which lost the bonds.

As illustrated in Figure 6.a.1-products a, b, the first two reaction schemes represent consecutive steps of the same reaction mechanism, initiated by the cleavage of a C–H bond and followed by the attack of the generated intermediate on a C=C bond of another R1233zd(E) molecule. Both reactions (involving the breaking of C-H bond) are thermodynamically favourable, with the product energies being 14 and 13 kJ $mol^{-1}$ lower than those of the reactants, respectively. These two steps collectively illustrate a plausible chain-growth mechanism through which larger, polymer-like organic species can form from the initial refrigerant molecules.

The third scheme (Figure 6.a.1-product c), on the other hand, depicts a hypothetical pathway involving the detachment of a $–CF_3$ group from R1336mzz, following a similar reaction principle.

However, this reaction is thermodynamically unfavourable, as the calculated product energy is about 5 kJ $mol^{-1}$ higher than that of the reactants, indicating that it is not expected to occur.

The first scheme reported in Figure 6.a.1 was expanded to assess the possible saturation of the C=C bonds. The chlorine atom was assumed to bind to one of the four carbon atoms characterized by $sp^2$ hybridization. The remaining hydrogen atom was consequently placed. Thus, four possible schemes were investigated, with calculated ΔE values ranging from-55 to-62 kJ/mol. The energy difference was calculated with respect to the refrigerant gas mixture. Figure 6.a.1 product d shows the most stable configuration, with the C-Cl on the fifth carbon atom, assuming the chain begins at the top left. ΔE does not differ from that calculated for the configuration with C-Cl bond on the third carbon atom, while both cases with chlorine on second and fourth carbon atoms exhibit higher energies (-55 kJ/mol).

According to these results, the formation of long and branched organic molecules can be expected, characterized by the presence of single carbon bonds, with a considerable presence of-$CF_3$ groups and possibly C-H and C-Cl bonds. The presence of remaining C=C bonds may be detected in the products, and it may be inversely correlated with the molecular mass.

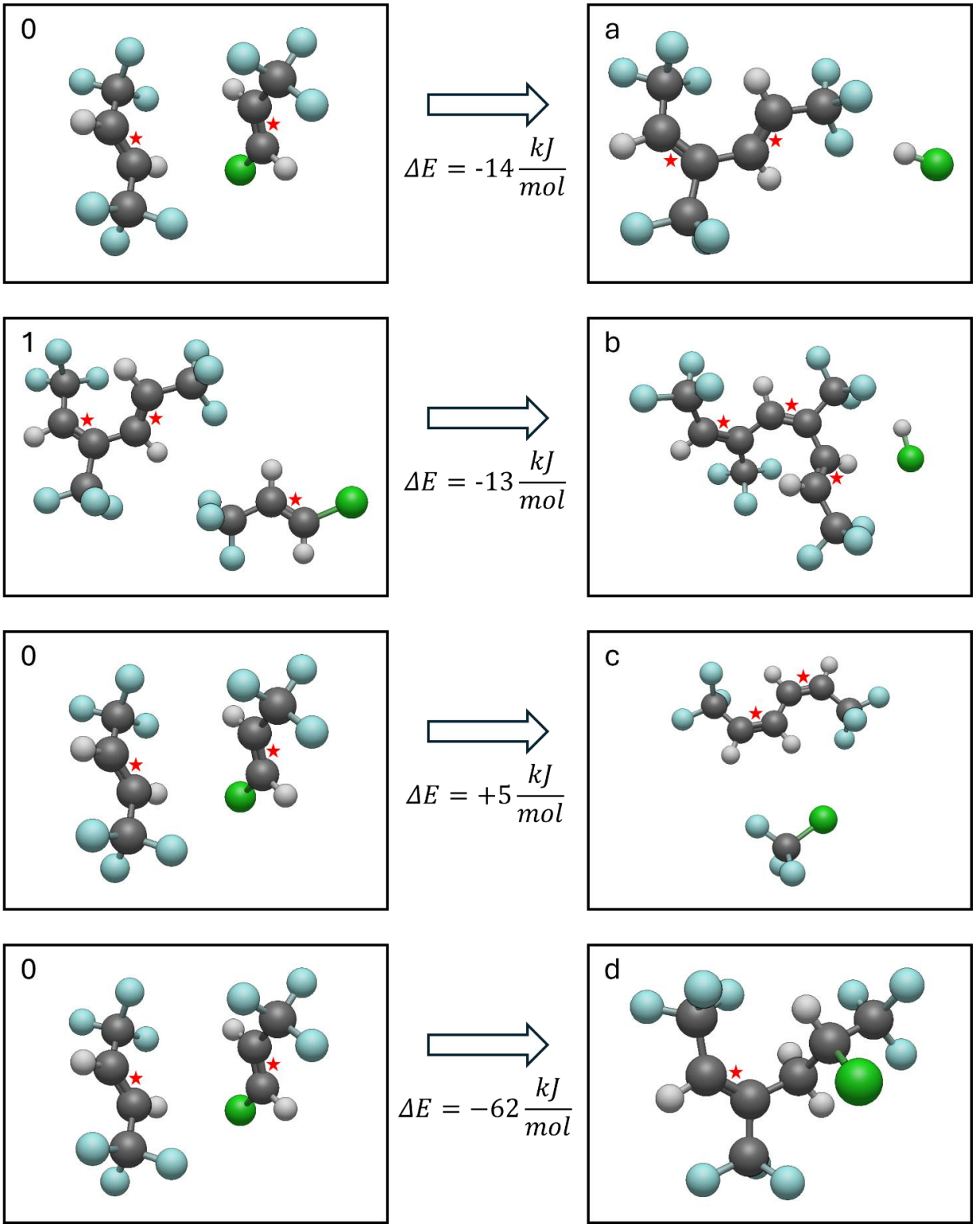



***Figure 6.a.1:*** *Representations of the investigated reaction mechanisms involving R1233zd(E) ((E)$CF_3$-CH=CClH) and R1336mzz(E) ((E)$CF_3CH=CHCF_3$). Configurations a and b correspond to consecutive steps of a reaction mechanism leading to chain growth between the eventual byproduct and R1233zd(E). Scheme c represents a hypothetical –$CF_3$ detachment reaction, which was found to be thermodynamically unfavourable (ΔE > 0). Scheme d is representative for reactions involving the loss of one double bond. Double bonds are highlighted with red stars. grey ➔ carbon, white ➔ hydrogen, green ➔ chlorine, light blue ➔ fluorine. E = Eproducts - Ereagents.*

## Spectroscopic characterization

After a thermal treatment at 110 °C for one week, carried out to reproduce realistic working conditions for the fluid, the formation of an oily liquid product with a partial presence of dark solid particles was observed. The liquid phase of the product was characterized by μ-Raman and Attenuated Total Reflection Fourier Transform InfraRed (ATR-FTIR) spectroscopies, while the structure of the black solid particles was investigated exclusively by Raman spectroscopy due to the need for microscopic focusing on individual particles. Spectra are reported in Figure 6.a.2.

Raman spectra were recorded using a Horiba LabRAM HR spectrometer equipped with a He–Ne laser (λ = 633 nm). For the liquid sample, the exposition time was set to 20 seconds, and the spectral window of 100-4000 $cm^{-1}$ was considered. For the solid particle, the acquisition time was set accordingly to the signal scattered by the spot, with a shorter exposition time (10/30 s) for the extended spectral window (100-3500 $cm^{-1}$) and a longer one (30/60 s) for the region 100-1000 $cm^{-1}$. Both for liquid and solid samples, two spots ($z_1$, $z_2$) were measured.

FTIR measurements were conducted using a Nicolet™ Summit™ FTIR Spectrometer equipped with Everest™ Diamond ATR, which allows for direct analysis of liquid samples. Reported spectrum represents the average of 16 measurements, collected in a single measurement of around 10 s.

Dark solid particles of the obtained material (Figure 6.a.2) were collected by washing the test cylinder with dimethyl sulfoxide (DMSO) and isolating it from the solvent by centrifugation. Two regions of the sample ($z_1$ and $z_2$) were measured in the 100–3500 $cm^{-1}$ range, followed by a second measurement in the 100–1000 $cm^{-1}$ region with a longer acquisition time. Due to the lower signal intensity observed for $z_2$, the acquisition time was increased compared to $z_1$.

Measurements on liquid samples allowed to access to precious confirmation of the theorized model. Spectra collected via FTIR and Raman spectroscopy showed almost completely the same features, with the differences addressable to the selection rule for vibrational spectroscopy. A slight shift of 5/10 $cm^{-1}$ can be observed comparing the two spectra, although this does not drastically affect the analysis.

FTIR and Raman spectra showed contributions from CH stretching in the region 2850-3000 $cm^{-1}$. Three peaks present in Raman spectra are directly findable also in FTIR, while FTIR shows a fourth feature at 2896 $cm^{-1}$. CH2 bending mode in alkanes is commonly found in the region 1480-1440 $cm^{-1}$, thus this could be the origin for the peak at 1460 $cm^{-1}$. Other modes referrable to CH bending and

$CF_3$ stretching may be found in the region 1200-1500 $cm^{-1}$, while features at lower wavenumbers up to 1000 $cm^{-1}$ are usually addressed to skeletal vibrations of carbon chains. In this region, the contribute of $CF_3$ may be present, mainly in the FTIR spectrum due to the strong polarity of the functional group.

Oxygen presence was not covered by the simulations, as the reactor was supposed to contain just the mixture of the two refrigerant gases. From the FTIR spectra, OH band is slightly visible at 3500 $cm^{-1}$; thus, this could be due to oxidation after exposure to environmental oxygen. This could have happened during the degassing phase, as the temperature of the fluid was higher than the environmental. High temperature facilitates the oxidation or even the autoignition of many oils, and, for this reason, this could be addressed as the origin of the oxygen presence. Oxygen is also detectable because of a slight contribution of carbonyl detectable at 1700-1750 $cm^{-1}$. FTIR spectrum is characterized by two peaks: the one at 1724 $cm^{-1}$ derives from residues of acetone, while the other at 1744 $cm^{-1}$ may be a C=O located in the obtained carbonaceous material. Moreover, the feature in FTIR spectrum at 1012 $cm^{-1}$ may be originated by vibrations of a secondary alcohol. Its absence in Raman spectrum could be due to polarity related to carbon-oxygen bonds.

The doublet observable in Raman spectra at 1588 and 1616 $cm^{-1}$ is indicative of conjugated C=C. Its low intensity is completely compatible with the results of simulations which predicted a stable structure distinguished by this characteristic. This was not the most stable structure, which might explain why its spectral features do not present strong intensity.

Peaks at wavenumbers lower than 1000 $cm^{-1}$ are compatible with halogen-carbon, while other peaks may present different origins, such as $CH_2$ twisting or CCO stretching in alcohols. Raman spectra are affected by not negligible noise and low intensity features probably addressable as artifacts. Origin for these may be the variation of optical focus due to long-term measurements on a liquid sample.

The Raman spectrum of the analysed dark particle shows the characteristic features of a carbon-based material, with two main bands at approximately 1330 and 1580 $cm^{-1}$, corresponding to the D and G bands, respectively[11]. The D band is only slightly less intense than the G band, indicating a relatively high level of structural disorder and therefore a low degree of crystallinity. Consistently, the absence of the sharp G band expected near 2700 $cm^{-1}$ further confirms that the material is not graphitic. This is in line with the fact that well-crystallised graphite generally forms only under temperatures and pressures higher than those employed in our experiments. Increasing the exposure time allows the detection of more peaks in the window 100-1000 cm-1. The peaks at approximately

290 and 680 $cm^{-1}$ are observed only in one spot (z1) and can be assigned to deformation and stretching modes of the C–Cl bond, respectively. The features at around 420 and 770 $cm^{-1}$ are observed in both spots and may be attributed to vibrations of-$CF_3$ group, which could be the origin of the other peaks observed in the region 500-900 $cm^{-1}$[12].

Peaks observable in Raman spectra of liquid sample at around 1600 $cm^{-1}$ cannot be detected in the spectra of the solid sample. This may be due either to their being overlapped by a nearby intense band or to their actual absence in the final product. The latter explanation appears more plausible, since the combination of high temperature and pressure could promote radical formation and, consequently, saturation of the double bond. This also finds confirmation in the fact that most solid content was found after prolonged treatment.

Solid dark particles appear to be more heterogeneous than the liquid, as can be deducible from a comparison of spectra. This may be explained by the fact liquid samples are more chaotic than solid ones, thus inhomogeneities in the sample have a statistically less influence on the measurement performed with a micro-Raman spectrometer.

Raman spectra of the solid dark particle showed more heterogeneity than measurements on the liquid sample, which could be described by different carbon chain lengths (implicating a different chlorine/fluorine ratio) obtained during the treatment.

In addition to the spectroscopic characterization reported herein, further quantitative and qualitative analyses would be of great interest. Since the contents of this chapter represent a preliminary section subject to future revisions, it should be noted that additional evaluations have been incorporated into the final text of the scientific article currently undergoing publication. Among these, particular attention was dedicated to estimating the reaction yield between the two gases, determined through weight measurements taken before and after thermal treatment.

However, certain FTIR characterizations of potential interest could not be performed due to experimental difficulties. Specifically, the FTIR analysis of the black solid particulate formed during the reaction was hindered by two main factors: the scarcity of the sample and the extremely small size of the particles, which significantly complicated their separation from the liquid product. Furthermore, even if a suitable isolation strategy were identified, the currently unresolved nature of these reaction products and their potential to interact with the contact surfaces during ATR-FTIR measurements would still need to be addressed.

Prior to analysing the liquid sample, preliminary tests were conducted to evaluate its solubility in acetone, as any persistent residue on the ATR crystal could irreversibly damage the device. Due to the previously mentioned difficulties in sampling the solid material, exhaustive solubility tests could not be performed on it; for this reason, ATR-FTIR measurements on the solid particles were avoided. Nevertheless, despite similar concerns regarding support contamination, a micro-FTIR measurement could have overcome the limitation of requiring direct contact between the sample and the instrument optics.

For future investigations, a micro-FTIR configuration could be considered. This setup restricts the risk of damage to the sample substrates, which are relatively inexpensive compared to the higher financial risk associated with damaging the ATR crystal. In the work reported here, this analysis was not performed due to a temporary instrument breakdown.

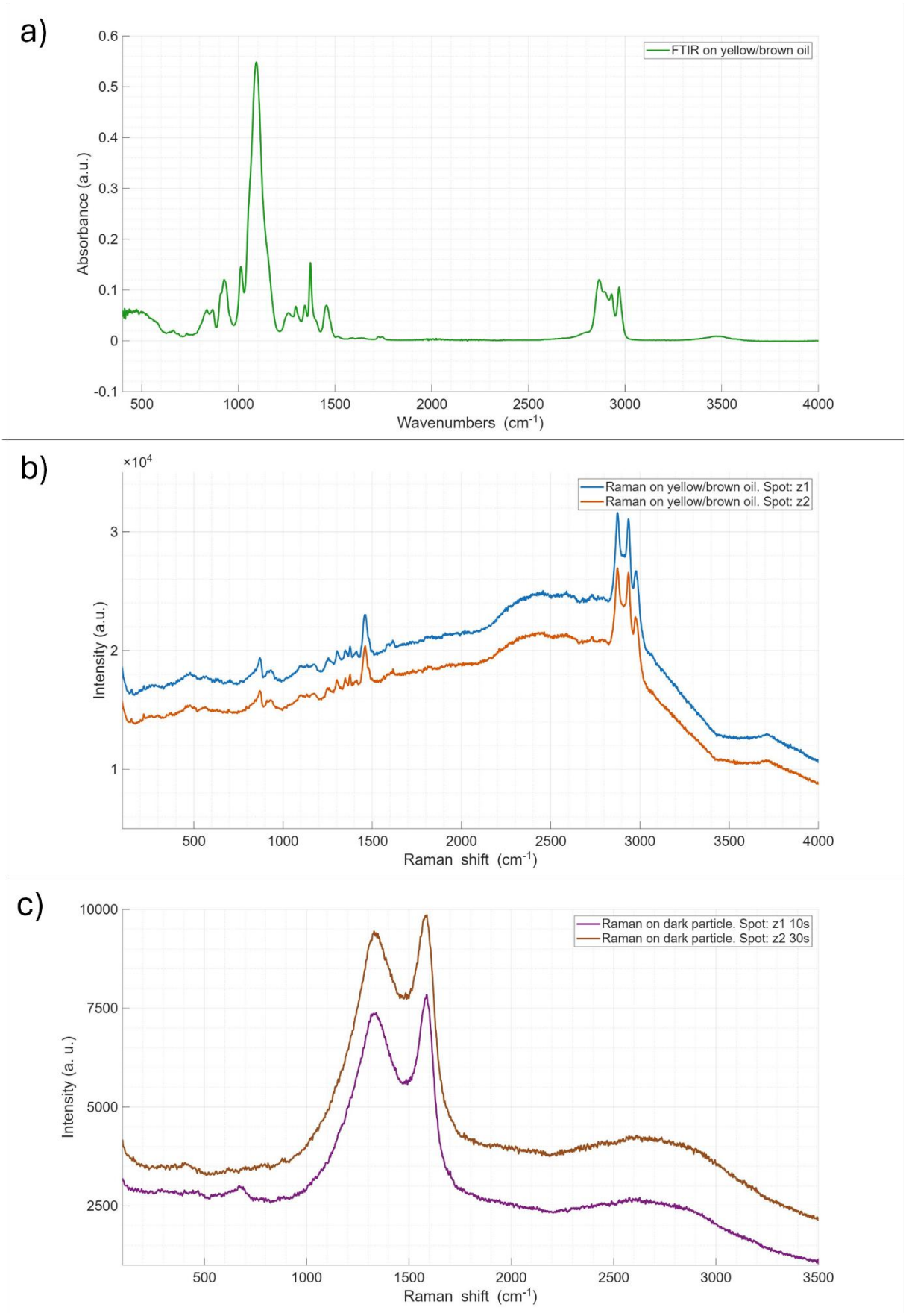



*Figure 6.a.2: a) FTIR and b-c) Raman spectra of liquid and solid reaction products.*

## Conclusions

This brief discussion aimed to summarize the relevant points of a broader study within the context of this thesis. The novel element is the chemical approach, combined with conventional thermodynamic tests. In this way, it was possible to investigate certain properties of a refrigerant fluid that would have otherwise remained unexplored, given that they depended on the reaction between the two gases composing the mixture.

Thanks to this methodology, it was possible to demonstrate the thermodynamic stability of the trans isomers of the two refrigerant gases composing the tested binary mixture over their cis counterparts. This is a relevant detail, as it can be significant even when simply investigating the behaviour of a single gas when subjected to thermodynamic conditions different from the original ones by means of a controlled temperature increase, which also influences the pressure.

After experimenting with a mixture of the two gases, R1233zd(E) ((E)$CF_3$-CH=CCIH) and R1336mzz(E) ((E)$CF_3CH=CHCF_3$), at medium-to-high temperatures, the formation of an oily product also characterized by the presence of solid particles suggested that the two molecules might have reacted. For this reason, a DFT-based study was conducted to evaluate which reaction pathway was most favourable, assuming that an adequate amount of energy was supplied to the system. The findings revealed that the two molecules could iteratively associate, forming a branched carbon chain in which the presence of double bonds was progressively reduced following the attachment of further molecules.

FTIR and Raman spectroscopies allowed for the characterization of the reaction products, showing a good level of agreement with the simulation predictions. A limited presence of C=C bonds was observed, which is consistent with what was predicted. Many features in the spectra could be associated with the presence of C-H bonds and halogenated groups, in line with the simulations.

For these reasons, the power of combining a computational and experimental chemical approach with classic thermodynamic tests was successfully demonstrated. This operational methodology could be extended to further investigations on the mixture under study and could also be of interest for other analogous contexts.

## References


[1] B. O. Bolaji, 'Theoretical assessment of new low global warming potential refrigerant mixtures as eco-friendly alternatives in domestic refrigeration systems', *Sci. Afr.*, vol. 10, p. e00632, Nov. 2020, doi: 10.1016/J.SCIAF.2020.E00632.

[2] N. Mattiuzzo, A. Berto, M. Azzolin, and D. Del Col, 'Experimental analysis and modelling of R1233zd(E) condensation heat transfer and pressure drop in small diameter channels', *Thermal Science and Engineering Progress*, vol. 62, p. 103586, Jun. 2025, doi: 10.1016/J.TSEP.2025.103586.

[3] M. Khan, J. Wen, M. A. Shakoori, and Y. Liu, 'Condensation and thermophysical properties of R1336mzz(Z) through molecular dynamics simulations', *International Journal of Refrigeration*, vol. 146, pp. 290–299, Feb. 2023, doi: 10.1016/J.IJREFRIG.2022.11.008.

[4] Schultz, 'Refrigerant compositions', Apr. 2016.

[5] P. Giannozzi *et al.*, 'Advanced capabilities for materials modelling with Quantum ESPRESSO', *Journal of Physics Condensed Matter*, vol. 29, no. 46, Sep. 2017, doi: 10.1088/1361-648X/aa8f79.

[6] P. Giannozzi *et al.*, 'Quantum ESPRESSO: a modular and open-source software project for quantum simulations of materials', *Journal of Physics Condensed Matter*, vol. 21, no. 39, Jul. 2009, doi: 10.1088/0953-8984/21/39/395502.

[7] D. R. Hamann, 'Optimized norm-conserving Vanderbilt pseudopotentials', *Phys. Rev. B*, vol. 88, no. 8, p. 085117, Aug. 2013, doi: 10.1103/PhysRevB.88.085117.

[8] D. R. Hamann, M. Schlüter, and C. Chiang, 'Norm-Conserving Pseudopotentials', *Phys. Rev. Lett.*, vol. 43, no. 20, p. 1494, Nov. 1979, doi: 10.1103/PhysRevLett.43.1494.

[9] C. Adamo and V. Barone, 'Accurate excitation energies from time-dependent density functional theory: assessing the PBE0 model for organic free radicals', *Chem. Phys. Lett.*, vol. 314, no. 1–2, pp. 152–157, Nov. 1999, doi: 10.1016/S0009-2614(99)01113-6.

[10] N. Tao, C. Liu, H. Xing, S. Lu, S. Lo, and H. Zhang, 'Experimental and Density Functional Theory Studies on 1,1,1,4,4,4-Hexafluoro-2-Butene Pyrolysis', *Molecules 2020, Vol. 25, Page 3799*, vol. 25, no. 17, p. 3799, Aug. 2020, doi: 10.3390/MOLECULES25173799.

[11] A. Dychalska, P. Popielarski, W. Frank´owfrank´ Frank´ow, K. Fabisiak, K. Paprocki, and M. Szybowicz, 'Study of CVD diamond layers with amorphous carbon admixture by Raman scattering spectroscopy', *Materials Science-Poland*, vol. 33, no. 4, pp. 799–805, 2015, doi: 10.1515/msp-2015-0067.

[12] G. Socrates, 'Infrared and Raman characteristic group frequencies : tables and charts', 2001.

# 6.b DFT study on the interaction between histamine and polydopamine

*This chapter takes inspiration from the work carried out regarding the article Boontanom A. et al., Poly(dopamine)-coated $TiO_2/SiO_2$ resonators for the non-plasmonic SERS detection of organic analytes, Applied Surface Science (2026). The corresponding author has been informed that part of the material will be reused here and has provided her approval for the drafting of this section of the thesis.*


## Abstract

The T-Rex resonators exploit the optical phenomenon of total internal reflection to trap and magnify the Raman signal originating from molecules adsorbed on their surface. This facilitates the clear identification of spectral features associated with the vibrational modes of the analyte, whose intensity may be extremely low when concentration is below the limit of detection. T-Rex resonators consist of micrometric silica spheres coated with a nanometric layer of titanium dioxide deposited via Atomic Layer Deposition (ALD). Recently, surface modification of these resonators was evaluated by introducing a polydopamine (PDA) layer to enable the selective adsorption of specific chemical species. Raman characterization confirmed that the fabricated sensors successfully lowered the detection limit for two target molecules, methylene blue and histamine, reaching remarkably low concentrations. To identify the chemical mechanisms governing this adsorption process, Density Functional Theory (DFT) simulations were performed to investigate the interaction between PDA and histamine. The computational results revealed a significant contribution from hydrogen bonding, which likely drives this adsorption phenomenon.


## Introduction

The term T-Rex refers to Raman resonators consisting of silica microspheres coated with titanium dioxide grown via Atomic Layer Deposition (ALD) and subsequently annealed to anatase[1]. Their operating principle relies on the refractive index contrast between the two materials, which enables the confinement of radiation within the titania layer. Consequently, by optimizing the coating thickness, constructive interference can be achieved. This allows to magnify the signal originating from chemical compounds adsorbed on the surface of the sphere.

These resonators have been effectively employed for the detection of ambient carbon dioxide via Raman spectroscopy[2]. It is well known that $CO_2$ exhibits an almost negligible Raman signal, in contrast to its infrared contribution, which is often treated as background noise and removed through baseline subtraction. Electromagnetic field simulations, coupled with remarkable experimental results, demonstrated a direct dependence between the TiO2 coating thickness and the signal intensity due to constructive interference, specifically affecting the Fermi dyads that arise from the coupling between the symmetric stretching and bending modes of $CO_2$[2].

However, what has recently generated remarkable interest is the possibility of introducing an additional coating on top of the $TiO_2$ layer to selectively improve the adsorption of specific chemical species[3]. This approach combines the resonating mechanism of the spheres with an increased concentration of target molecules on the T-Rex surface. The case study analysed herein involved the use of polydopamine (PDA) as an outer coating to enhance the adsorption of pollutant molecules. Among various alternatives, methylene blue and histamine were chosen as target analytes, based on the hypothesis that the presence of aromatic rings in both the polymer and the molecules could generate π-π interactions capable of coordinating the pollutant onto the surface.

In the case study presented in the published work, silica microspheres (radius = 1 μm) were coated with a 100 nm layer of titanium dioxide via ALD and subsequently subjected to thermal treatment 715 °C for 4 h to obtain the anatase crystalline phase. Afterward, they were coated with a 15 nm layer of polydopamine (PDA).

Raman measurements under these conditions confirmed the increase in signal intensity, enabling correct identification of the molecule's spectrum even at low concentrations. In the case of methylene blue (MB), its detection limit is known to be on the order of $10^{-3}$ M in the absence of specific resonators. Using bare T-Rex substrates (without PDA coating), it is possible to lower this limit by an order of magnitude, leading to an effective recognition of MB even when the concentration does not exceed $10^{-4}$ M. With the PDA–T-Rex system, the value is further decreased to $10^{-6}$ M. Similarly, for histamine, the introduction of PDA on the T-Rex surface lowered the detection limit from $10^{-7}$ M to $10^{-8}$ M, thus improving it by an order of magnitude in this case as well. Generally, sensing performances of this order of magnitude achieved via SERS are considered excellent results[4].

Given these purely experimental premises, a computational approach was pursued to investigate the interaction between the histamine molecule and the investigated surfaces, namely $TiO_2$ and PDA. The primary challenges stem from the difficulty in predicting the correct relative arrangement of the

monomers constituting the PDA, which necessitated multiple trials with different polymer chain configurations. The results appear to converge on the pivotal role of hydrogen bonds between the molecule and the surface in dictating the interaction. Consequently, the adsorption energy was calculated, demonstrating that the interaction between the molecule and the PDA is more stable compared to the bare titania surface, hereby considered a reference of an uncoated T-Rex resonator.

## Materials and methods

T-Rex preparation and the subsequent polydopamine (PDA) coating are detailed within the published work; however, these experimental procedures are beyond the scope of the present chapter[3].

All Density Functional Theory (DFT) simulations in this study were performed using the Quantum Espresso package. The periodic nature of plane-waves (PW) was exploited to model infinite replicas of single or grouped monomers[5], [6], [7]. To achieve an optimal balance between computational cost and accuracy, the Perdew-Burke-Ernzerhof (PBE) functional within the Generalized Gradient Approximation (GGA) was selected[8].

Convergence tests involved optimizing atomic positions along the x-direction on a cell containing a single monomer (the bonding axis between fundamental units of the polymer), while the y and z dimensions were set to large values (15 and 10 Å, respectively) to eliminate spurious mirror interactions. Energy convergence within $10^{-4}$ Ry/atom was reached at a wavefunction cutoff energy of 75 Ry, sampled with a 3x1x2 Monkhorst-Pack k-points grid. Finally, the PDA surface was modelled by expanding the supercell to include four monomers, with dimensions optimized to 17.8x17.0x17.0 Å and using the Γ-point trick to accelerate convergence. The construction of the 4-monomers PDA chain will be detailed further on as it represented a source of uncertainty, thus requiring proper discussion. The reported computational parameters proved valid for accurately simulating the histamine molecule within the expanded supercell.

## Results and discussion

The experimental study involved two molecules: methylene blue (MB) and histamine. Although a computational study involving both could arouse considerable interest and lead to innovative results, the simulations focused solely on the histamine case study. This is because methylene blue introduces

certain computational criticalities that could have required significantly greater resources and calculation times. This is a consequence of the size of the MB molecule, which is characterized by more than twice the number of atoms as the histamine molecule, thus representing an additional difficulty that translates into greater computational complexity. Furthermore, the greater spatial expansion of the molecule could also have influenced the required size for the supercell and, inevitably, the number of monomeric units to be inserted, bringing the overall number of atoms to a significantly higher value.

The simulations on the histamine molecule did not present any evident criticalities. The dimensions of the used supercell made it possible to avoid spurious interactions between replicates due to periodicity. The optimized geometry of histamine, along with the relative bond distances, is reported in Figure 6.b.1.

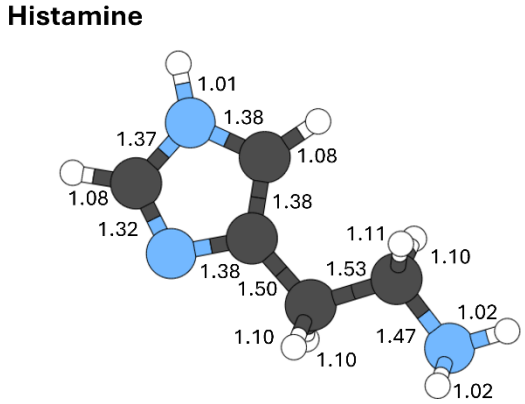



*Figure 6.b.1: Optimized histamine molecule. Bond lengths are displayed (in Å).*

Greater challenges emerged in the study of polydopamine, as this material does not exhibit a conventional polymeric structure. Indeed, it is known that the relative arrangement of the various monomers in space is incredibly variable and, furthermore, there might not be strict control over the shape of the monomeric unit. Therefore, it is useful to split the overall problem into two parts, isolating the issue of the monomeric structure from the relative arrangement between the fundamental units of the polymer.

As clearly highlighted by Liebscher et al. (2013), the dopamine-derived monomer can exist in four distinct structural forms[9]. During the polymerization process, dopamine can undergo various pathways to generate dissimilar structures with different theoretical capabilities to interact with surrounding molecules. Several studies report that it is possible to control the resulting geometry by

appropriately modulating the synthesis conditions[10]. The most well-known geometry involves the complete rearrangement of the ethylamine group into a 5-membered ring and the conversion of the hydroxyl groups into carbonyls; this structure is widely recognized as the actual PDA monomer. Although doubts may arise regarding the real geometry of the monomer within the polymer matrix, this described structure was selected as the baseline model from which to construct various polymeric configurations.

To exploit the periodic properties of plane waves, it is possible to hypothesize the polymer chain extended along a specific direction. This is not completely accurate, knowing that PDA properties do not exhibit a predefined preferential polymerization orientation due to the possible relative arrangements between monomers[11]. For convenience, while acknowledging how this could represent a factor capable of influencing the simulation results, it will be considered that the monomers form a chain along x direction.

Since it was not possible to excessively extend the number of tests to be performed on different configurations, only four of them were simulated. These are reported in Figure 6.b.2, where the shape of the monomers is the one described in the previous paragraph. Each configuration is obtained by replicating the monomer four times. For these configurations, it is relevant to identify the formation energy, which can be calculated using Equation 6.b.1, which includes a term in the denominator to normalize the calculation result to a single monomer.

$$E_{form} = (E_{4mono} - 4*E_{1mono}) / 4$$

*Equation 6.b.1*

The values for the formation energies of the analyzed systems are reported in Table 6.b.1. All the tested configurations, which nonetheless represent a subset of the total possible cases, prove to be stable given their negative formation energy.

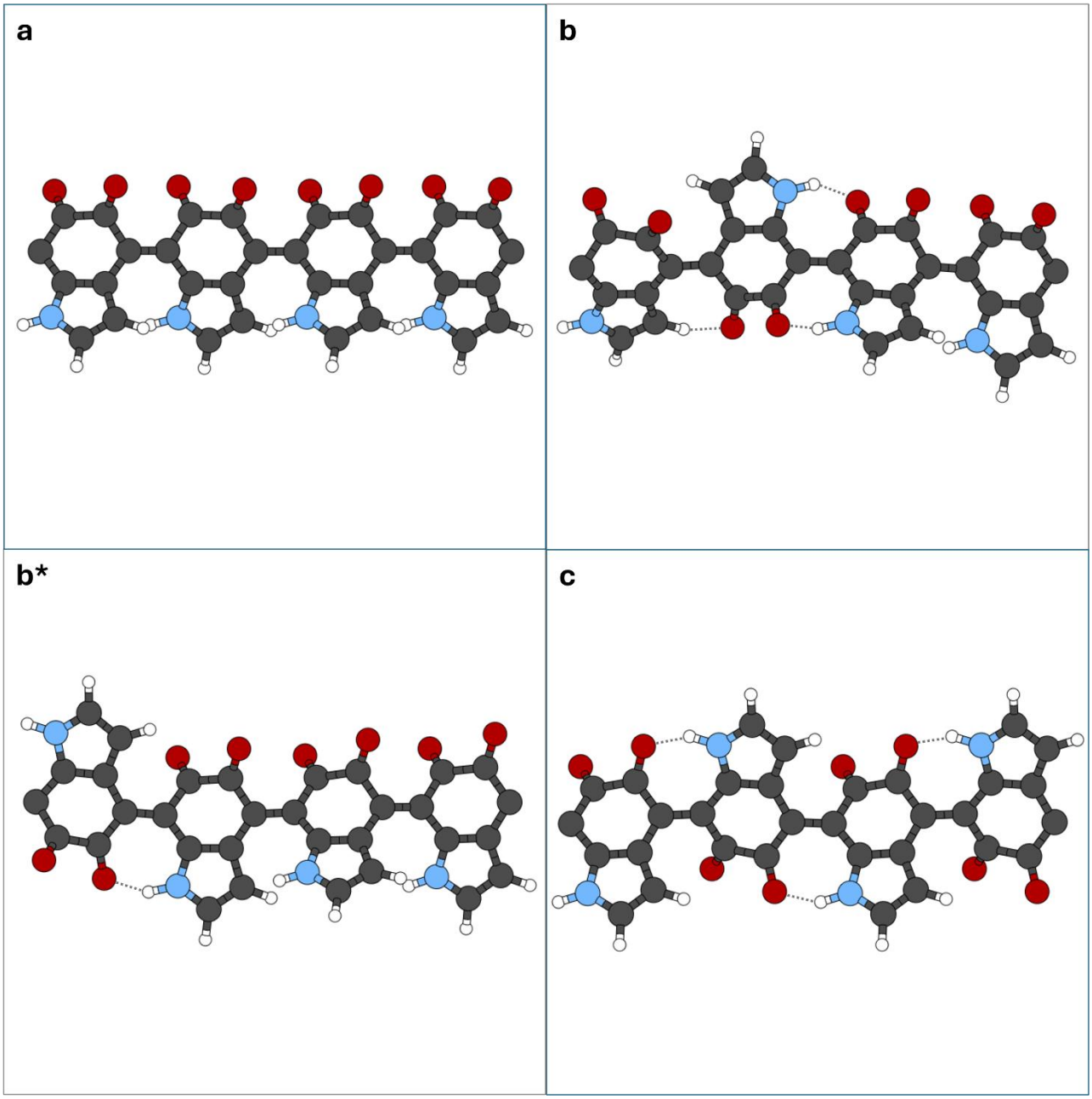



***Figure 6.b.2:*** *Four different investigated PDA configurations represented in the xy plane. Possible hydrogen bonds are represented as dashed lines. H-bonds formed due to periodicity are not shown.*

| PDA configuration | Formation energy (kJ/mol) |
|---|---|
| a | -54 |
| b | -69 |
| b* | -75 |
| c | -95 |

***Table 6.b.1:*** *formation energy for the four different PDA configurations.*

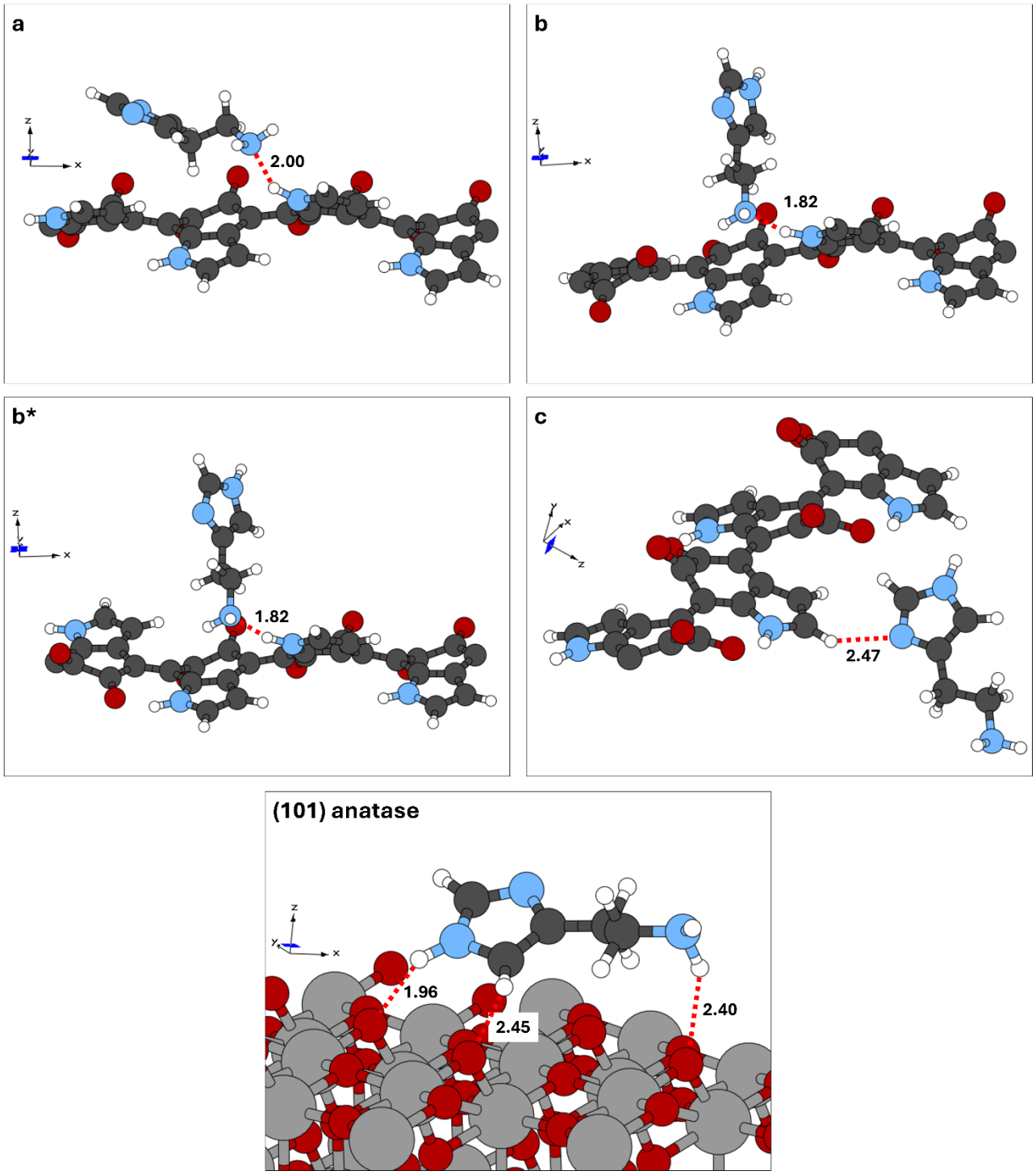



*Figure 6.b.3: Adsorption geometries for histamine on PDA and (101) anatase. Possible hydrogen bonds between molecule and surface are represented as dashed lines. Bonds formed due to periodicity are not shown. Configurations b and b* have been regenerated but remain equivalent to those in Figure 6.b.2.*

The adsorption energy for histamine on the various tested PDA chains is always negative, as reported in Table 6.b.2, just as it is for the anatase (101) used as a reference. It can be observed that there is a dependence on the surface in the value obtained for the adsorption energy. It is possible to identify

a trend where the chains with lower formation energy, and thus higher stability (such as c), are those that present less stable adsorption conditions. Conversely, in the case of surface a, where the formation of certain hydrogen bonds between adjacent monomers is prevented due to the rotation of the monomer itself around the x-axis, it can be verified that the adsorption energy is lower. It is important to emphasize that, in this case, histamine adsorption is coordinated to a hydrogen atom which, in other chains, directly participates in hydrogen bonding.

| Substrate | Adsorption energy (kJ/mol) |
|---|---|
| a | -45 |
| b | -46 |
| b* | -48 |
| c | -28 |
| (101) anatase | -37 |

*Table 6.*b.2: adsorption energy for histamine onto different PDA configurations. Adsorption energy on (101) anatase is reported as a reference.

The examination of the anatase (101) surface allowed to observe two correlated and particularly noteworthy phenomena. The molecule tends to align almost horizontally relative to the surface, with at least three hydrogen atoms electrostatically attracted by the surface oxygen atoms. However, the distances for at least two of these atoms are considerably larger than those found in the three PDA chain configurations that exhibit more favorable adsorption energies (*a*, *b*, and *b**). Given that adsorption on PDA is driven by a single hydrogen bond and yet yields stronger adsorption energies, it can be inferred that each individual interaction on the $TiO_2$ surface is characterized by a significantly lower binding energy than in the case of PDA. Overall, the results presented in Table 6.b.2 indicate that anatase offers less potential for robust histamine adsorption compared to PDA, with the sole exception of PDA configuration *c*. These considerations likely explain why PDA-coated T-Rex resonators enable a lower detection limit than their pristine counterparts.

## Conclusions

In this chapter, the discussion initiated in our previously published paper was extended. The main novelty of that work was the coating of T-Rex Raman resonators (titania-coated silica microspheres) with polydopamine (PDA) to facilitate the sensing of specific pollutants. Upon adsorption, the

resonator's optical properties amplified the signal of the adsorbate. Notably, while the bare resonator already enhanced the Raman signal of both methylene blue and histamine, the PDA functionalization yielded the most significant result, lowering the detection limit by one or two orders of magnitude.

Computational studies focusing on the interaction between histamine and PDA confirmed the occurrence of stable adsorption, characterized by strong hydrogen bonds forming between the molecule and the polymer. Reliable results were obtained even though the PDA geometry—particularly the relative orientation of the monomers within the polymer chain—is not entirely predictable, thereby requiring multiple tests with different chain configurations. Although the number of investigated configurations was limited compared to the total pool of possibilities, it was generally observed that adsorption on PDA is more stable than on the anatase (101) surface, which represents the bare, uncoated T-Rex resonator.

We expect that these results and this computational setup can be extended, thus enabling a deeper analysis also considering other coatings and target molecules, aiming to achieve a better selectivity in the Raman detection of specific chemical compounds.

## References


[1] I. Alessandri, 'Enhancing Raman Scattering without Plasmons: Unprecedented Sensitivity Achieved by TiO 2 Shell-Based Resonators', *J. Am. Chem. Soc*, vol. 135, p. 25, 2013, doi: 10.1021/ja401666p.

[2] N. Bontempi, L. Carletti, C. De Angelis, and I. Alessandri, 'Plasmon-free SERS detection of environmental CO 2 on TiO 2 surfaces †', vol. 8, 2016, doi: 10.1039/c5nr08380j.

[3] A. Boontanom *et al.*, 'Poly(dopamine)-coated TiO2/SiO2 resonators for the non-plasmonic SERS detection of organic analytes', *Appl. Surf. Sci.*, vol. 720, p. 165249, Feb. 2026, doi: 10.1016/J.APSUSC.2025.165249.

[4] K. H. Huynh *et al.*, 'Facile Histamine Detection by Surface-Enhanced Raman Scattering Using SiO2@Au@Ag Alloy Nanoparticles', *International Journal of Molecular Sciences 2020, Vol. 21, Page 4048*, vol. 21, no. 11, p. 4048, Jun. 2020, doi: 10.3390/IJMS21114048.

[5] P. Giannozzi *et al.*, 'QUANTUM ESPRESSO: a modular and open-source software project for quantum simulations of materials', *J. Phys.: Condens. Matter*, vol. 21, p. 395502, 2009, doi: 10.1088/0953-8984/21/39/395502.

[6] P. Giannozzi, S. Baroni, and N. Bonini, 'Advanced capabilities for materials modelling with Quantum ESPRESSO Related content QUANTUM ESPRESSO: a modular and open-source software project for quantumsimulations of materials', 2017, doi: 10.1088/1361-648X/aa8f79.

[7] P. Giannozzi *et al.*, 'Quantum ESPRESSO toward the exascale', *J. Chem. Phys.*, vol. 152, no. 15, Apr. 2020, doi: 10.1063/5.0005082.

[8] D. R. Hamann, 'Optimized norm-conserving Vanderbilt pseudopotentials', *Phys. Rev. B*, vol. 88, no. 8, p. 085117, Aug. 2013, doi: 10.1103/PhysRevB.88.085117.

[9] J. Liebscher *et al.*, 'Structure of Polydopamine: A Never-Ending Story?', *Langmuir*, vol. 29, no. 33, pp. 10539–10548, Aug. 2013, doi: 10.1021/LA4020288.

[10] L. Ghidoni *et al.*, 'Effect of surface Zeta potential on the deposition of inorganic nanoparticles on polydopamine (PDA) grafting layers', *Colloids Surf. A Physicochem. Eng. Asp.*, vol. 727, p. 138460, Dec. 2025, doi: 10.1016/J.COLSURFA.2025.138460.

[11] H. Hemmatpour *et al.*, 'New insights in polydopamine formation via surface adsorption', *Nature Communications 2023 14:1*, vol. 14, no. 1, pp. 664-, Feb. 2023, doi: 10.1038/s41467-023-36303-8.

# 6.c Estimation of the deacetylation grade of chitosan via FTIR spectroscopy

*This chapter provides a general outline of a draft paper that has not yet been submitted for publication. The future need to maintain a sufficient degree of originality to ensure a more streamlined review process has forced the removal of some important sections that are not strictly necessary for understanding the method described.*

*Several authors contributed to this study in different roles. Thus, sincere thanks are extended to Beatrice Cerea, Francesco Berneri, Giovanni Ribaudo, Alessandra Gianoncelli, and Ivano Alessandri.*

## Abstract

Chitosan is a highly versatile biopolymer with extensive applications in environmental and biomedical engineering. Derived from the deacetylation of chitin—a primary constituent of crustacean and fungal biomass—its production aligns with circular economy principles by valorising food industry waste. The degree of deacetylation (DDA) is a critical factor conventionally determined via $^{1}$H NMR spectroscopy. While NMR provides accurate and rapid quantification through direct signal integration, its widespread application is often constrained by high operational costs and equipment accessibility. In this work, an alternative methodology based on ATR-FTIR spectroscopy is proposed. The developed method directly exploits the carbonyl absorption peak, and it is designed to promote automation, eliminating the requirement for manual data preprocessing. The algorithm was validated on both commercial chitosan samples and samples obtained from commercial chitin through alkaline deacetylation.

## Introduction

Chitosan applications span various fields, notably water treatment, sustainable agriculture, medicine, and the food industry. It is obtained through the deacetylation of chitin, a polysaccharide present in the exoskeletons of certain crustaceans and insects, as well as in fungal cell walls[1]. These organisms can represent food industry waste, proving to be low-cost economic and environmental sources of chitin. The procedures used to obtain chitosan from this waste vary depending on the specific origin of the biomass, as extracting the substance requires separating it from an organic matrix containing proteins, other polysaccharides, and inorganic compounds[2]. The deproteinization and

demineralization processes necessary to remove these substances can influence the reaction yield. For this reason, especially when a high degree of purity is not required, their application is not particularly widespread.

The deacetylation process that converts chitin into chitosan is universally present. The common strategy involves high-concentration strong bases combined with a moderate temperature increase[3]. Although the procedure depends on the desired purity level and the starting material, the removal of the acetyl group is generally achieved at least partially. Consequently, determining the degree of deacetylation (DDA%) of chitin—the percentage of monomers that have lost the acetyl group relative to the total—represents a major issue of interest[4]. Hereinafter, DDA refers to the degree of deacetylation in general, while DDA% is used when the value is expressed as a percentage for mathematical rigor. This is accompanied by the fact that commercial chitosan standards exhibit different degrees of deacetylation. Additionally, potential internal inhomogeneities in commercial reagents must be considered, given their not fully controllable biological origin.

The analytical technique primarily used to determine the DDA of chitosan is Nuclear Magnetic Resonance (NMR)[5]. Although NMR allows for an accurate and relatively rapid characterization, the required instrumentation is expensive and demands isotopically enriched solvents (such as $^{2}H$ and $^{13}C$).

For this reason, numerous studies have explored complementary techniques such as InfraRed spectroscopy[6]. The non-destructive nature of the technique, combined with rapid measurements and instrumental simplicity, has made DDA determination a highly popular case study. However, many proposed methods involve manual baseline correction operations that limit repeatability, often producing discordant results.

The method proposed in this work highlights an automatic baseline calculation method specifically for the region concerning the carbonyl peak. The combination of NMR and FTIR analyses allowed the construction of a calibration curve that utilizes the C=O stretching peak, extracted from the spectra via the application of the Savitzky-Golay filter over an extended spectral region. This result runs counter to the literature, where manual determination of the baseline—and consequently of peak intensities—is suggested as a valid option for DDA calculation.

## Materials and methods

Chitin (CAS: 1398-61-4) was purchased from Sigma-Aldrich (SA), and two commercial chitosan samples (CAS: 9012-76-4) were obtained from Sigma-Aldrich and BioBasic. According to the manufacturers, the Sigma-Aldrich standards are derived from shrimp shells, whereas the biological origin of the BioBasic sample remains unconfirmed. The certificate of analysis reported a DDA% of ≥75% for Sigma-Aldrich sample and ≥90% for BioBasic; no DDA specification was provided for standard chitin[7], [8].

In-house chitin deacetylation was performed by treating the powder in a 12 M NaOH solution for 1.5, 3 and 5 hours. Chitosan deacetylation was further promoted following the same treatment for 2 hours, accounting for its higher starting DA.

A total of seven samples already characterized via Nuclear Magnetic Resonance (NMR) were measured via Fourier Transform InfraRed (FTIR) spectroscopy.

FTIR spectra employed for method calibration were acquired using a Nicolet™ Summit Spectrometer equipped with an Everest™ Diamond ATR Accessory. Each spectrum resulted from the average of 16 acquisitions, with four independent replicates collected per sample using different powder aliquots. This multi-replicate approach was adopted to account for the intrinsic heterogeneity of chitosan, which may exhibit localized variations in the degree of deacetylation. The spectral resolution was set at 4 $cm^{-1}$, with a data sampling interval of 0.48 $cm^{-1}$ in the exported files. Unless otherwise specified, the term "spectrum" hereafter refers to the mean absorbance calculated from the four replicates.

To provide independent validation of the proposed method, all samples were additionally analysed using a Lyza 7000 ATR-FTIR spectrometer (Anton Paar) and a Nicolet iN10 micro-FTIR (Thermo Fisher Scientific). For the external validation on the Lyza 7000, spectra were averaged over 24 scans with a single replicate per sample to verify the predictive performance of the calibration curve. These measurements were acquired at a spectral resolution of 2 $cm^{-1}$, yielding a data sampling interval of 0.66 $cm^{-1}$ in the exported files. For the Nicolet iN10 analysis, 16 scans were averaged per individual particle focused under the microscope. To account for sample heterogeneity, 31 distinct particles were analysed per sample. The spectral resolution was set to 4 $cm^{-1}$ with a data sampling interval of 3.8 $cm^{-1}$. Within the setup including the microscope, the measurements were conducted in reflectance mode.

Both ATR spectrometers were equipped with detectors operating at room temperature, eliminating the requirement for liquid nitrogen cooling, which was employed when reflectance measurements were performed. For a typical measurement, a small quantity of the powder sample was placed directly onto the crystal surface. Consistent contact between the sample and the crystal was ensured by applying a constant load via the integrated pressure device.

A mathematical treatment was performed employing the Savitzky-Golay filter to calculate a baseline for each spectrum. This approach exploits the filter's low sensitivity to narrow absorption peaks when a sufficiently wide window is employed, effectively isolating the underlying spectral background. A detailed description of the whole method will be provided in the following section of this work as it represents a critical factor for the calculation of DDA.

## Procedural steps for the application of the method

Various commercial chitin and chitosan samples were subjected to further deacetylation using highly concentrated alkaline solutions for different periods of time. The degree of deacetylation (DDA) of these samples was subsequently determined via Nuclear Magnetic Resonance (NMR) spectroscopy. Given that the application of the two distinct methods (Hirai, 1991; Lavertu, 2003) yielded comparable results, the choice was to average them (Table 6.c.1)[9], [10].

The following description aims to separate the contribute of C=O peaks at 1655 cm-1, particularly identifiable in spectra of samples with low DDA, from the surrounding spectral features, typically associated to amide and water.

Although the results that will be presented in this chapter were obtained through the application of calculus software, the relevant algorithms required to extract the carbonyl peak are typically available within standard "spectral math" toolsets. Most instrument-related software allows for these methods to be applied through intuitive manual procedures. The following steps provide guidance on how to process the acquired spectra to directly employ the calibration coefficients proposed in this work:

1. Spectrum acquisition
2. Smoothing
3. Horizontal baseline correction
4. Normalization
5. Baseline calculation

6. Baseline subtraction
7. DDA Estimation

## 1. Spectrum acquisition

In addition to the standard recommendations provided for performing robust FTIR measurements, it is worth emphasizing that chitin and chitosan samples can exhibit significant internal heterogeneity. Consequently, different portions of the same sample may display widely varying degrees of deacetylation; therefore, it is recommended to acquire multiple measurements across different sample aliquots and use the average spectrum as the representative profile. As reported in the Materials and Methods section, four replicates per sample were performed for ATR-FTIR measurements, at least regarding one of the two spectrometers used. In the case of micro-FTIR measurements, the ability to partially automate acquisition via mapping increased the number of replicates to 31 per sample. Representative spectra for some chitin and chitosan samples are reported in Figure 6.c.1.

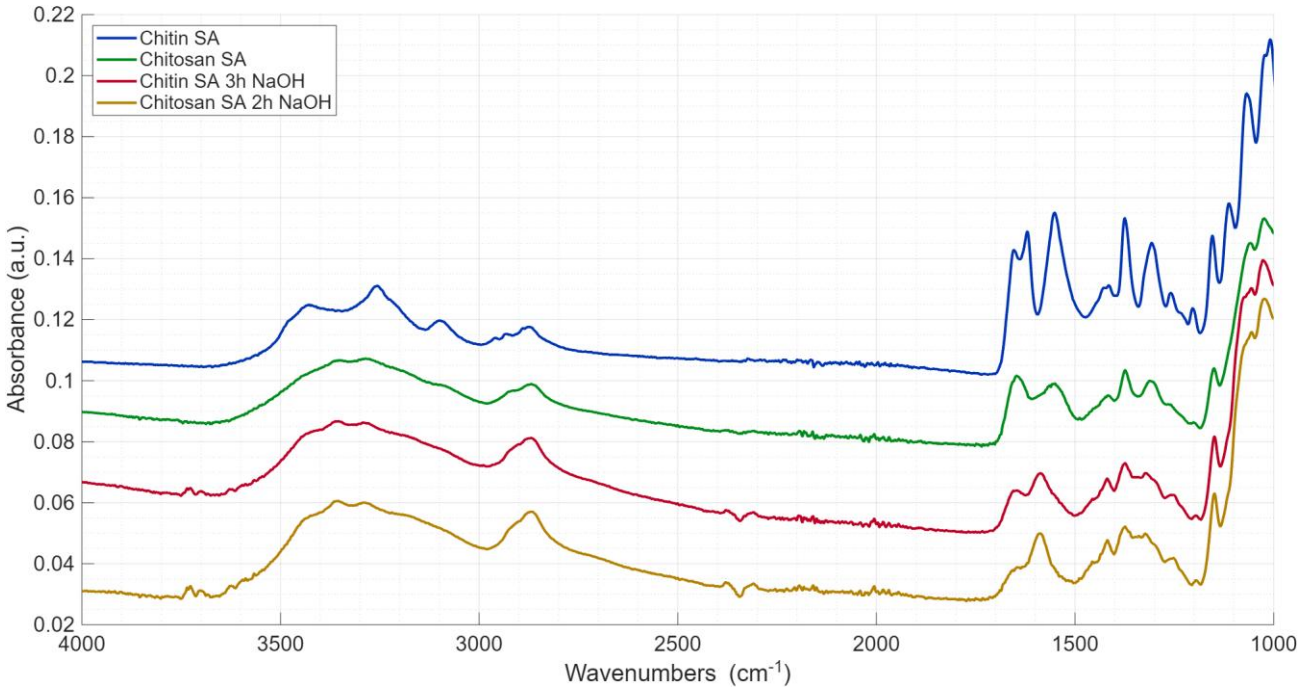



***Figure 6.c.1:*** *representative spectra for chitin and chitosan. Spectra are vertically shifted to enhance comprehension.*

## 2. Smoothing

The method detailed below does not strictly require the measured data to undergo smoothing. This is also supported by the fact that each measured spectrum is an average calculated from several acquired spectra. However, since the detector may be sensitive to thermal interference, particularly if it is not cooled with liquid nitrogen, a mild smoothing that does not suppress spectral features could be a reasonable option. Additionally, this procedure might be useful if the spectrum, or the average of multiple spectra, is characterized by systematic artifacts, likely resulting from a measurement instrument that is not fully efficient. For this reason, it was decided to proceed with smoothing using the Savitzky-Golay filter, with a spectral window of approximately 10 $cm^{-1}$ and a polynomial order of 0. Note that the same algorithm will be used for a completely different purpose for the baseline calculation.

## 3. Horizontal baseline correction

FTIR measurements may lack absolute repeatability because spectral intensity depends on local conditions, including sample thickness, instrument characteristics, and the pressure exerted by the ATR crystal on the sample. Ensuring comparable intensities across different spectra is essential for developing a generalizable method. Therefore, a vertical normalization (rescaling) is required. This process anchors at least two significant spectral points to constant values. One of these points is the baseline, set at 1750 $cm^{-1}$ as it appears free from spectral features in the analysed samples. For convenience, the calculation formula is presented in the following section.

## 4. Normalization

As stated in the previous section, spectrum normalization requires at least two points. The first corresponds to the previously identified horizontal baseline. The second is a peak to be rescaled to a constant value, defining the scaling factor applied to the entire spectrum. For convenience, the peak at approximately 1420 $cm^{-1}$ was selected, as it is commonly assigned to the-$CH_2$ scissoring vibration, which is a functional group unaffected by the deacetylation process. The formula combining the horizontal baseline correction and subsequent vertical rescaling is presented in Equation 6.c.1, while spectra normalized with this correction are reported in Figure 6.c.2.

Some tests conducted over the acquired spectra may suggest that spectra of samples with a low degree of deacetylation (DDA) are influenced by additional contributions in this region. Consequently, the proposed method is considered unreliable for samples characterized by low DDA, such as the ones commonly referred to as "chitin". This limitation can be easily monitored: chitin exhibits a prominent peak at approximately 1620 $cm^{-1}$ associated with the amide I band. Since this peak completely disappears when a mild deacetylation is introduced, it serves as an effective indicator for the applicability of the proposed method for DDA estimation.

$$spec_resc = (spec - base_{1750}) / (A_{1420} - base_{1750})$$

Equation 6.c.1

- spec_resc: rescaled spectrum
- spec: raw spectrum
- base1750, A1420: raw absorbance at 1750 and 1420 $cm^{-1}$

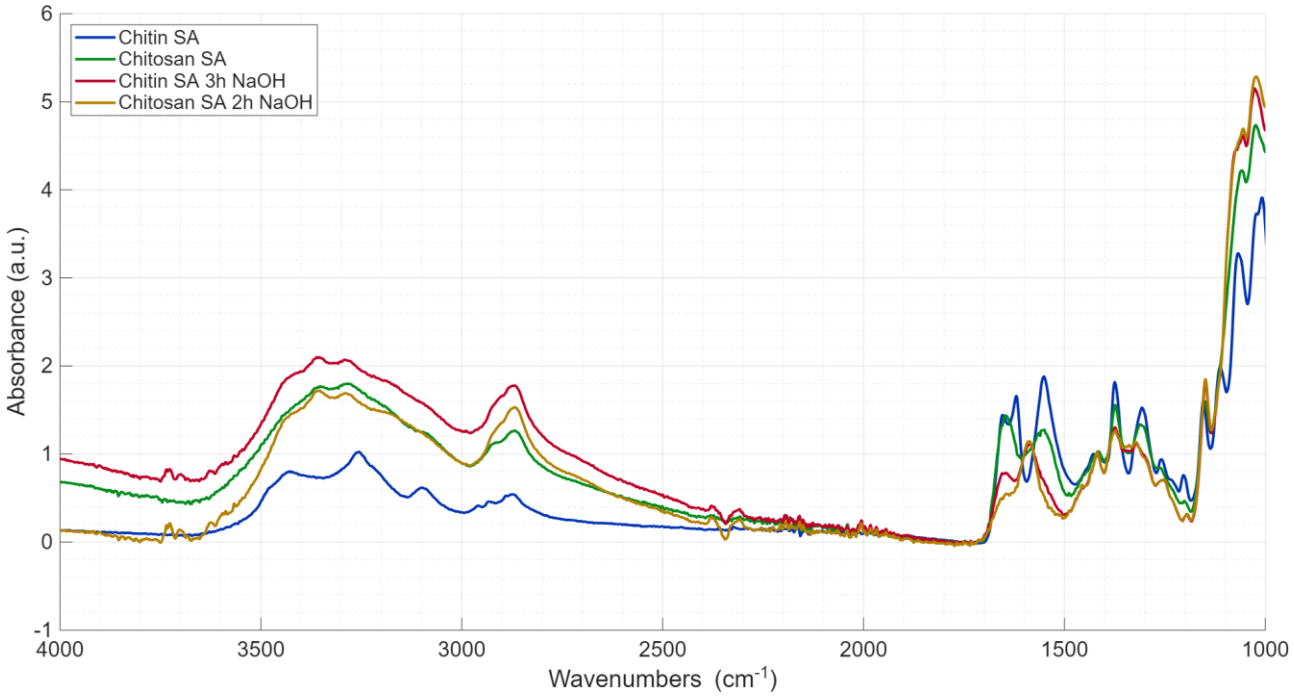



*Figure 6.c.2: representative spectra for chitin and chitosan. Vertical shift was not introduced to enhance effects of normalization.*

## 5. Baseline calculation

This section details the calculation of a baseline designed to isolate the C=O peak from the overlapping peaks within the spectral region around 1600 $cm^{-1}$. In addition to the peak of interest, this region is characterized by contributions from the water bending vibration—which is generally masked by adjacent peaks—and the amide II band. In highly acetylated samples, the amide I band peak is also present; however, as previously stated, the proposed method lacks robustness for a low DDA.

The method that we are proposing relies on the application of the Savitzky-Golay (SG) filter with specific input parameters. The goal is a baseline calculation; thus, no mathematical derivation must be included. It is known and easily understandable that SG filters applied over a sufficiently wide wavelength region allows for an evident smoothing, not considering the eventual presence of peaks. Although there is some subjectivity in the choose of the polynomial order, a trade-off between horizontal line and high value which could moderate the effect of the extended spectral window must be considered. Empirically, a window of 465 point, corresponding to a spectral range of around 223 $cm^{-1}$ centred in the point of application, was employed. A coherent spectral range should be the parameter to consider when considering spectra exported with a different sampling. Calculated baseline for spectra reported as example in the previous images are reported in Figure 6.c.3.

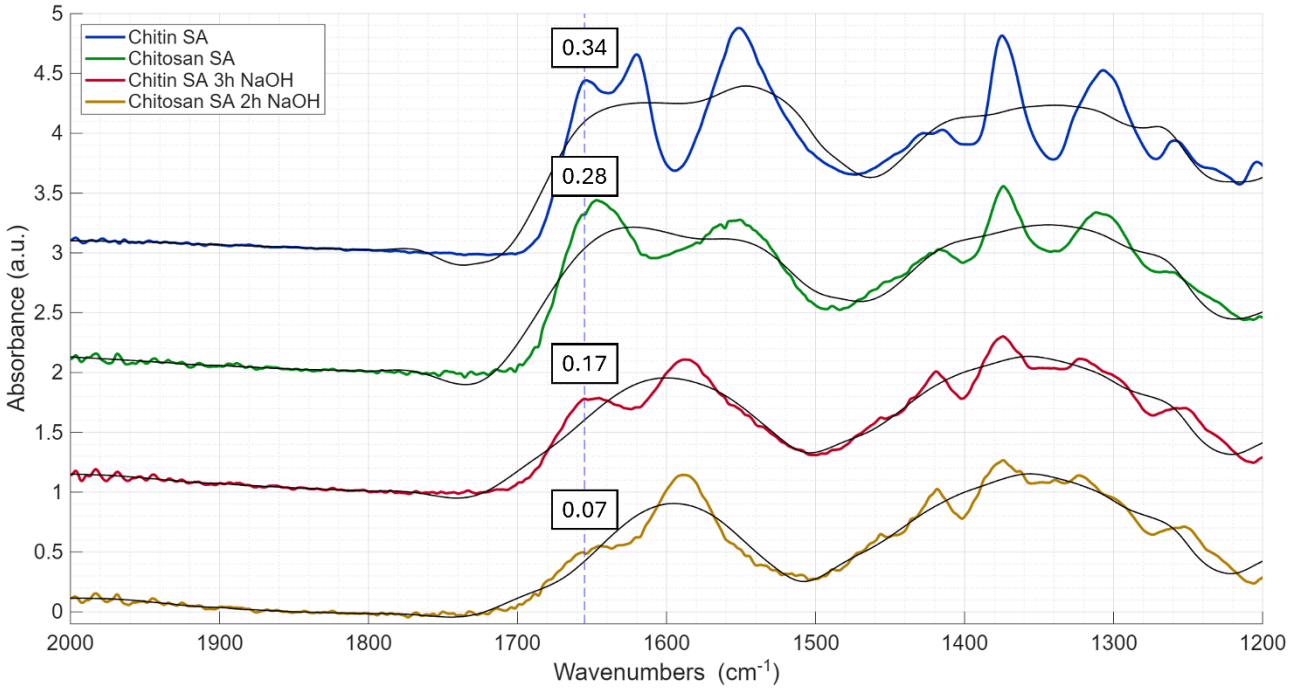



***Figure 6.c.3:*** *normalized FTIR spectra of chitin and chitosan, showing the baseline calculated via the Savitzky-Golay filter as described in the text. The absorbance of the C=O peaks after baseline correction are also reported.*

## 6. Baseline subtraction

The baseline calculated in the previous step must be removed from the spectrum through simple subtraction. It will be noted that in certain regions, the calculated baseline absorbance values will exceed those of the spectrum itself; therefore, this profile might not strictly define a conventional baseline. This specific approach lacks general applicability, and its validity was recognized empirically for the case under study. To apply similar methods to other case studies, a case-by-case analysis is highly encouraged. Representative baseline-corrected C=O peak absorbance values are illustrated in Figure 6.c.3.

## 7. Calibration line fitting

Labels reported in the Figure 6.c.3 highlight a decreasing trend for the absorbance of the baseline-corrected carbonyl peak associated with increment of the DDA. This opens for the definition of the linear application described by Equation 6.c.2, with the coefficients calculable by the application of the Ordinary Least Squares (OLS) approximation, working as a calibration line. Aiming to obtain an accurate method for calculation of DDA of chitosan which should be accurate and fast to implement, the easiest polynomial function which could obtained is the one described by Equation 6.c.2, with the coefficient m and the numerical constant q obtained by OLS. Since the focus is on the decrease in carbonyl peak baseline-subtracted absorbance ($A_{C=O}$, v=1655 $cm^{-1}$) after deacetylation, it appears more immediate to fit the model with the degree of acetylation (DA%). A comparison between $A_{C=O}$ and DDA% obtained from NMR spectroscopy is reported in Figure 6.c.4. Given the $A_{C=O}$ for the strongly acetylated sample (chitin), a superlinear function in the form $DDA\%=100-m*A_{C=O}^{b}-c$, b>1, or more complex solutions could be hypothesised. Given that the DDA of chitin cannot be accessed via NMR because of previously explained considerations, the actual slope of the curve for lower DDA cannot be determined. Linear approximation appears to properly describe sample with DDA higher than 60-65% until the almost complete deacetylation, which are the values for what defined as chitosan.

$$DA\% = y = m*x + q,\ x = A_{C=O},\ DDA\% = 100 - DA\%$$

Equation 6.c.2

- $A_{C=O}$: normalized, baseline-corrected absorbance of C=O peak
- m, q: coefficient determined via OLS

The calculated parameters describing the calibration curve are presented in Equation 6.c.3, demonstrating that the DDA can be effectively estimated from FTIR data. Table 6.c.1 reports the DDA values recalculated for both the calibration spectra and novel ones. A high level of consistency with the NMR results is observed, particularly for spectra acquired via ATR. Conversely, the error tends to increase for reflectance measurements. This issue is not fully resolved even by performing a new calibration to calculate new coefficients for the calibration line; therefore, further targeted analysis of this technique is required. The table also includes the calculated DDA for chitin, despite the lack of a reference NMR value and the previously discussed unreliability of the proposed FTIR method for such samples. For comparison, the DDA% calculated using the frequently employed method proposed by Brugnerotto et al. (2001) is provided[6]. This established method exhibits significant limitations for the analysed samples; consequently, its use is discouraged in favour of the method proposed in this work.

$$DA\% = y = 128.6 * A_{C=O} - 4.3,\ DDA\% = 100 - DA\%$$

Equation 6.c.3

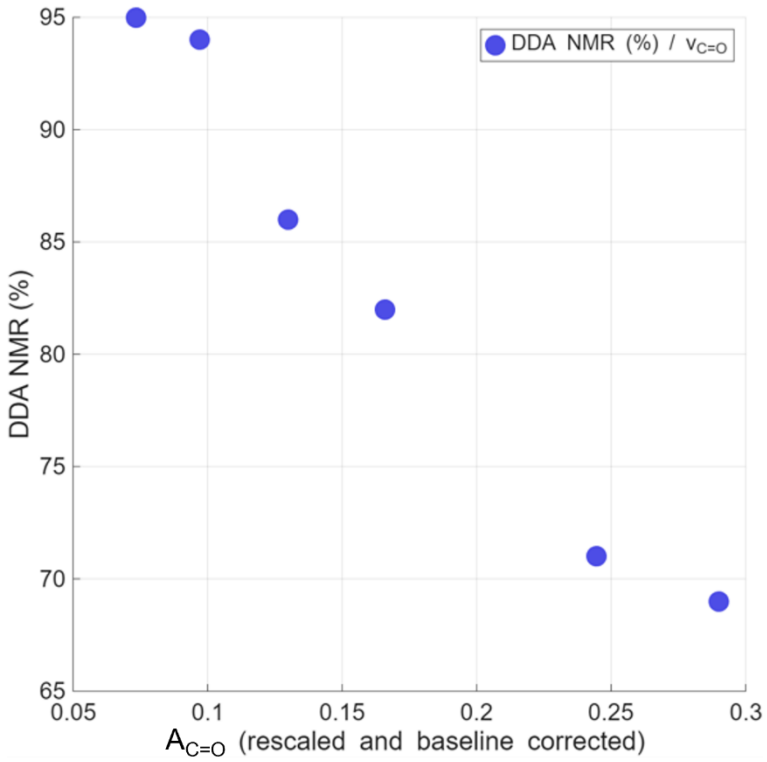



***Figure 6.c.4:*** *absorbance of C=O peak normalized and baseline corrected compared with DDA% obtained via NMR.*

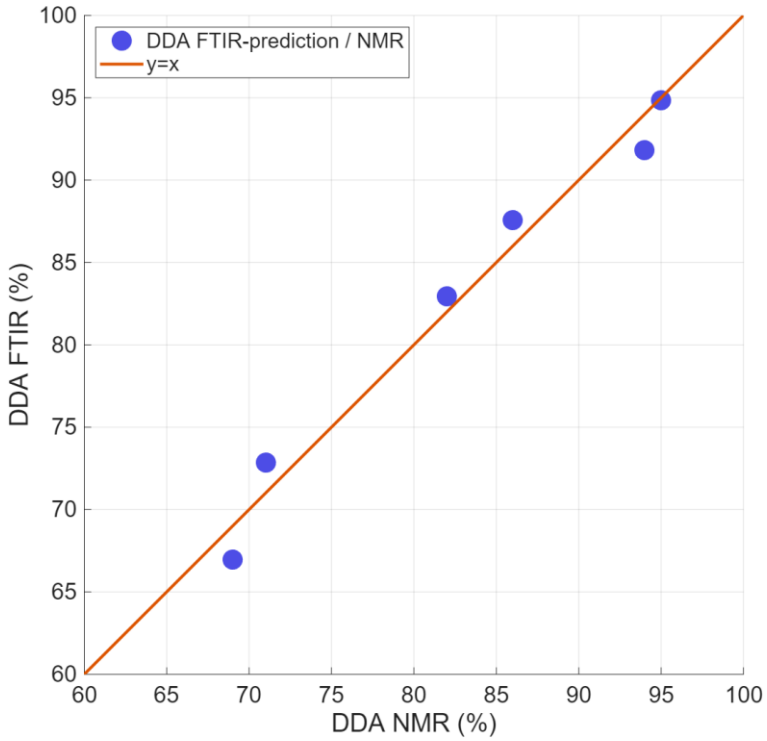



*Figure 6.c.5: DDA% calculated via NMR compared with DDA% calculated with the proposed method. Ideal prediction line is reported as reference.*

| | NMR (average of two methods) [9], [10] | Brugnerotto on ATR-Everest [6] | Proposed method on ATR-Everest (train) | Proposed method on ATR-Everest (test) | Proposed method on ATR-Lyza 7000 (test) | Proposed method on Reflectance (test) |
|---|---|---|---|---|---|---|
| Chitin SA | - | -55% | 65% | 65% | 75% | 74% |
| Chitosan SA | 69% | 40% | 67% | 70% | 66% | 87% |
| Chitosan BioBasic | 86% | 93% | 88% | 89% | 87% | 88% |
| Chitin SA 1.5 h | 71% | 85% | 73% | 78% | 75% | 77% |
| Chitin SA 3 h | 82% | 88% | 83% | 85% | 85% | 84% |
| Chitin SA 5 h | 94% | 85% | 92% | 93% | 93% | 96% |
| Chitosan SA 2 h | 95% | 90% | 95% | 95% | 95% | 99% |

*Table 6.c.1: DDA% calculated with different methods using NMR and FTIR spectroscopies. FTIR results are subdivided into train and test, to recognize which spectra were used to obtain the calibration line with the OLS method. Two different datasets were acquired with ATR-Everest to fulfil this purpose. SA=Sigma-Aldrich.*

Table 6.c.1 shows that the procedure enables the transfer of the proposed method and calibration curve to different ATR-FTIR instruments. However, a greater criticality emerges when applying them to spectra acquired via the reflection set-up; in this case, the estimated DDA% deviates more significantly from the reference value, which is conventionally represented by NMR data. This discrepancy is particularly pronounced for chitosan samples with a low degree of deacetylation, such as the commercial chitosan purchased from Sigma-Aldrich, whereas it is considerably more contained for samples with a high DDA.

The reason behind this phenomenon has not been clearly identified; however, several hypotheses have been formulated, the validation of which is encouraged as a possible extension of this work. One of the reasons limiting the portability of the proposed method is directly linked to the different measurement technologies employed, leading to varying intensities in the measured spectral features, thereby affecting the DDA% estimation.

Nevertheless, it should be emphasized that normalizing the data using the spectral features associated with the C=O and $CH_2$ groups should limit, if not eliminate, the issues arising from directly incomparable measured intensities. Supporting this, as previously discussed regarding the necessity of baseline correction and normalization, the portability of the method to data acquired with different instruments is not achieved without these procedures. For this reason, the hypothesis that the poor portability of the final method, which includes normalization, stems entirely from the measurement technology exhibits limitations in its robustness.

Another hypothesis advanced to explain the origin of this issue focuses on the poor homogeneity of the chitin and chitosan samples. This leads to a varying local DDA% and, potentially in a related manner, to a differing water content across the individual measured spots. To confirm this, future research should incorporate an extended campaign of NMR and FTIR measurements, thereby providing deeper insights into the micro-structural variations of the biopolymer matrix. Lastly, it should be noted that the baseline definition method based on the Savitzky-Golay algorithm represents, to some extent, a novel approach, which might not be the optimal way to extract the

spectral features of interest from the raw data. Consequently, experimentation with alternative algorithms, potentially considering the direct deconvolution of the peaks of interest, is encouraged.

Despite the discussed limitations, empirical evidence suggests that the method remains effective for samples characterized by a high DDA%. This could be particularly relevant in many contexts where the objective is to achieve an almost complete degree of deacetylation—a factor that, as previously emphasized, naturally distinguishes chitosan from chitin. Therefore, the specific experimental context in which the method is applied could mitigate inaccuracies and, consequently, enhance the overall level of accuracy.

## Conclusions

This work presented a rapid tool for DDA estimation in chitosan sample via FTIR spectroscopy. This approach overcomes several issues introduced by NMR spectroscopy, such as prohibitive costs, long analysis times, and the need for specialized personnel. The method introduced by the present work relies on a baseline calculation algorithm based on the Savitzky-Golay filter with a large spectral window. The method supposes that baseline is subtracted from the measured spectrum, thus this avoids suppression of the spectral features while the intensity of the backbone of a spectrum is reduced. While this strategy has been fundamental to avoid problems related to the convolution of peaks associated with C=O, $H_2O$ and amide I band, this does not represent, in general, a valid correction method, mostly because of the artificial peaks that are introduced. After the correction, a linear function of the C=O peak to calculate DDA can be defined, employing NMR results as a ground truth. Comparison among the two spectroscopies shows that they are in strong agreement, with the possibility, thanks to FTIR spectroscopy, to perform many measurements in a reduced time, thus statistical parameters become more accessible. The calibration coefficients calculated herein proved valid for estimating the DDA on spectra acquired with a different ATR-FTIR spectrometer, demonstrating the robustness of the method. Conversely, applying the same procedure to reflectance spectra obtained via micro-FTIR resulted in a higher deviation from the NMR reference data. We expect that the investigated method could enable a better characterization of chitosan, with the general objective of supporting researchers to obtain more coherent results.

## References


[1] C. Thambiliyagodage, M. Jayanetti, A. Mendis, G. Ekanayake, H. Liyanaarachchi, and S. Vigneswaran, 'Recent Advances in Chitosan-Based Applications—A Review', *Materials 2023, Vol. 16, Page 2073*, vol. 16, no. 5, p. 2073, Mar. 2023, doi: 10.3390/MA16052073.

[2] K. Mohan *et al.*, 'Green and eco-friendly approaches for the extraction of chitin and chitosan: A review', *Carbohydr. Polym.*, vol. 287, p. 119349, Jul. 2022, doi: 10.1016/J.CARBPOL.2022.119349.

[3] X. Sun, Y. Wang, J. Yu, Q. Wei, and X. Ren, 'Study on the deacetylation and mechanism of chitin in natural deep eutectic solvent', *Int. J. Biol. Macromol.*, vol. 255, p. 127698, Jan. 2024, doi: 10.1016/J.IJBIOMAC.2023.127698.

[4] T. Martins, G. L. Oliveira, S. B. Henriques, and E. H. M. Nunes, 'Comparative Analysis of Analytical Methods for Quantifying the Deacetylation Degree in Chitosan Polymer Chains', *Materials Research*, vol. 28, 2025, doi: 10.1590/1980-5373-MR-2025-0108.

[5] R. Czechowska-Biskup, D. Jarosińska, B. Rokita, P. Ulański, and J. M. Rosiak, 'DETERMINATION OF DEGREE OF DEACETYLATION OF CHITOSAN- COMPARISION OF METHODS', *Prog. Chem. Appl. Chitin Deriv.*, vol. 17, pp. 5–20, 2012.

[6] J. Brugnerotto, J. Lizardi, F. M. Goycoolea, W. Argüelles-Monal, J. Desbrières, and M. Rinaudo, 'An infrared investigation in relation with chitin and chitosan characterization', *Polymer (Guildf).*, vol. 42, no. 8, pp. 3569–3580, Apr. 2001, doi: 10.1016/S0032-3861(00)00713-8.

[7] 'Chitosano from shrimp shells, ≥75% (deacetylated) | Sigma-Aldrich'. Accessed: Jun. 19, 2026. [Online]. Available: https://www.sigmaaldrich.com/IT/it/product/sigma/c3646

[8] 'SDS Chitosan BioBasic'. Accessed: Jun. 19, 2026. [Online]. Available: https://www.biobasic.com/amfilerating/file/download/file_id/26710/

[9] A. Hirai, H. Odani, and A. Nakajima, 'Determination of degree of deacetylation of chitosan by 1H NMR spectroscopy', *Polymer Bulletin*, vol. 26, no. 1, pp. 87–94, Jul. 1991, doi: 10.1007/BF00299352/METRICS.

[10] M. Lavertu *et al.*, 'A validated 1H NMR method for the determination of the degree of deacetylation of chitosan', *J. Pharm. Biomed. Anal.*, vol. 32, no. 6, pp. 1149–1158, Aug. 2003, doi: 10.1016/S0731-7085(03)00155-9.

# 6.d Baseline correction algorithm of Raman spectra: analysis of the Schulze algorithm in combination with smoothing

*This chapter takes inspiration from the work carried out regarding the article Ducoli S. et al., Comparison of different fragmentation techniques for the production of true-to-life microplastics, Talanta (2025). The data presented in this section of the thesis refer to a subsection of the Raman spectra measured, processed, and finally published according to the guidelines in the corresponding section of the paper. This chapter focuses primarily on the algorithms used for experimental data cleaning, although the issue of environmental microplastics and the contributions of the work described in the article will also be introduced. The corresponding author has been informed that part of the material will be reused here and has approved the drafting of this section of the thesis.*

## Abstract

The problem of baseline correction in Raman spectra represents an open issue that constantly receives attention from the scientific community. An interesting case study which required a specific focus on this was encountered in the context of analysis of microplastics, whose spectra showed not negligible baselines. Results of this analysis were presented in a paper, which scope was not the investigation of the effectiveness of mathematical processing of experimental data but an extensive characterization of microplastic obtained via different fragmentation techniques. Raman spectra of these samples required the application of a combined algorithm for smoothing and baseline correction, with the aim of preserving all and only the relevant information. This is partially opposed to the common practice, as manual baseline identification is often preferred, with the disadvantage of introducing a degree of operator subjectivity and potentially affecting measurement reproducibility.

Within the scope of the published work, the baseline correction algorithm developed by Schulze implemented by Al-Rumaithi with Matlab code was evaluated in combination with a mild smoothing obtained by averaging over three replicates and the application of Savitzky-Golay filter. The most effective approach was characterized by the smoothing prior to baseline correction, although it is not a strict requirement as it will be demonstrated.

This thesis chapter primarily discusses the rationale that led to the development of the final algorithm. The methodology will be illustrated using selected LDPE spectra, although the proposed

approach is expected to be broadly adaptable to a wide range of contexts, thereby offering significant potential for application in different fields of analysis.

## Introduction

Raman spectroscopy demonstrated its potential in many context, as it allows material characterization with high accuracy. This is fundamental in chemical and pharmaceutical applications, both on laboratory and industrial scale, but it finds noteworthy applications in other fields of analysis, such as medicine, cultural heritage and scientific police[1]. Space is given to Raman also when Infrared spectroscopy, which represents its dual, is not convenient. IR shows an almost exclusive sensitivity to organic compounds, and, moreover, it is often not applicable when the content of water in the sample is moderately high[2].

The wide range of uses of Raman spectroscopy is accompanied by many criticalities. In some cases, they are specific to the application sector, together with the fact that the operator may not be able to carry out an in-depth analysis of the spectra which would require additional time. To better clarify this issue, the spectroscopic study of works of art can be mentioned. Raman spectroscopy is often referred to as a non-destructive technique, as it virtually does not require sample treatment prior to the measurement[3]. At the same time, it is required that the sample is irradiated with a laser, with the risk of local damage. Less energetic light sources or lower exposition times may not be effective for appreciable signal-to-noise ratios; thus, the identification of a thoughtful compromise may be a difficult choice. Other cases, such as scientific police operations and on-the-field characterization of unknown potentially illegal substances cannot be subjected to the necessity of tedious sample preparations. Moreover, often the analysis of powdery or colored samples may generate uncontrollable effects, such as light scattering or fluorescence. Raman cross-section, defined as the probability of the scattering event occurring, is typically very low. This could result in a complex material characterization, mainly when the analyte of interest is low in concentration or when the spectrum is critically affected by the previously mentioned artifacts[4]. In many cases their effect can be immediately recognized because of the presence of a non-polynomial baseline which affects the spectrum.

For these reasons, it is often required introduce some precautions when preparing and measuring a sample, although in many cases this is not practical or may require significant time efforts. For

example, due to its origin, fluorescence can be avoided changing the frequency of the incident laser [5]. A less energetic light source could abate the intensity of the recorded signal, requiring longer exposition time for appreciable measurements. This also requires the availability of different laser sources, with costs which may prohibitive. The mathematical treatment of the spectrum does not require additional hardware, representing an interesting opportunity for artifacts collections. This obviously cannot overcome some kind of issues, meaning that a spectral feature cannot be isolated from the baseline when, for example, its effect is enough strong to completely cover the peaks.

As this chapter includes microplastic characterizations as a case study for the development of an effective algorithm to decrease the noise in a spectrum and effectively remove the baseline effect, a brief introduction on the paper that we recently submitted[6].

Plastic pollution is widely recognized as a critical global issue due to its extensive environmental spread[7]. One of the key aspects associated with plastic contamination is the presence of micro and nanoscopic fibers, which originate from the fragmentation or release of plastic materials. The ecological impact of these particles is still under intense investigation, largely because of the virtually infinite ways in which they can interact with the various biological systems of living organisms[8].

The shapes and sizes of individual fragments vary significantly depending on the diverse environmental conditions that plastic waste encounters. For this reason, a study was conducted focusing on the characterization of microplastics produced in the laboratory through different mechanical procedures. The promising results obtained from this investigation was structured in the published work Ducoli S. et al, Comparison of different fragmentation techniques for the production of true-to-life microplastics, Talanta (2025)[6].

This investigation proved essential for understanding how various types of plastics undergo fragmentation and whether this process alters their spectroscopic signatures.

It was observed that, in some cases, specific spectral features disappear following the mechanical grinding of macroplastics. However, this effect strongly depends on both the type of plastic being analysed and the characterization technique employed. Such changes can provide valuable insights into the chemical structure of the resulting microplastics, allowing one to infer which chemical bonds may have been broken during mechanical fragmentation.

Due to the widespread problem caused by microplastic in the environment, four kinds of plastic (LDPE, HDPE, PP and PS) were fragmented in three different ways, using a Mixer Mill, an Ultracentrifugal Mill

and an Immersion Blender. This allowed a better comprehension of the behaviour of plastic in the environment, although plastic can still undergo uncontrollable fragmentation when it encounters natural elements.

A critical challenge during Raman analysis was the presence of broad and intense baselines in the measured spectra, particularly for milled samples. This compromised spectral comparisons, necessitating the application of a robust baseline correction algorithm. Manual baseline selection was judged not effective, due to the modest number of spectra acquired, in the paper just sixteen of them were presented, with each one of the is the average over three replicates to reduce instrumental noise.

The origins of this phenomenon have not been fully understood, as they may arise from multiple sources. Among these, the surface roughness induced by the milling process must certainly be mentioned, as it can cause disordered light scattering and consequently affect the measurement. Furthermore, despite the meticulous cleaning of the various mills employed, possible contamination by trace amounts of other chemical species capable of inducing fluorescence effects cannot be ruled out. The presence of the latter was not detected by the various characterizations performed but not reported here, including FTIR and XRD. Similarly, there is no evidence that the milling process triggered the formation of new chemical species from the original plastic through a mechanism akin to what is frequently referred to as "mechanochemistry," a term which highlights the role of the kinetic energy of the grinding balls in possibly promoting polymer fragmentation[9] . It should also be emphasized that although the spectrum of the ball-milled LDPE sample is characterized by a significant background, its presence—albeit often to a lesser extent—is substantially observed in every type of plastic milled using the three different modalities described in the published work. The decision to present solely this case study in this chapter of the thesis is intended to provide an easily understandable example.

Clearly denoising and baseline correction algorithm should be intended as distinct problems, which arise noteworthy interest from the scientific community, nowadays including automated Machine Learning components which demonstrated their effectiveness[10], [11]. On the other hand, this brilliant innovative approach requires competencies and robust dataset to train the models, thus its application to several sectors remain limited. To overcome cons of ML approaches, two strategies for an automatic baseline correction without its inclusion were evaluated. They rely on the Savitzky-Golay

filter, with different levels of sophistication. The most convenient one is substantially the method developed by Schulze in 2005, but with the application of a slight smoothing prior to it[12].

This section of the thesis aims to explicate the rationale behind the strategy that was established in the context of the published work. The methodology that will be presented is general and may find many other applications. Particularly, this can help when different kinds of artifacts -baselines, fluorescence, spikes- partially cover Raman features, helping both laboratory scale experiments and analysis on the fields, as it may avoid specific sample preparation or manual data correction.

## Materials and methods

For the purpose of this discussion, Raman spectra of LDPE will be presented in two forms: macroscopic (as fragments of a few millimetres) and ground via a ball mill. In this chapter, the latter will be referred to as Ball Mill (BM), whereas in the published paper it is termed Mixer Mill. The plastic was originally sourced from a semi-transparent film. To facilitate the grinding process, the samples were embrittled by immersion in liquid nitrogen for 30 minutes. Following the milling process, the fragments were passed through a 500 µm mesh filter to remove any insufficiently ground particles. Since the LDPE sample underwent a slightly different grinding procedure compared to the other plastic samples analysed in the published work, the reader is encouraged to refer to the original article for further details.

In the context of this work, some Raman spectra of two LDPE (Low Density Polyethylene) samples will be presented. One sample is defined as macroplastic, as it was a plastic piece with the size of few millimetres, will the other was obtained by the first after fragmentation using a Ball Mill (BM). This represents a subset of the study presented in the paper, which also included the analysis of HDPE, PS and PP; and fragmentation obtained with Ultracentrifugal Mill and an Immersion Blender. LDPE was embrittled before BM treatment with a 30-minute liquid nitrogen treatment prior to fragmentation, after whom the obtained powder was filtered employing a 500 µm mesh filter.

Measurements were obtained with a LabRAM HR spectrometer by Horiba and equipped with a He-Ne laser ($\lambda$ = 633 nm). In the published work it was also used a GaAlAs laser ($\lambda$ = 785 nm) to measure samples which exhibited fluorescence due to their pigments, specifically for polystyrene and to obtain a secondary check for HDPE, blue and green respectively. This factor does not directly influence the following discussion, as it will be focused on LDPE. Exposition time was calibrated accordingly with

the excitation laser energy: 1s for He-Ne and 20s for GaAlAs. All spectra were acquired in backscattering mode with 50x LWD objective and numerical aperture of 0.5, without optical filters. Each sample was measured at three different spots to ensure reproducibility.

The baseline correction algorithm in combination with denoising is detailed in the following section. It resulted in the method proposed by Schulze and distributed by Al-Rumaithi as Matlab code, hereafter referred to as SAR[12], [13].

## Results and discussion

Raw spectra of macroscopic and milled LDPE are presented in Figure 6.d.1-a and Figure 6.d.1-b respectively. Comparing these spectra, it appears that they do not present significant differences in terms of visible peaks. As demonstrated in the paper, this was not possible to establish it a priori, as for polystyrene samples the fragmentation made some Raman peaks less visible or even invisible. However, the data manipulation that will be described further on made spectra comparison easier and, without its application, it would be impossible to obtain this kind of consideration. What immediately emerges from the Figure is that two samples present different levels of absorption. Ball-milled plastic exhibited an evident band more critical for lower wavenumbers. This phenomenon is provoked by the roughness of the surface which promotes disordered scattering of light. Thus, this cannot be addressable as fluorescence, although both effects may disturb the analysis of the signal. From this quick consideration, one can understand the importance of defining a robust method for baseline correction. In case of Raman fluorescence, mathematical correction of the signal may be impossible as the possible peaks can be fused within the band. Thus, a change in the wavelength of the laser should be considered.

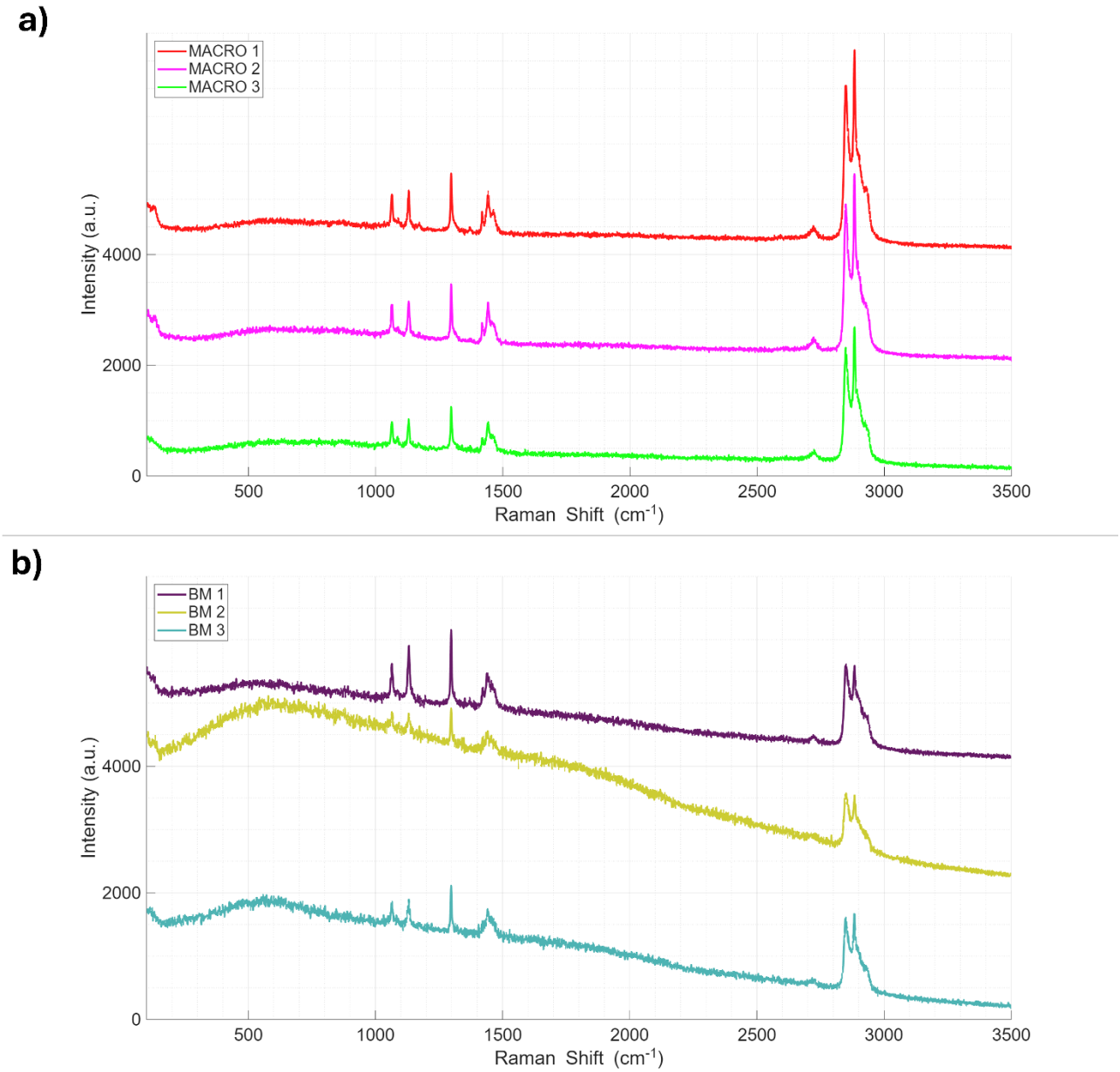



***Figure 6.d.1:*** *Raman spectra of LDPE a) macroscopic and b) microscopic samples. First and second replication were vertically shifted of 4000 and 2000 counts respectively for a more convenient visualization.*

Before detailing the SAR method, an algorithm based on Savitzky-Golay filter (SG) will be proposed, because of the interesting results it allowed for the calculation of deacetylation grade (DDA) of chitosan, as described in the corresponding chapter of this thesis. As highlighted in relation to the DDA estimation, the proposed method is specific to the context, and optionally other applications may be found. However, its eventual generalization must be evaluated case by case. This filter presents undiscussable advantages in terms of simplicity of applications, due to the availability of automated tools that allow its application and its integration in many common software which allow

standard spectral math. An example of this is Omnic Picta for FTIR Thermo-Fisher spectrometers, which also allow the investigation of Raman spectra. Both for the SG and SAR, the average (AVG) over the three replicates will be calculated as a first operation to reduce instrumental noise and correct eventual artifacts.

While a comprehensive description of the Savitzky-Golay (SG) filter is beyond the scope of this study, a brief overview of its input parameters is necessary. The algorithm requires three main parameters: window length, polynomial order, and derivative order. To apply this filter for baseline calculation, the derivative order must be set to zero. Furthermore, using a polynomial order of 0 prevents the formation of false positive peaks adversely affecting the visual interpretation of the spectrum. The window length, defined as the number of sampled data points used for polynomial fitting, must be carefully selected when applying this filter for baseline subtraction. For small windows, the resulting polynomial closely follows the spectral profile. Except for the specific case where window_length = polynomial_order + 1, the condition window_length > polynomial_order + 1 introduces a smoothing effect, which characterizes the algorithm as a filter. The filtering magnitude is directly related to the difference between the window length and the polynomial order. When window_length >> polynomial order, the filter captures macroscopic spectral features, such as broad bands and additive or multiplicative scattering, while effectively ignoring narrow peaks. By defining this calculated curve as base_SG, the substraction spectrum – base_SG yields a signal centered on the baseline that preserves the peak information. Figure 6.d.2 illustrates the application of this method to the average spectra of LDPE samples. For comparison, two baselines were calculated using a windows length of 201 and 21 points. Given the spectral sampling of approximately 1 $cm^{-1}$, these values correspond to spectral windows 200 $cm^{-1}$ and 20 $cm^{-1}$ respectively, each centred in the point which will be approximated.

As shown in Figure 6.d.2, the baseline calculated with a 21-points window generally follows the profile of the spectrum. However, in the presence peaks, the baseline fails to reach their full intensity, which is a positive characteristic due to subsequent subtraction. The difference between the original spectrum and the baseline generated a nearly flat signal, except for points where the strongest Raman features are recorded. This does not avoid the loss of information, because, for example, the C-H stretching at 2723 $cm^{-1}$ completely disappears. Furthermore, due to the algorithm's nature, the baseline partially overestimates the original spectrum near preserved features, leading to the

formation of false negative peaks. Consequently, if the objective is to enhance spectral legibility, this specific method proves to be inadequate.

Considering the work about DDA calculation, superior results may be obtained applying a baseline calculated over a 201-points window. This curve is less sensitive to narrow peaks; however, it effectively tracks broad, unwanted bands. While the occurrence of negative peaks remains a characteristic drawback of this method, it provides a clearer spectral interpretation compared to the 21-point baseline. The criticalities identified here demonstrate that using the Savitzky-Golay (SG) method for baseline correction in vibrational spectroscopy is not a universal or definitive solution.

A detailed analysis of Figure 6.d.2 reveals that several low-intensity spectral features, such as those at 1089, 1170 and 1371 $cm^{-1}$, are clearly identifiable in the average spectrum of the MACRO sample, while they are absent in the spectrum of milled sample, as obscured by noise. Consequently, a mild smoothing obtained with SG filter in combination with a more efficient baseline calculation algorithm may be considered.

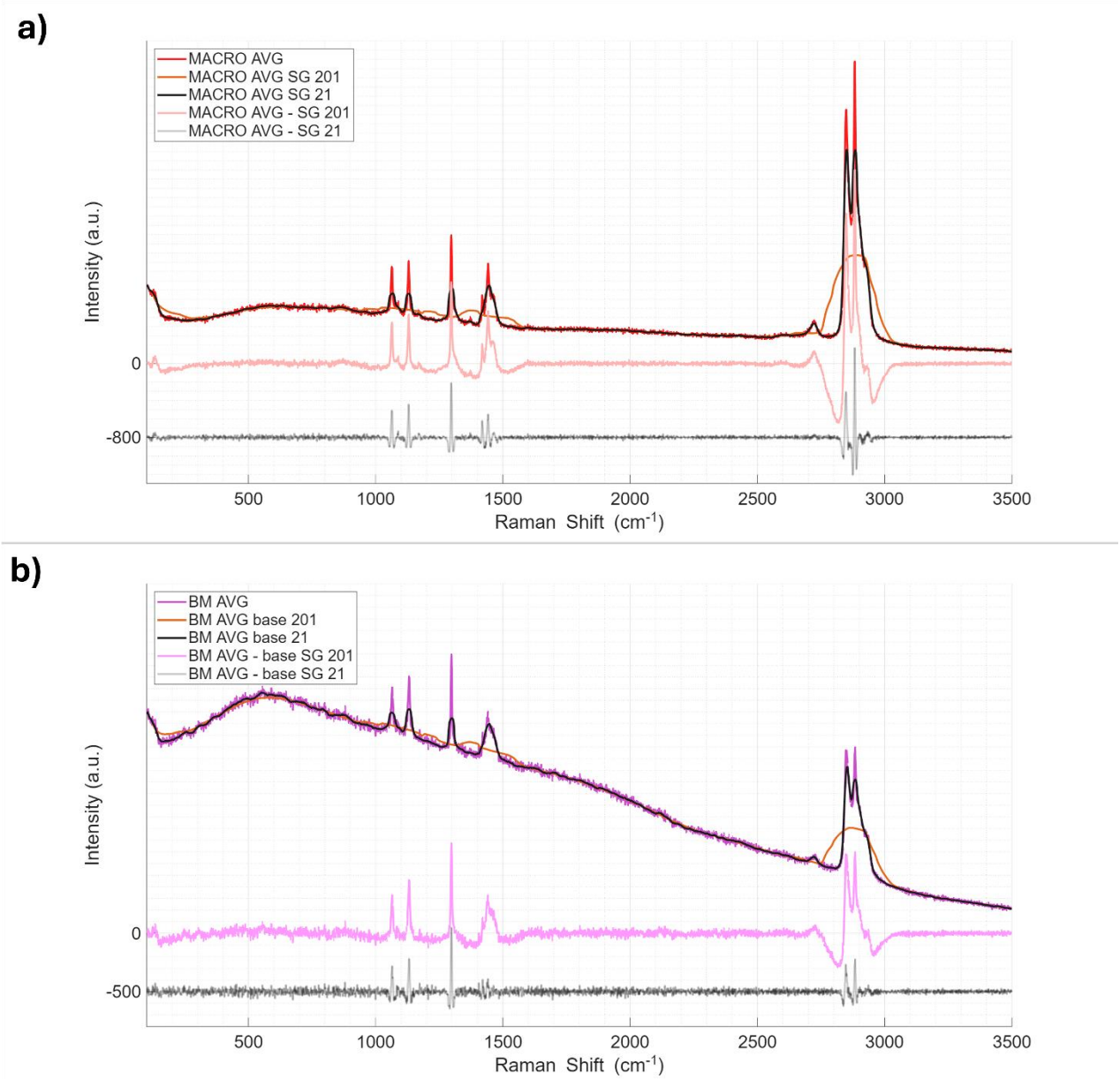



***Figure 6.d.2:*** *Raman spectra of LDPE a) macroscopic and b) microscopic samples. Measured spectra were averaged (AVG) and the baseline calculated with Savitzky-Golay method with a window of 201 and 21 points is reported. Baselines were substracted from the averaged spectrum. Result after 21-point baseline substraction is vertically shifted for a more convenient visualization.*

Given the limitations of the SG method for baseline calculation, the following analysis focus of the SAR method (Schulze's algorithm in the version of Al-Rumaithi). This algorithm natively incorporates the SG filter, with a more sophisticated approach, which can be divided into two distinct components: the internal and external modules.

In the internal module, SG filter is applied to with a window length of 50+n and polynomial order of 0. Variable n is iteratively increased by 2 from the external module, starting from a value equal to 3.

After this operation, a new spectrum is created comparing the original one with the filtered one, keeping for each sampled point the minimum between them. This may be considered as a temporary baseline. In the external module, the area A limited by the original spectrum and the temporary baseline is calculated. The cycle concludes when the relation A(i-2) > A(i-1) < A(i) is satisfied (i = (n-1)/2). This means that the algorithm stops when the difference between spectrum and temporary baseline, now definitive, reach a minimum. The application of the method SAR to LDPE spectra is reported in Figure 6.d.3. Baseline-corrected spectra do not present criticalities highlighted for SG. Specifically, false negative peaks are avoided, as the calculated baseline is constrained to be the minimum between the original spectrum and the filtered values.

The insight reported in the Figure shows a focus on the shape of the spectrum of fragmented LDPE in the region around 1100 $cm^{-1}$. It appears evident that the small peak now cannot be properly distinguished from the noise, thus smoothing may be applied. This can be obtained applying the SG filter, this time with the objective it was designed to. A relevant question is related to the best strategy for its application, before or after the SAR.

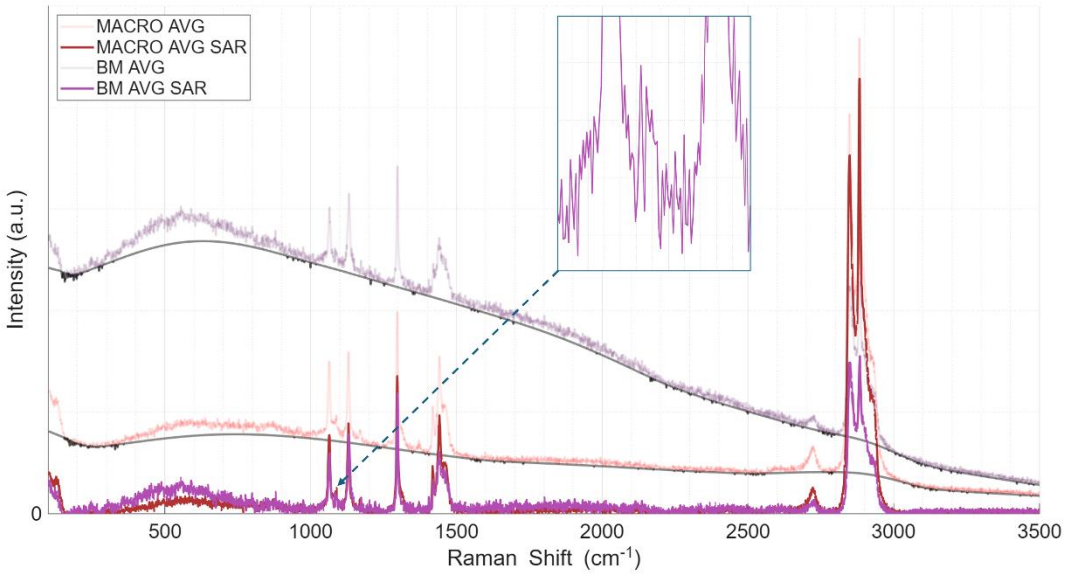



*Figure 6.d.3: Raman spectra of LDPE macroscopic and microscopic samples. Measured spectra were averaged (AVG) and the baseline calculated with Schulze_Al-Rumaithi (SAR) method is reported. Baselines were substracted from the averaged spectrum and a focus on the spectrum of BM after the correction is reported for a better visualization of the peak at 1087 $cm^{-1}$.*

In Figure 6.d.4 a comparison between the two cases, SG smoothing before SAR baseline correction or vice versa, is reported. SG filter here applied considered a window length of 9 point and a polynomial order of 2. This was judged a good trade-off between denoise and capability to accurately keep the intensity of the peaks. From this Figure, the order of application of the two algorithms is almost negligible, as spectra are almost identical. However, to obtain a more accurate baseline correction, it would be slightly better to apply the smoothing prior to it. In fact it helps in the removal of points with intensity lower than the baseline, allowing a more accurate result at the end of the procedure. This reason drove the choice also for results presented in the paper.

This algorithm allowed to detect which peaks were susceptible to the fragmentation, as presented in the paper for polystyrene spectra. Spectra of PS microplastic did not present some features typical of macroscopic sample. Focusing on the two LDPE spectra presented in this chapter, an interesting phenomenon can be evaluated. In fact, the peak at 1170 $cm^{-1}$ enhanced in Figure 6.d.4 cannot be properly detected in fragmented samples. This appears to be associated with this specific type of plastic and milling operation as this peak was visible in the spectra of plastic fragmented with Ultracentrifugal Mill and Immersion Blender. This is not clear in the Figure presented in the paper as the combination of noise and limited image resolution did not allow this conclusion. However, evaluating other kind of plastics and FTIR spectra after this consideration, some analogous cases where the fragmentation was obtained with Ball Mill (Mixer Mill in the paper) can be detected (e.g. FTIR spectra of polypropylene).

Although the brilliant results obtained after the application of the SG+SAR method, a hidden critical issue must be noticed. In fact, the algorithm could reduce the intensity of the peaks isolated from the baseline. More specifically, SG method is designed to obtain smoothing, thus the higher values of the peaks may be decreased. On the other hand, SAR should not directly act on the intensity of the peak, conventionally meant as the difference between the highest values or the central value and the baseline. However, more in general, SAR can introduce certain levels of alterations, depending on the shape of the spectrum and the signal-to-noise ratio. When the measured intensity of a peak cannot be deconvoluted as the sum between actual intensity and baseline, mainly because the intensity of the baseline partially covers the peak, the application of the method SAR must be properly evaluated. It appears then evident that the application of this method for some kind of quantitative analysis obtained by comparison of the intensity of two or more peaks could be affected by the mathematical treatment introduced.

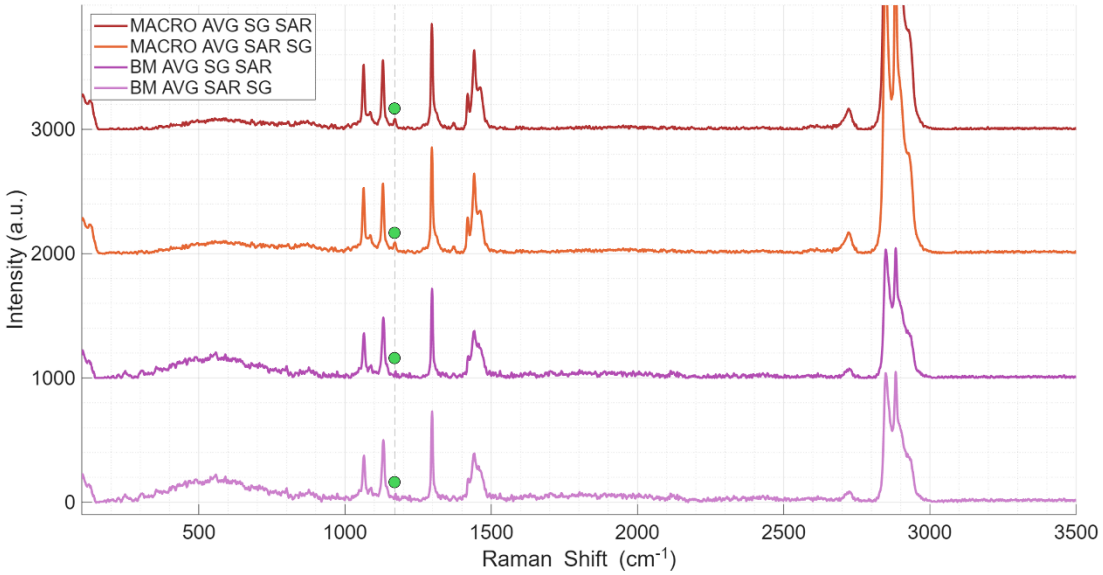



***Figure 6.d.4:*** *Raman spectra of LDPE macroscopic (MACRO) and microscopic (BM) samples. A comparison between SG smoothing and SAR baseline correction and viceversa is reported for both averaged spectra. Reported spectra were vertically shifted of 3000, 2000 and 1000 counts for a more convenient visualization. Aim of the green dots is enhancing the visualization of the peak at 1170 cm-1, which appear to be less visible in fragmented samples.*

## Conclusions

To conclude this section of the thesis, it is worthy underlining that baseline correction method for Raman spectra represents an open challenge, which requires deep analysis to avoid unwanted peak suppression and unnecessary complexity. An automated procedure which avoids user subjectivity in the selection of the baseline may be preferred, and the Schulze method seems to be a good opportunity. Combining this method with Savitzky-Golay filter, following the scheme referred to as SG+SAR, many spectral features can be surprisingly enhanced. As demonstrated in the published work and confirmed in this chapter, thanks to the application of this algorithm we could detect peak suppression due to fragmentation. As the main problem was due to strong baselines encountered during the spectral analysis on laboratory prepared microplastics, this phenomenon may evidently affect also samples collected from the environment.

Despite the effective results achieved with the SG+SAR method, certain limitations were identified. A primary concern is the potential for excessive smoothing, which may compromise quantitative accuracy despite the method's effectiveness for qualitative analysis. The algorithm that was presented

in this work is completely general and it could find other fields of applications. Thus, a future extensive test and use of the method is warmly suggested.

## References


[1] "What is Raman Spectroscopy? - HORIBA." Accessed: Jun. 19, 2026. [Online]. Available: https://www.horiba.com/int/scientific/technologies/raman-imaging-and-spectroscopy/raman-spectroscopy/

[2] Z. Li, M. J. Deen, S. Kumar, and P. R. Selvaganapathy, "Raman Spectroscopy for In-Line Water Quality Monitoring — Instrumentation and Potential," Sensors (Basel), vol. 14, no. 9, p. 17275, Sep. 2014, doi: 10.3390/S140917275.

[3] A. Candeias and J. M. Madariaga, "Applications of Raman spectroscopy in art and archaeology," Journal of Raman Spectroscopy, vol. 50, no. 2, pp. 137–142, Feb. 2019, doi: 10.1002/JRS.5571;WGROUP:STRING:PUBLICATION.

[4] R. teja Vulchi, V. Morgunov, R. Junjuri, and T. Bocklitz, "Artifacts and Anomalies in Raman Spectroscopy: A Review on Origins and Correction Procedures," Molecules, vol. 29, no. 19, p. 4748, Oct. 2024, doi: 10.3390/MOLECULES29194748.

[5] "Avoiding Interference from Fluorescence Signal by Performing Raman Spectroscopy Measurements at Excitation Wavelength of 1064 nm - JASCO %." Accessed: Jun. 19, 2026. [Online]. Available: https://jascoinc.com/applications/avoiding-interference-from-fluorescence-signal-by-performing-raman-spectroscopy-measurements-at-excitation-wavelength-of-1064-nm/

[6] S. Ducoli et al., "Comparison of different fragmentation techniques for the production of true-to-life microplastics," Talanta, vol. 283, p. 127106, Feb. 2025, doi: 10.1016/J.TALANTA.2024.127106.

[7] C. Espinoza-González et al., "PRIORITY project in action: Advances and future directions on remediation, recovery, and development of sustainable alternatives to plastic materials to combat microplastic pollution," Open Research Europe, vol. 5, p. 391, Dec. 2025, doi: 10.12688/OPENRESEUROPE.21943.1.

[8] L. Zhu et al., "Transport of microplastics in the body and interaction with biological barriers, and controlling of microplastics pollution," Ecotoxicol. Environ. Saf., vol. 255, p. 114818, Apr. 2023, doi: 10.1016/J.ECOENV.2023.114818.

[9] M. A. Ghanem et al., "The role of polymer mechanochemistry in responsive materials and additive manufacturing," Nature Reviews Materials 2020 6:1, vol. 6, no. 1, pp. 84–98, Oct. 2020, doi: 10.1038/s41578-020-00249-w.

[10] S. Fang, S. Wu, Z. Chen, C. He, L. L. Lin, and J. Ye, "Recent progress and applications of Raman spectrum denoising algorithms in chemical and biological analyses: A review," TrAC Trends in Analytical Chemistry, vol. 172, p. 117578, Mar. 2024, doi: 10.1016/J.TRAC.2024.117578.

[11] S. Innocente, A. Visentin, S. Andersson-Engels, K. Komolibus, and R. Gautam, “Automated Baseline Correction Evaluation Score for Raman Spectroscopy,” vol. 11, 2026, doi: 10.1021/acsomega.5c09870.

[12] H. G. Schulze, R. B. Foist, K. Okuda, A. Ivanov, and R. F. B. Turnera, “A Small-Window Moving Average-Based Fully Automated Baseline Estimation Method for Raman Spectra,” Appl. Spectrosc., vol. 66, no. 7, pp. 757–764, 2012, doi: 10.1366/11-06550.

[13] “Raman Spectrum Baseline Removal - File Exchange - MATLAB Central.” Accessed: Jun. 19, 2026. [Online]. Available: https://it.mathworks.com/matlabcentral/fileexchange/69649-raman-spectrum-baseline-removal

# 7. Notes on the synthesis procedures and characterization of titanium dioxide

*This section of the thesis is the result of an original and independent analysis regarding characterization of titania samples. It should be noted that the XRD measurements were conducted by Dr. Saad Javaid. SEM characterizations were performed by Prof. Dario Zappa and Prof. Matteo Ferroni.*

The (001) anatase facet is highly attractive because of its capability to adsorb carbon dioxide. Consequently, the synthesis and the characterization of a $TiO_2$ powder which present that facet prevalently exposed were extensively investigated. Since developing novel synthetic strategies falls outside the scope of this thesis, established protocols adapted from the literature were followed or readapted. Two of them are reported at the end of this chapter. The first represented an interesting trade-off between procedural complexity, time, and product yield, although a detailed evaluation of the analytical data failed to confirm the predominant exposure of (001) facet. Interest in the second protocol arises from the unique morphological features observed in the synthesised $TiO_2$. However, a complete characterization of the powder obtained following this protocol was not possible due to the limited reaction yield.

Estimating the preferentially exposed facets of a powder remains an open challenge because many characterization techniques fail when certain conditions are not satisfied. In the following brief dissertation, an overview of different methods (XRD, Raman, SEM, TEM) will be presented.

From a theoretical point of view, powder X-ray Diffraction (XRD) is suitable for this purpose as it enables the detection of specific crystal planes. However, considering the physical phenomenon that allows the measurement of a diffraction pattern, this method can easily fail. This statement relies on the fact that only crystal planes parallel to the specimen surface can diffract the beam[1]. Thus, to observe an increase in the intensity of a peak associated with an exposed facet, the crystal morphology should be roughly flat, with the investigated facet oriented parallel surface of the sample.

Examples of anatase samples with preferentially exposed (001) planes, where the (004) peak is comparatively strong, confirm this hypothesis[2]. In fact, observing SEM characterization which complements the analysis, the crystals are usually flat and can easily arrange themselves parallel to the sample holder because of many physical factors, including gravity and electrostatic interactions. TEM characterization confirms that the flat surface is associated with the (001) plane.

On the contrary, other works focused on (001) anatase as a preferentially exposed plane did not show an increment in the intensity of the (004) peak[2], [3], [4]. Coherently, the morphology of the micro- or nanocrystals obtained was anything but flat. This is a consequence of the fact that the orientation of the particles was almost random. From this, it must be deduced that if the morphology of the powder is not flat, and there are no guarantees on crystal orientation, no conclusion can be derived from XRD characterization.

Raman spectroscopy has recently been proposed as a valid method for quantifying the exposed (001) facets of anatase[5]. This approach relies on the $A_{1g}/E_g$ intensity ratio and has shown promising correlations with results from complementary characterization techniques. Although it is supported by theoretical considerations regarding the symmetry of the (001) plane with respect to the (101) plane, the method has not yet found widespread application. Consequently, further research is required to fully validate this approach. In this work, Raman characterization was performed and the model was applied; despite some experimental limitations affecting the measurements, the calculated percentages followed a coherent trend. Additionally, Raman spectroscopy proved to be a valuable tool for detecting organic residues within the $TiO_2$ samples, which likely derive from the synthesis procedure.

Transmission Electron Microscopy (TEM) represents a powerful technique for identifying specific crystal planes, as it enables the direct measurement of the crystal lattice along defined crystallographic directions. A disadvantage introduced by microscopy is that the analysis is performed on a limited portion of the samples, and it can hardly offer a bulk evaluation of the entire sample. Although TEM characterization was planned to complement this study, it could not be performed due to instrument unavailability and is scheduled for the near future.

TEM analysis is often supported by Scanning Electron Microscopy (SEM) when a comparison of the morphology observed by the two techniques can be easily performed. This approach can allow facet estimation, despite the potential inaccuracies inherent to SEM imaging. In a relevant case of study related to (001) plane of anatase, because of the characteristic morphology of the crystals, the facet was properly identified via SEM for different $TiO_2$ samples[6]. Notably, just one sample was also characterized via TEM. While a parallel characterization using both techniques is typically preferred to ensure maximum robustness, the temporary unavailability of TEM required relying primarily on SEM analysis, which was then meticulously compared with literature data. Nonetheless, it must be

noticed that SEM characterization suffers the same problem of spot-dependency previously discussed for TEM.

## Synthesis I: recipe and XRD, Raman, SEM characterization

This synthesis procedure was adapted from the work of Song et al (2017)[4]. In their work, 2.5 mL of tetrabutyl titanate (TBOT) were mixed with 60 mL of isopropanol and the obtained solution stirred for few minutes. Subsequently, 1 mL of hydrofluoric acid (HF) was added dropwise under magnetic stirring. The solution was transferred to a 100 mL Teflon-lined autoclave and kept at 200 °C under hydrothermal conditions. The precipitate was harvested via centrifugation, washed with ethanol and dried at 60°C. According to the authors' estimations, the obtained $TiO_2$ sample exhibited approximately 85% of exposed (001) anatase facets.

In the synthesis that we performed to obtain (001) anatase as principal exposed facet, TBOT was replaced with titanium isopropoxide (TTIP) while maintaining the same volume. The employment of pure isopropanol could represent a risk as it may self-ignite in presence of high pressure and temperature; thus, it was diluted 70% v/v in water. In the original literature protocol, concentration of HF was not explicit; therefore, also considering the different precursor that was used, an accurate calculation to keep the same Ti/HF ratio was impossible. For this reason, 1mL of HF 49 wt. % was added. The obtained solution was transferred to a 125 mL PTFE container and subsequently kept at 200 °C for 24 hours. The choice of a larger container was driven by safety purposes, as maintaining an adequate headspace is essential during hydrothermal treatments, particularly when organic solvents are employed.

After synthesis, the dried powder exhibited a bluish coloration, suggesting the formation of non-stoichiometric $TiO_2$. Indeed, it is documented that sub-stoichiometric titanium oxides, such as $Ti_2O_3$, can display dark or even black colours, completely different from the brilliant white of $TiO_2$.[7] This observation suggests the presence of oxygen vacancies within the synthesized powder, a feature highly desirable for photocatalytic applications but distinct from the expected properties of a stoichiometric titania.

Furthermore, it was observed that a defective powder shifted to a yellow colour upon thermal treatment at temperatures exceeding 600 °C for 2 hours[7]. This phenomenon strongly indicates a chemical interaction between the powder and ambient oxygen, likely leading to re-oxidation. In a

different work, where the goal was the detection of carbon dioxide adsorbed over the (001) anatase facet, two distinct thermal treatments were performed to both clean the powder and correct possible oxygen vacancies[8]. The sample was treated a first time at 550 °C under high vacuum and a second time at 450 °C in an O2 atmosphere to obtain a fully stoichiometric TiO2.

Considering available references, the synthesized powder underwent a single thermal treatment at 500 °C under room conditions in terms of oxygen presence. It was estimated that this operation could allow a proper calcination without damaging potential (001) anatase exposed facets. Considering that the temperature was slightly below the threshold identified by Hu et al, the treatment lasted 6 hours instead of just 2[7].

Following the synthesis, an extended characterization of the obtained powder was performed. It must be noted that it is impossible to establish the exact TBOT/HF molar ratio occurring in the reference work because of the unavailability of the HF concentration[4]. Considering a 49 wt. % concentration, due to its common commercial availability, the ratio was estimated to be around 1/7. Conversely, in the synthesis proposed by the present work, given the different precursor, the ratio was calculated to be around 1/6, which is fully comparable to the reference. It must be considered that other authors proposed drastically lower Ti/HF ratios, such as 1/300, to obtain comparable percentages of exposed (001) anatase facets[5].

Following the previous introduction, XRD, Raman, and SEM were used to characterize the synthesized sample. For XRD and SEM characterization, a sample of $TiO_2$ synthesized in accordance with the reported recipe but without HF was measured as well, as an internal reference. As the annealing procedure was absent in the original synthesis recipe, thus the characterizations were conducted on both samples before and after the calcination at 500 °C.

X-ray diffraction (XRD) patterns of all samples were collected using a PANalytical X'Pert Pro diffractometer (Malvern, UK). This instrument was equipped with an X'Celerator detector and a Cu anode $CuK_\alpha$ = 1.5406 Å, operating at 40 kV and 40 mA. For the analysis, the samples were prepared using the up-loading technique.

Comparing the patterns of the two synthesized powders, it appears that no significant differences are observable, indication that the obtained $TiO_2$ is pure anatase. XRD can offer a structural indication of any potential increase in the (001) facet, by simply calculating the ratio between (004) and (101). Table 7.1 reports the calculated values for each sample, revealing that the sample which was not

synthesized with HF presents a slightly higher percentage of the (001) exposed facet. The thermal treatment appears to decrease the percentage of the (001) facet for both samples, suggesting that the instability of the (001) facet does not allow it to resist high temperatures, with a potential conversion to most stable facets, probably (101). However, it should be noted that the subsequent SEM characterization reveals a lack of flat morphology in the sample crystals.

Despite this, it appears that specific peaks show a clear trend. Setting aside the (004) peak, attention may be directed toward (200) and (211), as the former allows characteristic $CO_2$ adsorption geometry, and the latter was described as highly reactive surface[9], [10], [11]. Notably, the (200) peak changes in both intensity and shape due to the presence or the absence of HF. Table 7.1 reports their ratios with respect to the (101) peak. Due to the limited variations in peak intensity, no definitive conclusions can be drawn; therefore, further investigation is required.

Following these considerations, it appears that in the case under analysis the (001) plane of anatase cannot be confirmed as preferential exposed facet via XRD characterization.

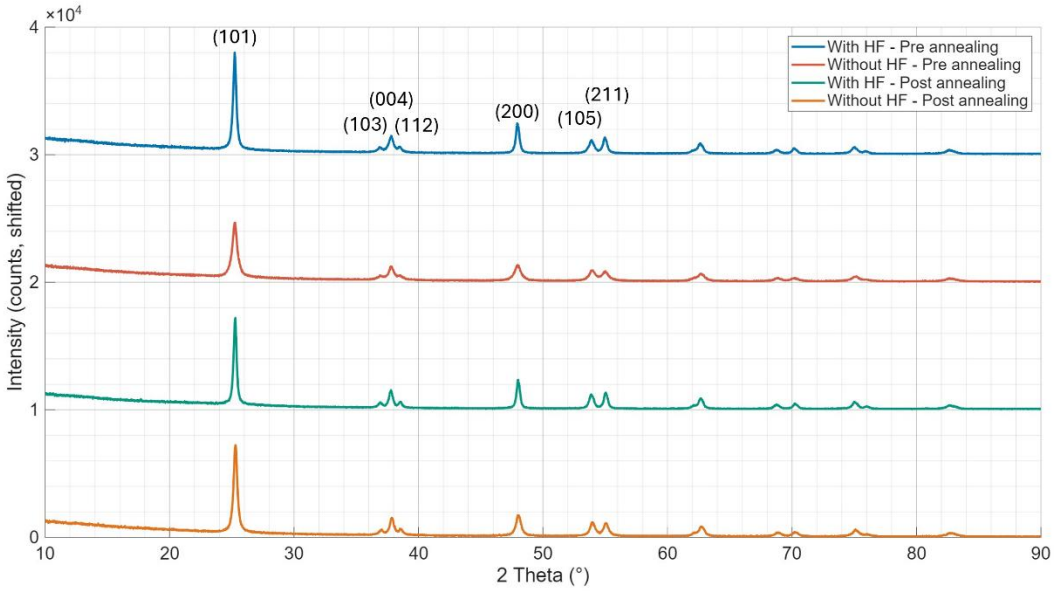



***Figure 7.1:*** *XRD patterns of anatase samples synthesized without and with hydrofluoric acid as a capping agent. Samples were measure before and after annealing to evaluate possible variations provoked by the thermal treatment. Crystal planes associated with relevant peaks are reported.*

| Sample | $I_{004}/I_{001}$ | $I_{200}/I_{101}$ | $I_{211}/I_{101}$ |
|---|---|---|---|
| With HF – Pre annealing | 20% | 29% | 16% |
| Without HF – Pre annealing | 24% | 26% | 15% |
| With HF – Post annealing | 18% | 31% | 18% |
| Without HF – Post annealing | 19% | 22% | 15% |

***Table 7.1:*** *$I_{004}/I_{001}$, $I_{200}/I_{101}$, and $I_{211}/I_{101}$ calculated from XRD patterns in Figure 7.1. Absolute values of peaks were baseline corrected.*

Second characterization of the powders was performed with Raman spectroscopy using a LabRAM HR spectrometer by Horiba equipped with He–N laser (λ=633 nm). Exposure time was set to 3 s and 1 s for the region 100-1000 $cm^{-1}$ for the samples before and after the thermal treatments. For the region 1000-3500 $cm^{-1}$, exposure time was increased to 60s and 120 s respectively to detect presence of eventual adsorbate species, probably residues from the synthesis procedure.

The spectra reported in Figure 7.2 describe the characteristic anatase profile, with four principal bands at 144, 393, 517, and 638 $cm^{-1}$[12], with another minor peak at 195 $cm^{-1}$. As expected from XRD, no other phases were detected. The ratio $A_{1g}/E_g$ was described as relevant to identify the percentage of exposed (001) facet, although the accuracy of the method remains debatable[5]. Furthermore, for a precise evaluation of the Eg peak at 144 $cm^{-1}$, signal saturation must be avoided. As clearly visible in the Figure, even with 1s of exposition time, the intensity of this peak saturated the detector.

One option could have been to use a more limited exposure time or to apply a filter; however, this could have resulted in a lower signal-to-noise ratio for other features. Moreover, it would have introduced a variability factor with respect to the previous measurement, which was not properly replicable as the sample was already calcined. Thus, a mathematical correction was preferred. For the spectrum acquired before annealing the ratio between the baseline-corrected intensities for the two $E_g$ peaks can be properly calculated ($E_{1g\text{-}144}/ E_{1g\text{-}638} = 9.53$). Since it was assumed to be almost constant, the calculated value was used as a correction coefficient to estimate the value of the $E_{1g}$ at 144 $cm^{-1}$ for the other spectrum. Following this calculation, the $A_{1g}/E_g$ ratio was calculated to be 7.7% for the sample before annealing and estimated to be 6.2% for the one after calcination. Even if there is no match with the results obtained from diffraction—a phenomenon also observed in the reference paper—it appears that the decreasing trend cause by the calcination seems to be confirmed.

Possible shifts recorded in this region of the spectrum may be assigned to both artifacts and actual variations inside the sample due to calcination. Artifacts deriving from an incomplete alignment of the laser and the detector appear to be the most probable reason, as, in any case, the shift is limited to few a $cm^{-1}$.

As clearly observable from the spectra measured in the region 1000–3500 $cm^{-1}$, the prolonged exposure times increased the overall noise in the measurement and lead to a more frequent presence of artifacts (as observed at 2650 $cm^{-1}$ for the sample post-annealing). Some features present in both spectra turned out to be shifted, except for the C–H stretching in the region 2800–3000 $cm^{-1}$, which appears to be completely absent after the thermal treatment. This clearly demonstrates how the calcination removed the organic contaminants. The origin of the shift of the other features was not investigated.

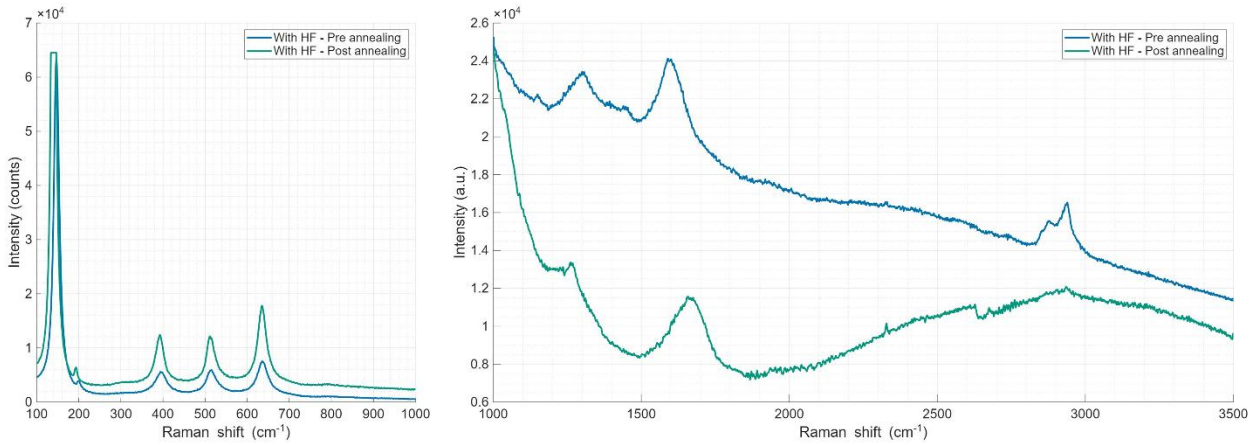



***Figure 7.2:*** *Raman spectra of the synthesized sample before and after the thermal treatment (500°C, 6 h). Exposure time was optimized according to the sample and the analysed spectral region.*

Figure 7.3 compares the SEM images of anatase samples synthesized with and without HF. Due to the small crystal dimensions, identifying the (001) facets is highly challenging, as extended flat surfaces are rarely visible. Although some sporadic areas exhibit the characteristic flat profile of this plane—consistent with the morphology reported in the reference paper—the reduced size complicates the clear identification of possible (001) anatase facets. From a catalytic perspective, smaller crystals are preferred because they maximize the exposed surface area and enhance performance. However, because of these imaging limitations, relying solely on SEM characterization may not provide a sufficiently robust assessment for these specific samples.

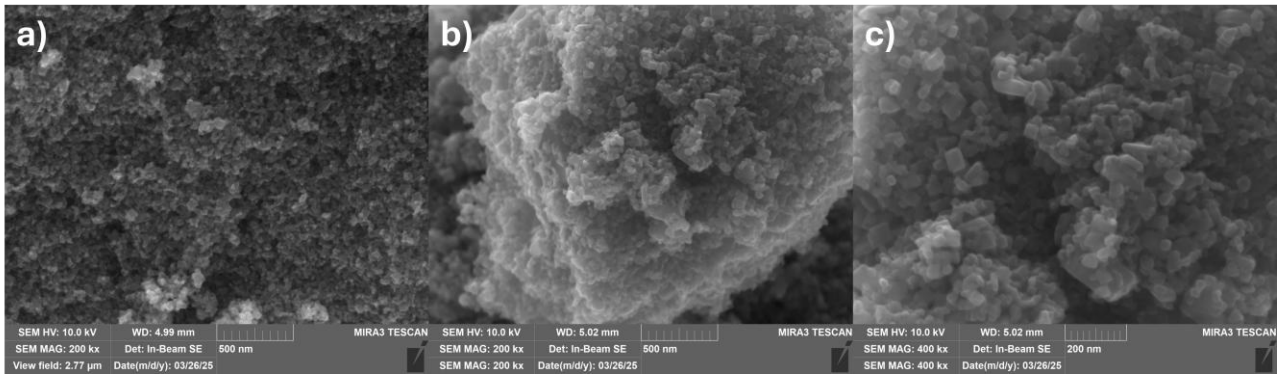



*Figure 7.3: SEM images of anatase samples synthesized (a) without and (b, c) with hydrofluoric acid as a capping agent following the recipe I. Due to the small crystal size, flat surfaces indicating the (001) anatase facets are difficult to detect. Images courtesy of Prof. Dario Zappa.*

Based on the characterization results and the subsequent analysis, the prevalence of the exposed (001) anatase facet could not be confirmed. Therefore, as previously noted, further TEM analysis will be performed.

## Synthesis II: recipe and SEM characterization

The second synthesis was adapted from the work of Yang et al (2009)[13]. The main difference with respect to the first one was the acidic conditions under which the synthesis was carried out, which could have promoted the formation of larger crystals according to many authors.

In their work, a titanium tetrafluoride (TiF4) was dissolved in an HCl at pH=2 solution to obtain a TiF4 concentration of 0.04 M. The pH was then adjusted with deionized water. The procedure required 14.5 mL of the above solution (2.76 mM), 13.38 mL of 2-propanol and 0.5 mL of hydrofluoric acid (HF, 10% w/w). The resulting mixture was transferred into a Teflon-lined stainless-steel autoclave and kept at 180 °C for at least 6 hours under hydrothermal conditions. The obtained powder was then harvested via centrifugation and washed with deionized water. It was specifically described that after an overnight drying in a vacuum, the powder was kept at 600°C for 90 minutes to eliminate fluorine from the surface.

The introduced readaptation included TTIP as a replacement for $TiF_4$ at the same concentration. Another critical variation included the absence of the subsequent dilution of the precursor solution, as it was found through experimentation that the reaction yield was almost negligible when dilution was applied. The drying was performed under room conditions, given that the subsequent calcination

was expected to eliminate contaminants. It must be noted that this procedure is intrinsically safer as it does not include pure organic solvents.

Although the powder obtained with this procedure was not deeply investigated, SEM characterization was performed to identify the presence of larger crystals. The peculiar morphology reported in Figure 7.4 describes a coherent presence of microparticles where extended flat surfaces are partially intergrown. The SEM images reported in the reference work presented a different morphology, with flat microcrystals completely separated from one another. However, the situation in Figure 7.4 is strongly correlated to what was showed in another work where a similar procedure was followed[14]. Interestingly, the formation of polycrystalline agglomerates was obtained when the Ti precursor concentration was increased, consistently with the absence of further dilution in the synthesis introduced in the present work. This reference acquires particular interest as, even though flat surfaces are clearly identifiable in their SEM images, the XRD pattern seems not to show strong (004) peak. As previously discussed, in the case of a different sample where crystals were oriented along the (001) direction, the (004) peak is predominant.

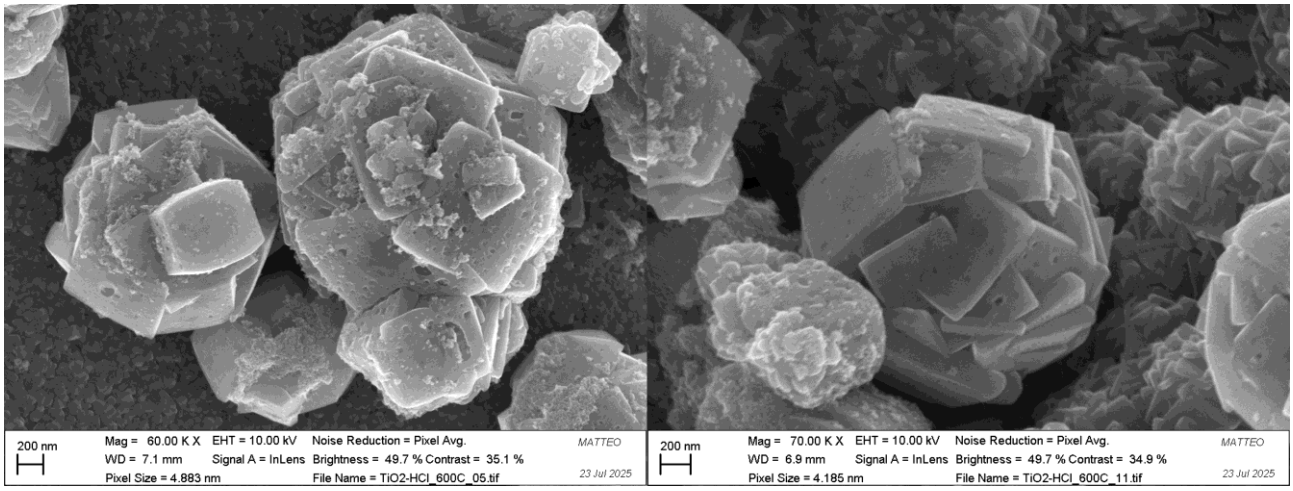



*Figure 7.4: SEM images of anatase samples synthesized according to procedure II. Microscopic size of the crystals allows the detection of extended flat surfaces comparable with (001) planes. Images courtesy of Prof. Matteo Ferroni.*

The latter synthesis procedure proposed aimed at the formation of larger crystals, whose presence was confirmed via SEM characterization. The interesting morphology obtained represents a strong basis for further investigations, although it was hypothesised that the reduced surface area may limit the efficiency of this material from a catalytic point of view.

## References


[1] ‘Chapter 7: Basics of X-ray Diffraction’, 1999, Accessed: Jun. 16, 2026. [Online]. Available: www.scintag.com

[2] C. K. Nguyen, H. G. Cha, and Y. S. Kang, ‘Axis-Oriented, Anatase TiO2 Single Crystals with Dominant {001} and {100} Facets’, *Cryst. Growth Des.*, vol. 11, no. 9, pp. 3947–3953, Sep. 2011, doi: 10.1021/CG200815T.

[3] H. G. Yang *et al.*, ‘Solvothermal Synthesis and Photoreactivity of Anatase TiO2 Nanosheets with Dominant {001} Facets’, *J. Am. Chem. Soc.*, vol. 131, no. 11, pp. 4078–4083, Mar. 2009, doi: 10.1021/JA808790P.

[4] J. Song, L. Yan, J. Duan, and C. Jing, ‘TiO2 crystal facet-dependent antimony adsorption and photocatalytic oxidation’, *J. Colloid Interface Sci.*, vol. 496, pp. 522–530, Jun. 2017, doi: 10.1016/J.JCIS.2017.02.054.

[5] F. Tian, Y. Zhang, J. Zhang, and C. Pan, ‘Raman Spectroscopy: A New Approach to Measure the Percentage of Anatase TiO2 Exposed (001) Facets’, *Journal of Physical Chemistry C*, vol. 116, no. 13, pp. 7515–7519, Apr. 2012, doi: 10.1021/JP301256H.

[6] S. Yang *et al.*, ‘Titania single crystals with a curved surface’, *Nature Communications 2014 5:1*, vol. 5, no. 1, pp. 5355-, Nov. 2014, doi: 10.1038/ncomms6355.

[7] T. Hu, P. Feng, L. Guo, H. Chu, and F. Liu, ‘Construction of Built-In Electric Field in TiO2@Ti2O3 Core-Shell Heterojunctions toward Optimized Photocatalytic Performance’, *Nanomaterials 2023, Vol. 13, Page 2125*, vol. 13, no. 14, p. 2125, Jul. 2023, doi: 10.3390/NANO13142125.

[8] L. Mino, G. Spoto, and A. M. Ferrari, ‘CO2 Capture by TiO2 Anatase Surfaces: A Combined DFT and FTIR Study’, *Journal of Physical Chemistry C*, vol. 118, no. 43, pp. 25016–25026, Oct. 2014, doi: 10.1021/JP507443K.

[9] J. Xu *et al.*, ‘Ab Initio Study of Water Adsorption and Reactivity on the (211) Surface of Anatase TiO 2’, 2016, doi: 10.1103/PhysRevApplied.5.064001.

[10] M. Lazzeri, A. Vittadini, and A. Selloni, ‘Structure and energetics of stoichiometric TiO 2 anatase surfaces’, doi: 10.1103/PhysRevB.63.155409.

[11] M. Yu, R. Li, J. Li, X. Yang, and Y. Peng, ‘Enhanced CO2 Adsorption and Conversion Induced by Surface Oxygen Vacancy on Low-Index (010) Surface of Anatase TiO2’, *ChemPhysChem*, vol. 26, no. 18, p. e202500245, Sep. 2025, doi: 10.1002/CPHC.202500245;PAGE:STRING:ARTICLE/CHAPTER.

[12] S. S. El-Deen *et al.*, ‘Anatase TiO2 nanoparticles for lithium-ion batteries’, *Ionics 2018 24:10*, vol. 24, no. 10, pp. 2925–2934, Jan. 2018, doi: 10.1007/S11581-017-2425-Y.

[13] H. Gui Yang *et al.*, ‘Solvothermal Synthesis and Photoreactivity of Anatase TiO 2 Nanosheets with Dominant {001} Facets’, doi: 10.1021/ja808790p.

[14] C. K. Nguyen, H. G. Cha, and Y. S. Kang, ‘Axis-Oriented, Anatase TiO2 Single Crystals with Dominant {001} and {100} Facets’, *Cryst. Growth Des.*, vol. 11, no. 9, pp. 3947–3953, Sep. 2011, doi: 10.1021/CG200815T.

# 8. Conclusions and future perspectives

The work presented in this thesis is characterized by a hybrid computational and experimental approach, which enabled an in-depth investigation into many of the phenomena studied. Density Functional Theory (DFT) served as a fundamental methodology for performing reliable simulations of material behaviour, providing the necessary framework to predict the outcomes of subsequent experimental characterization.

In the first section, the primary focus is on titanium dioxide ($TiO_2$) and its role as a carbon dioxide adsorbent to promote photocatalytic applications. As extensively documented in the literature, the capacity of a material to interact with molecules is strongly influenced by its exposed crystal plane. This correlation is particularly relevant for $TiO_2$; indeed, beyond the general dependence on the crystalline phase, the ability to adsorb molecules, carbon dioxide in this case study, is strictly dictated by the geometry of the exposed surface atoms. In the case of anatase, the (101) surface exhibits poor $CO_2$ adsorption properties, whereas other planes, including the (001) facet extensively investigated in this work, provide significantly more stable adsorption geometries.

Before proceeding with the simulations, however, it is essential to conduct robust convergence tests to establish a reliable working framework. Stringent simulation parameters may drastically increase the required computational effort; thus, a trade-off between accuracy and complexity must be evaluated. The impact of several parameters is relatively marginal, thereby eliminating the need for their exhaustive optimization, although focusing solely on the few parameters typically evaluated may not be enough to provide predictive results.

The core parameters requiring proper convergence tests are the cut-off energy and the number of k-points, as they drastically affect both simulation accuracy and computational time. Generally, it is impossible to define a universally safe framework without considering other computational settings, most notably the exchange-correlation functionals employed. Consequently, each specific case study must include its own dedicated convergence tests.

Another computational parameter found to significantly impact simulation outcomes is the supercell size used to model a surface. Indeed, certain behaviours observed for the (001) anatase facet vary depending on the lateral dimensions of the supercell. This variation can affect adsorption kinetics and geometries, potentially leading to an incorrect evaluation of the stability of certain configurations.

As previously noted, a material's reactivity highly depends on its exposed crystal plane. Consequently, calculating the surface energy, also referred to as formation energy, associated with each crystal facet becomes crucial. This approach not only provides a general indication of material reactivity, which remains inherently dependent on the specific molecules involved in the reaction or adsorption, but also allows for an estimation of the stability of a real sample with preferentially exposed planes. Indeed, a highly reactive facet may be unstable and undergo reconstruction into a more stable configuration. In this regard, key computational challenges were identified, once again linked to the supercell size and the appropriate number of k-points required to sample the first Brillouin zone. Furthermore, it was demonstrated that slab thickness can also influence the calculated surface energy, though this effect is strictly dependent on the specific exposed facet.

Once the computational parameters for accurate simulations were defined, the adsorption geometries of $CO_2$ on the anatase (101) and (001) surfaces were identified, confirming literature data regarding the ability of the latter to form carbonate and bicarbonate species. As valuable additional insight, the role of water in promoting $CO_2$ adsorption was hypothesized. For each adsorption configuration, vibrational frequencies were calculated, correcting the harmonic approximation through the evaluation of the anharmonic component.

Following the completion of the computational section regarding $TiO_2$, experimental validation was pursued. A titania sample with preferentially exposed anatase (001) facets was synthesized according to procedures described in the literature. A detailed analysis of the synthesis and characterization of this $TiO_2$ sample is provided in a separate section. This detailed examination was deemed necessary because the synthetic procedure lacks scalability and presents significant safety concerns, given the use of hydrofluoric acid and organic solvents under hydrothermal conditions. Furthermore, an additional challenge lies in accurately identifying the preferentially exposed crystal planes.

The synthesized powder was characterized using Infrared, Raman, and X-Ray Photoelectron Spectroscopy (XPS) to identify the presence of adsorbates. FTIR analysis revealed a clear contribution from linearly adsorbed $CO_2$ and structural water within the sample, whereas no carbonate or bicarbonate species were detected. A subsequent experiment was conducted by adding a small amount of water to the powder, followed by drying under ambient conditions. This procedure led to the emergence of numerous previously absent spectral features, in addition to those clearly associated with water modes. Intriguingly, these new peaks were located at positions comparable to those computed for the stable geometries resulting from $CO_2$ adsorption. This not only confirms the

accuracy of the simulations but also provides experimental validation for the crucial role of water in promoting $CO_2$ adsorption. Finally, C-H stretching bands were clearly detected in the spectra after the hydration-dehydration treatment, although their origin remains unidentified.

The computational model adopted in this work enabled an unambiguous identification of the specific $CO_2$ adsorption geometries on the (001) anatase surface. This achievement represents a significant advancement over existing literature, where establishing a direct correlation between theoretical configurations and spectroscopic evidence is generally far less straightforward, often leaving room for ambiguity.

Raman and XPS characterizations yielded similar conclusions; however, inherent limitations in the computational method for vibrational frequencies resulted in lower predictability for Raman-active modes. Concurrently, the interpretation of the XPS data demonstrated that the carbonate species adsorbed following water addition interest the outermost surface layers of the sample.

Despite the promising results achieved for $CO_2$ adsorption on the (001) anatase facet, the challenges surrounding its synthesis and characterization remain highly significant, severely limiting its industrial scalability. To address this issue, an alternative strategy was explored, involving the use of commercial anatase samples enriched with metal ions. This approach successfully bypasses the drawbacks associated with hydrothermal synthesis and the handling of hazardous reagents.

In this case as well, the initial approach was computational, examining the adsorption of species containing $Ca^{2+}$ and $Mg^{2+}$ ions onto (101) anatase surfaces. After confirming the stability of these systems, $CO_2$ adsorption was simulated, demonstrating that it is possible to achieve significantly more stable configurations compared to those obtained on stoichiometric (101) anatase. Subsequently, Raman characterization of a powder synthesised accordingly to the simulations was performed, aiming to the identification of potential adsorbates. As observed for stoichiometric (001) anatase, spectral features attributable to adsorbed carbonates or bicarbonates were identified. However, limitations in the computational method used for vibrational frequencies still restricted a direct assignment to the theorized adsorption geometries. In this instance too, the presence of organic species was clearly identifiable.

Regarding the $TiO_2$ section, two fundamental questions remain open. The first concerns the identification of the preferentially exposed crystal plane, a challenge that can be effectively addressed through Transmission Electron Microscopy (TEM) characterization. This technique, not only for titania

but also for other systems, could offer clear and unequivocal information regarding the exposed facet. The second involves extending the studies on the metal-atom enrichment of commercial TiO2 samples. Given the striking similarities with the observations from the stoichiometric (001) anatase study, this could prove to be an excellent pathway toward developing samples capable of adsorbing $CO_2$ without the constraints of operational safety and industrial scalability.

The second section of this thesis covers alternative projects conducted during the PhD program that are unrelated to $CO_2$ adsorption on $TiO_2$. Nonetheless, several of these studies retained the hybrid computational-experimental approach, enabling an in-depth investigation of the investigated phenomena.

One case study addresses the potential reaction between two refrigerant gases, hypothesized following thermodynamic testing that revealed the formation of a liquid phase and solid particles. DFT calculations enabled the identification of potential reaction products, one of which demonstrated high stability and is likely representative of the molecules experimentally obtained. Vibrational spectroscopy further confirmed that this product possessed a structure matching the computational estimates. It should be noted that this study is currently undergoing peer-review, and the interpretation of the results may be subject to minor refinements.

Additionally, DFT proved highly valuable in examining the interaction between polydopamine and histamine, providing a robust rationale for phenomena observed via Raman spectroscopy within the framework of low-concentration pollutant sensing.

Studies strictly focused on spectroscopy involved estimating the degree of deacetylation (DDA) of chitosan via FTIR and investigating microplastics using Raman spectroscopy. In both cases, a primary challenge clearly emerged from the presence of baselines within the measured spectra. Consequently, identifying an effective algorithm capable of removing these baselines while preserving the spectral features of interest became a central objective.

In conclusion, the findings of this thesis offer valuable insights for broad applications and establish a solid foundation for future research. The hybrid approach demonstrated throughout this work has proven highly effective in detecting carbonate and bicarbonate species originating from CO2 adsorption on surfaces exposing the (001) crystal facet. Furthermore, the role of co-adsorbed species can significantly influence overall adsorption properties—as demonstrated herein for water—highlighting that their presence should always be carefully considered. Within this context, the

computational framework is crucial for achieving robust simulations, while experimental characterization remains fundamental to validate these computational models. As demonstrated in the second main section of this thesis, this integrated approach is versatile and applicable to numerous case studies beyond those investigated here.

The methodologies and results highlighted in this work could find applications in several high-impact scientific fields, such as catalysis and pollutant storage, where adsorption and surface properties represent key operational factors. In particular, the development of next-generation TiO2-based catalysts could represent a turning point for the ongoing energy transition, highlighting the contemporary relevance of this study. Furthermore, the outcomes of the other case studies could significantly benefit analytical chemistry, as the supporting methodologies were comprehensively evaluated, and their strengths and criticalities thoroughly discussed. Consequently, integrating these results and methodologies into future studies will undoubtedly enhance the scope and impact of research across multiple disciplines.